NOTE TO USERS

Page(s) not included in the original manuscript and are unavailable from the author or university. The manuscript was scanned as received.

vi-xvi

This reproduction is the best copy available.

UMI®

Université d'Ottawa • University of Ottawa

Université d'Ottawa · University of Ottawa

FACULTÉ DES ÉTUDES SUPÉRIEURES ET POSTDOCTORALES

FACULTY OF GRADUATE AND POSTDOCTORAL STUDIES

Yansong CUI

AUTEUR DE LA THÈSE - AUTHOR OF THESIS

M. A. Sc. (Electrical Engineering)

GRADE - DEGREE

School of Information Technology and Engineering

FACULTÉ, ÉCOLE, DÉPARTEMENT - FACULTY, SCHOOL, DEPARTMENT

TITRE DE LA THÈSE - TITLE OF THE THESIS

GaAs-based Travelling Wave Electro-optic Modulators

P. Berini

DIRECTEUR DE LA THÈSE - THESIS SUPERVISOR

CO-DIRECTEUR DE LA THÈSE - THESIS CO-SUPERVISOR

EXAMINATEURS DE LA THÈSE - THESIS EXAMINERS

L. Roy

J. Yao

J.-M. De Koninck, Ph.D.

LE DOYEN DE LA FACULTÉ DES ÉTUDES SUPÉRIEURES ET POSTDOCTORALES

SIGNATURE

DEAN OF THE FACULTY OF GRADUATE AND POSTDOCTORAL STUDIES

GaAs-based Traveling Wave Electro-optic Modulators

By

Yansong Cui

A thesis submitted to the
Faculty of Graduate and Postdoctoral Studies
in partial fulfillment of the requirements for the degree of

Master of Applied Science

in Electrical Engineering

Ottawa-Carleton Institute of Electrical and Computer Engineering
School of Information Technology and Engineering
University of Ottawa
Ottawa, Ontario, Canada

Your file Votre référence
ISBN: 0-494-01454-7
Our file Notre référence
ISBN: 0-494-01454-7

Abstract

This thesis addresses research on the design and modeling of GaAs traveling wave electro-optic modulators with a highly doped layer. These modulators are in the form of a waveguide integrated with Planar Microstrip electrodes (PMS), and of a Mach-Zehnder interferometer integrated with capacitively loaded Coplanar Strips (CPS) electrodes. In both, the use of a thin highly doped layer ensures a good overlap between the applied electric field and optical mode. The design space of both PMS and loaded CPS electrodes are fully characterized. Waveguides of low propagation loss are designed. Wide bandwidth traveling wave modulators require low optical and microwave insertion loss, impedance matching, velocity matching and low half wave voltage. The simulation results predict that modulators with PMS electrodes have a limited frequency response while the modulators with CPS loaded electrodes have an electrical 3 dB bandwidth up to 70 GHz for 1cm device and $V\pi$ of 9.4 V·cm.

Acknowledgement

Special thanks go to my supervisor, Dr. Pierre Berini, whom I can always count for valuable suggestions and clear guidance. Without his support I may never have completed this thesis.

I thank evaluation committee, Chengkun Chen and Luan Nugyen for their valuable input.

Sincere thanks will be given to University of Ottawa and National Capital Institute of Telecommunications for the financial support during my thesis work.

Finally, I would like to thank you, my husband, Xinan Zhou, for supporting me through the difficulties and sharing the same dream with me.

Table of Contents

CHAPTER 3

CHAPTER 4

CHAPTER 5

CHAPTER 6

List of Figures

List of Tables

List of Acronyms

CPS	Coplanar strip
CPW	Coplanar waveguide
EA	Electroabsorption
MIS	Metal-insulator-semiconductor
MMI	Multimode interferometer
MQW	Multiple quantum well
MZI	Mach-Zehnder interferometer
PMS	Planar microstrip
QCSE	Quantum-confined stark effect
SI-GaAs	Semi-insulating gallium arsenide
TW	Traveling wave
WDM	Wavelength-division multiplexing

CHAPTER 1

Introduction

The next generation of optical networks operating at and above 40 Gbits/s stimulates the development of a range of high-speed electronic and opto-electronic components. Very wide bandwidth external optical modulators are one of these key components. Their importance comes from the requirements for extremely high coherence and stability of laser sources – qualities which are compromised by high-speed direct modulation of the drive current in the case of semiconductor lasers. This research focuses on the development of high speed Gallium Arsenide (GaAs) traveling wave electro-optic external modulators using doped epitaxial layers. The bandwidth of these modulators can extend to 40 GHz and above.

In this chapter, the history and current state of optical communication are briefly reviewed, followed by an introduction to integrated devices and to electro-optic modulators. Thesis objectives and outlines are also presented.

1.1 Optical Communications

Great effort has been made to increase the capacity of communication systems in the late part of the twentieth century. It was not until the 1950s that people realized that the transmission of a large amount of information over long distances would be possible if

optical waves were used as the carrier. However, neither a coherent optical source nor a suitable transmission medium was available at that time. The invention of the laser [1] in 1960 solved the first problem, which provides an appropriate coherent light source for optical communication. Later on, semiconductor lasers were proven to be a good choice for this purpose due to their compactness, reliability and potential for monolithic integration with other optical and electronic devices. On the other hand, it was suggested in 1966 that optical fiber might be the best transmission medium, however its loss was in excess of 1000dB/km. The reduction of optic fiber loss to 20 dB/km in 1970 made it a preferred medium for optical communications [2]. At present, the optical fiber loss has been drastically reduced to 0.2 dB/km.

There have been five generations of fiber optic communication systems. The first generation, operating near 0.85 μm and using multimode fiber, was commercially available in 1970 [3]. The second generation of fiber optic communication systems appeared in the early 1980s. Though it still used multimode fiber, it operated in the wavelength region near 1.3 μm where dispersion is minimal. The third generation is characterized by minimum fiber loss and minimum dispersion for it uses single mode, dispersion-shifted fiber at the wavelength of 1.55 μm.

The fourth generation system is revolutionary in the development of optical communication systems. It makes use of optical amplification to increase the repeater spacing and of wavelength-division multiplexing (WDM) to increase the bit rate. The advent of erbium-doped fiber amplifiers makes long haul optical communications cost

effective. Currently, the fourth generation systems focus on the increase of system capacity by transmitting multiple channels through the WDM technique. Some researchers have demonstrated that the capacity of single channel could extend up to 40 Gb/s and a 160 Gb/s WDM transmission was realized by using a four-channel wide spaced multiplexed signal [4]. Furthermore, dense wavelength -division multiplexing is deployed to meet the ever-growing bandwidth demand. At present, WDM systems with channel capacity of 10 Gb/s are commercially available.

The fifth generation system is optical solitons, optical pulses that preserve their shape during propagation in a low loss fiber by counteracting the effect of dispersion through the fiber nonlinearity. Optical solitons provide a solution to the fiber -dispersion problem that the former four generations of systems failed to solve. Soliton-based optical communications are under the development [5]. WDM may not be the only way to increase the capacity of fiber, since a higher number of wavelengths will crease undesirable effects. Optical solitons using TDM may provide an alternative solution for very long high bit rate links.

1.2 Electro-Optic Modulators

Modulation of the optical signal in optical communications can be divided into direct modulation and external modulation. The schematic diagram of a typical optical fiber communication system is depicted in Figure 1.1.

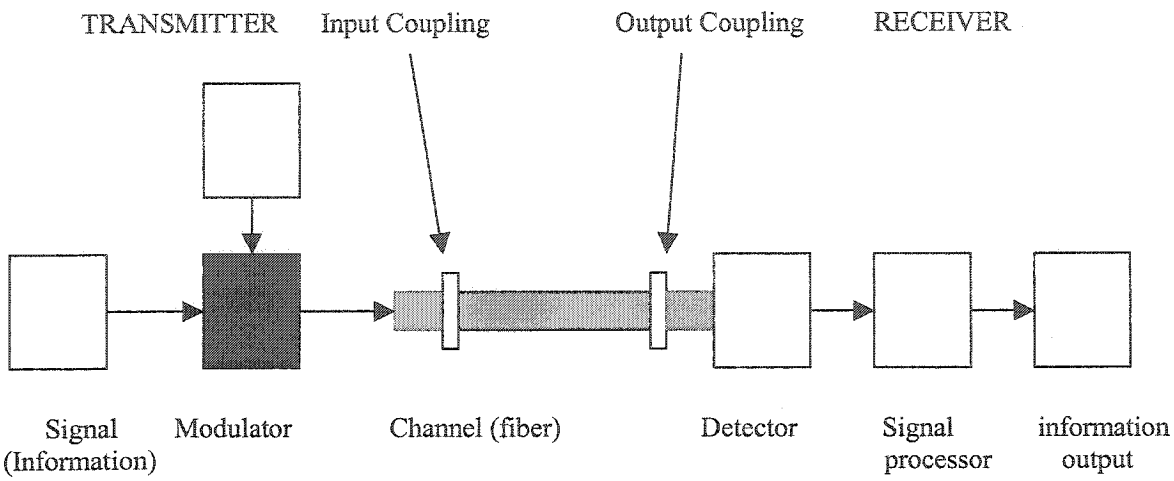

Figure 1.1 Schematic of a typical optical fiber communication system.

Semiconductor lasers are frequently used under direct modulation. Although direct modulation of semiconductor lasers offers simplicity and large amplitude modulation, it has some disadvantages, such as frequency chirp and modulation bandwidth limitation. The frequency chirp refers to the time-dependent frequency shift. The frequency chirp often limits transmission quality because of the dispersion in optical fibers [6]. The frequency bandwidth of semiconductor lasers is inherently limited. The present frequency limit for direct laser modulation exceeds 40 GHz and these devices have been used for large-signal digital modulation at 20 Gb/s [7]. Direct modulation of semiconductor lasers is currently being employed for optical communication systems operating at 2.5 Gb/s (OC48) or less.

The limitations of directly modulated lasers in optical communications stimulate the development of high-speed external modulators. An external optical modulator can

modulate the light output power from lasers with no frequency chirp or a small negative chirp while providing a larger modulation bandwidth [8]. Usually, a small negative chirp will provide some pulse compression that can balance out the pulse broadening in the fiber. All OC 192 (10 Gb/s) optical communication systems are using external modulators to modulate the optical signals. External modulators are essential components for the next generation of optical network operating at 40 Gb/s and higher.

The basic qualities required of any wide band modulator are large bandwidth with a flat frequency response and linear phase response over the required band, low drive power from a standard 50 Ω generator, high return loss over the band, and low optical insertion loss. The main figure of merit of an optical modulator can be given by the modulation bandwidth divided by the drive voltage (GHz/V). Naturally, one should increase the bandwidth while keeping drive voltage as low as possible.

According to the physical phenomena utilized, external modulators can be divided into two distinct kinds: electroabsorption (EA) modulators [9] and electro-optic modulators [10]. The EA type of modulators modulates light by changing the optical absorption coefficient of a semiconductor medium under the application of an electric field. EA modulators operate on a quantum tunneling principle, termed the Franz-Keldysh effect in bulk materials and the quantum-confined stark effect (QCSE) in quantum well.

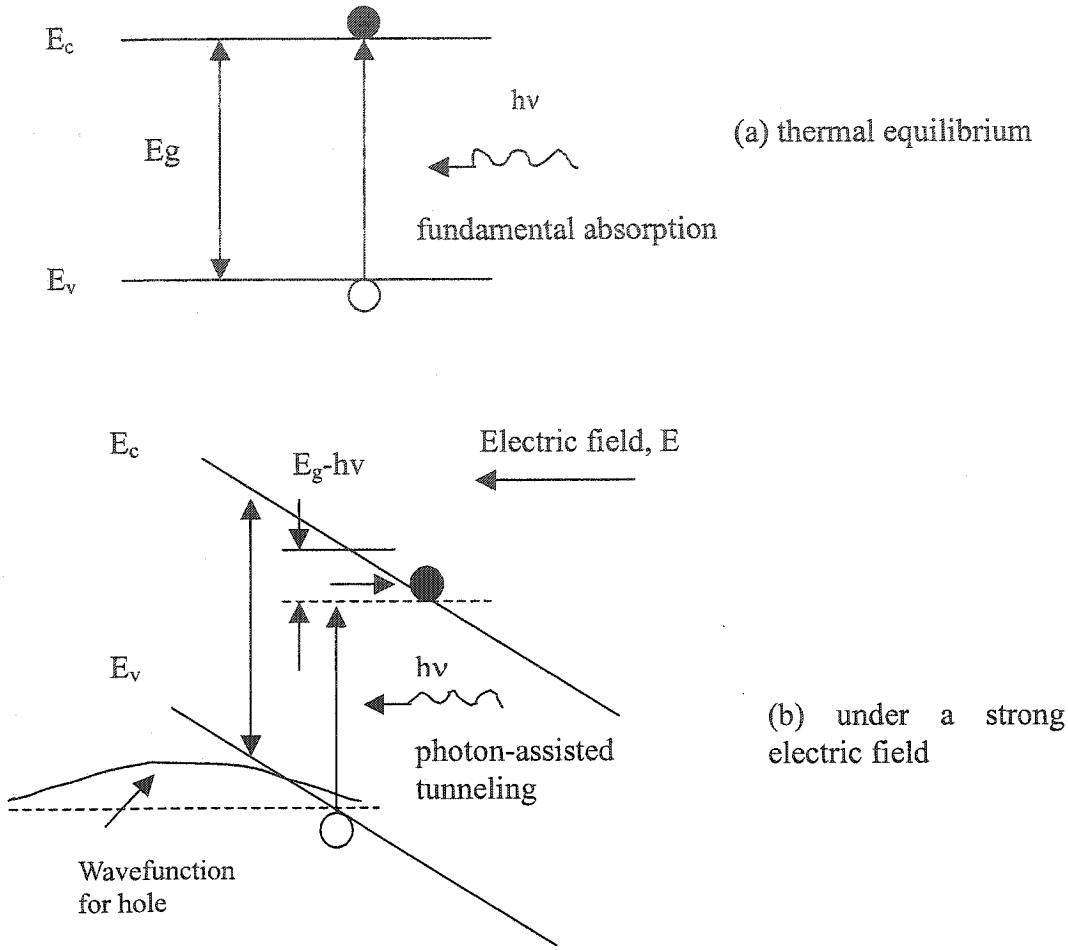

Figure 1.2 Schematic diagram of the tilting of energy bands under a strong electric field and of the Franz-Keldsh effect.

A strong electric field applied to a semiconductor tilts the band edges, valence band maximum, and conduction band minimum, and the wavefunctions for electrons and holes penetrate into the band-gap as shown in Figure 1.2. The photo-assisted tunneling therefore occurs at a wavelength longer than the wavelength corresponding to the band-gap energy. Consequently, the fundamental absorption edge shifts to a longer wavelength. This phenomenon is called the Franz-Keldysh effect and it is large when the field strength is more than 10^4 V/cm.

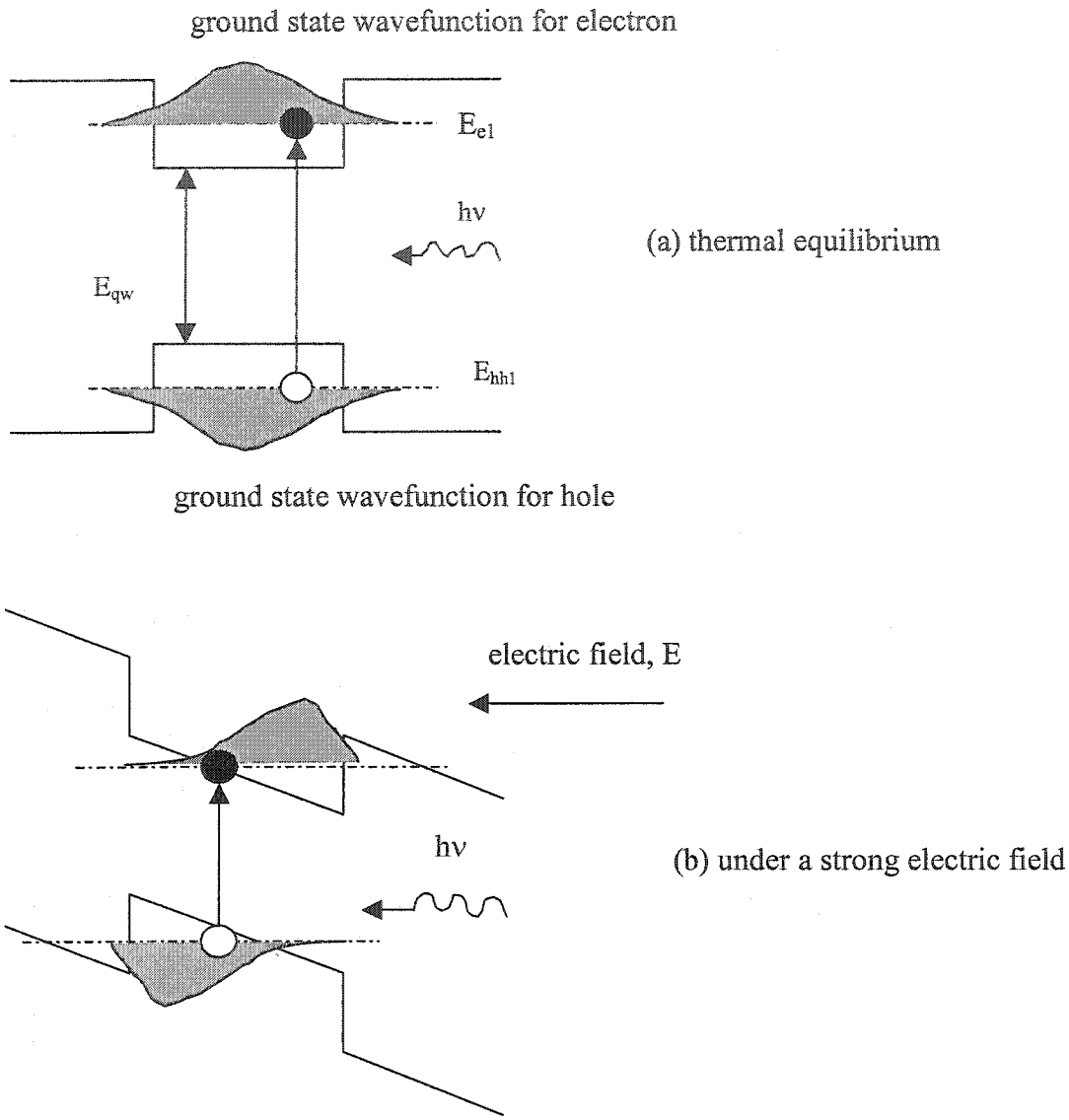

Figure 1.3 Schematic diagram of the tilting of energy bands under a strong electric field and of the quantum-confined stark effect. E_{e1}, E_{hh1} designate energy levels for electrons and heavy holes, respectively.

Concerning QCSE, electrons and holes are confined in the same physical quantum well (QW) so that they strongly interact and overlap to form a bond. This is called an exciton and has a strong absorption. Under the applied electric field, electron and hole are forced to opposed ends of QW and are physically separated as shown in Figure 1.3, and simultaneously the binding energy of the exciton decreases. Consequently, the effective

band-gap energy decreases with increasing electric field strength, and the refractive index also changes. This phenomenon is called QCSE. QCSE is most pronounced for photon energies near the bandgap of the material and shows strong wavelength dependence. The shift of the absorption edge is larger for the QCSE than it is for the Franz-Keldysh effect. In short, QCSE offers large changes in the real part and imaginary parts of the refractive index in the wavelength range near band gap region. Thus multiple-quantum well (MQW) EA modulators offer low modulation voltage, though they suffer from frequency chirp and high insertion loss.

At the wavelength of 1.55 μm, the desired wavelength for fiber-optic communications, EA modulators require alloys of InP and GaAs as active material grown on InP. A InGaAlAs/InAlAs MQW EA modulator at 1.55 μm has been reported with low drive voltage about 1V for 10-dB on/off ratio [11]. At 1.3 μm, EA modulators have been realized both on InP and GaAs substrates. EA modulators operating at 1.3 μm have also demonstrated low modulation voltage [12]. EA modulators also show high-speed operation. The electrical 3 dB bandwidth approaching 60 GHz has been reported for lumped devices [13]-[14]. Due to low drive voltage, high speed and compact size, EA modulators are frequently integrated monolithically with lasers [15].

Recent research on EA modulators focuses on reducing the drive voltage, and increasing the on/off ratio and the bandwidth. For the lumped device, this presents a conflict, a wide bandwidth requires a short device while high on/off ratio and low drive voltages require a long device. In one approach, a double-pass modulator has demonstrated the drive voltage

reduction of 60% [16]. The limitations of lumped device performance stimulate researchers to design the device as a traveling wave (TW) modulator. A 200-μm-long TW-EA modulator with a bandwidth of 54 GHz and a drive voltage of 3 V for 20-dB on/off ratio [17], and a 450-μm-long device with a bandwidth of 43 GHz and a drive voltage of 1.3V were reported respectively [18].

When an electric field is applied to some semiconductors or some dielectric materials, their refractive index change. This phenomenon is known as the electro-optic effect. If the change in refractive index is linearly proportional to the applied electric field, this effect is called the linear electro-optic effect (Pockels effect). Currently, electro-optic modulators are based on the linear electro-optic effect. The linear electro-optic effect is present in many materials, such as III-V compound semiconductors, lithium niobate ($LiNbO_3$), lithium tantalite (LiTaO3), ADP (NH4H2PO4), KDP (KH2PO4) and others. Among them, $LiNbO_3$ and GaAs are the most popular materials for electro-optic modulators due to the strength of the linear electro-optic effect in these materials and reasonable dielectric constants for the easy realization of velocity matching. $LiNbO_3$ is a ferroelectric crystal that is commonly used in other types of commercial products, most notably, in surface acoustic-wave filters for mobile communication receivers. Thanks to the mature technology, many excellent $LiNbO_3$ traveling wave modulators have been demonstrated and are commercially available. $LiNbO_3$ is well suited for this kind of usage owing to the large mode size of the titanium indiffused waveguides that can provide very low fiber-to-waveguide coupling loss. In the meantime, with the development in III-V epitaxial technologies, III-V semiconductors once again excite the interest for research and

development of high-speed optical components due to their versatility, potential for opto-electronic integration, and freedom from the dc charging and optical damage effects observed with $LiNbO_3$.

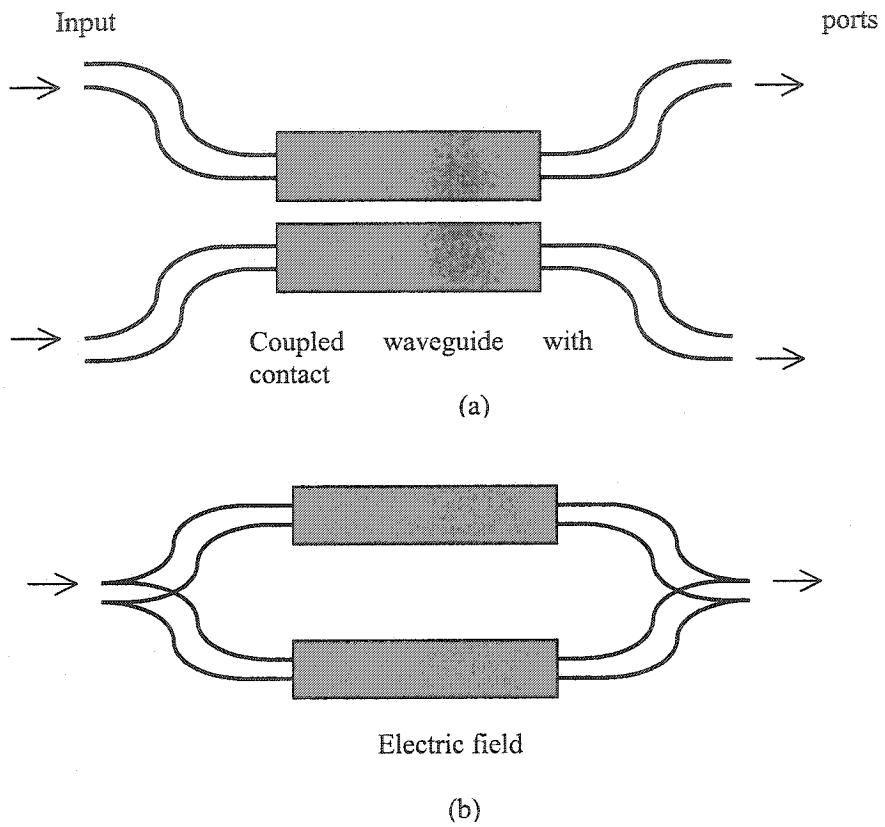

Figure 1.4 Schematic layout of a) a directional coupler electro-optic switch, b) an electro-optic Mach-Zehnder modulator.

The most common structures for external modulators and switches are directional coupler type and Mach-Zehnder interferometer (MZI) type, as shown in Figure 1.4. Though switches have additional capability of routing the signal, the basic operating principles of optical modulators and switches are similar. In the directional coupler approach, light is injected into two modes of a waveguide structure. The applied electric field modifies the relative velocities of the two modes as well as the coupling between the two modes

[19]-[20]. The directional coupler type switches are typically used for lower speed switching applications where small size and polarization diversity may be required. MZI modulator consists of two Y-branches and two phase modulation arms. The input light is divided into two paths by the Y-branch, at which the light is bisected. The light is guided to the two arms and the phase of the light in each arm is modulated by applying an electric field, so each arm works as a phase modulator. At the output Y-branch, the phase modulation is converted into intensity modulation. When the phase of the light from one arm is the same as that of the light from the other arm, the light is added constructively and propagates along the waveguide toward the output port. If the phase difference between the light propagating each arm is π, they cancel each other and no optical power is emitted from the output port. The MZI works well with high-bandwidth electrode structures requiring tens of micrometers of spacing between waveguides, and long electrodes are needed to reduce voltages. MZI modulators are the subject of this thesis and will be discussed in the next chapter.

In addition, there are other type structures for external modulators. If Multimode interferometers (MMI) are used at the input and output of the MZI modulator instead of Y-branches, the device can operate as a 2*2 switch [21]-[22]. A total internal reflection (TIR) switch has also been reported [23].

One of the key factors limiting the bandwidth of electro-optic modulators is the electrode type. Electrode types are usually divided into two types: lumped and traveling wave. For a lumped modulator, the modulation bandwidth is determined by the RC time constant of the

equivalent circuit or transit time (defined in chapter 3). However, in the case of a traveling wave modulator, the electrode is designed as a transmission line so that electrode capacitance is distributed and does not limit the modulator speed due to RC time constant limitations. Consequently, the traveling wave approach to modulator design can lead to wide bandwidth, and possibly represents the ultimate in broadband modulators. The bandwidth of traveling wave electro-optic modulators is limited by the velocity-mismatch between the modulating microwave signal and the modulated optical signal, and by microwave losses (dielectric and electrode). The velocity match condition is crucial to wide bandwidth, low modulation power and high modulation depth [24]. Velocity mismatch is caused by the leading or lagging of the microwave signal with respect to the optical signal. In the case of a $LiNbO_3$ modulator with coplanar electrodes, the optical signal travels faster than the microwave signal; therefore, to match the velocity of optical and microwave signals, the speed of propagation of the microwave signal must be increased. Electrodes that achieve this are called fast wave electrodes. In contrast, in III-V compound semiconductors, the microwave signal travels faster than the optical signal, so the microwave signal must be slowed down to achieve velocity matching. These electrodes are called slow wave electrodes.

The most commonly used electrode for $LiNbO_3$ is the coplanar waveguide, and the most common way of increasing the velocity of the microwave signal for this case is to use a SiO_2 buffer layer under the electrode and to increase the thickness of the conductors. With the advent of velocity matching techniques in $LiNbO_3$ traveling wave modulators [25], researchers target low drive voltage devices with simultaneous velocity and impedance

matching, low electrode losses, long interaction lengths, and large electro-optic overlap integrals. Approaches to achieve some of these conditions have included etched ridge devices [26]-[27], long interaction lengths [28]-[29] and reflection devices [29]. Etched ridge structures are capable of achieving near simultaneous velocity and impedance matching in LiNbO3, and have demonstrated an electrical 3 dB bandwidth of 70 GHz with $V\pi$ of 5.1 V in probe contact Z-cut LiNbO3 devices [26]. In the reflection devices, the $V\pi$ was demonstrated as low as 0.89 V at 1.3μm for an electrode and interaction length of 5.3 cm and 10.6 cm, respectively [29]. A $LiNbO_3$ Mach-Zehnder Modulator based on a cascaded Bragg grating has also been proposed with an optical 3-dB bandwidth over 100 GHz and 1 V half- wave voltage [30].

III-V compound semiconductors such as GaAs, InP, and their alloys have excellent optical properties due to their direct and tunable bandgap and are preferred materials in many optoelectronic components such as lasers and detectors. Furthermore, they are often used in modulator applications due to their possession of an electro-optic effect. GaAs, with the bandgap energy 1.42 eV, is one of the most commonly used materials for modulators. As mentioned above, for GaAs traveling wave modulators, the electrodes are slow wave electrodes, since the velocity of the microwave signal must be slowed down to match that of the optical signal. Two conventional electrode configurations for GaAs electro-optic traveling wave modulators are well known [31]. These are the microstrip configurations using p-i-n structures [32] and the coplanar strip configurations using undoped epitaxial layers grown on a semi-insulating substrate [33]. Velocity mismatch exists in both of these structures. Though p-i-n modulators have the advantage of perfect overlap close to

100%, the n+ GaAs substrates used in this case causes high microwave losses and microwave dispersion and thus limits bandwidth. A revised microstrip structure, so-called planar microstrip structure, was proposed [34]. As shown in Figure 1.5, this structure has the ground plane on top of the n+ layer with semi-insulating GaAs as the substrate,

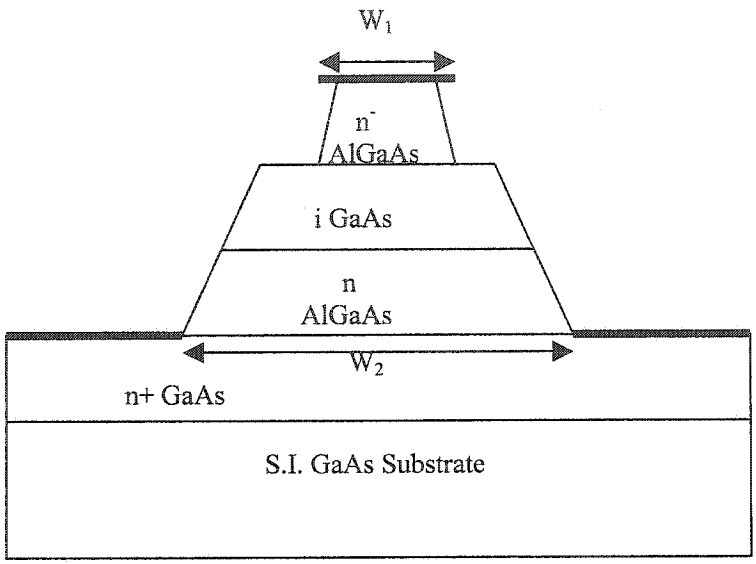

Figure 1.5 The cross section view of a new planar microstrip configuration modulator on a semi-insulating (100) GaAs substrate with double heterostrucutre cladding layers of n^- and n. A single optical mode is guided in the i-layer. The top n^- epitaxial layer and undoped i layer are easily depleted by Schottky contact. The bottom electrode of the conventional p-i-n structure is placed on the top of n^+ epitaxial layer.

and the doped n+ epitaxial layer contributes to velocity-matching and lower microwave loss, and improves the overlap integral. An optical 3 dB bandwidth >40 GHz and a half wave voltage V_π <6 V were predicted [34]. Several other slow-wave electrode structures have also been reported, such as the metal-insulator-semiconductor (MIS) structures [35], the Schottky contact structures [36], and the coplanar waveguide structures using periodically doped semiconductor substrates [37]. The inherently lossy nature of the doped semiconductor makes these slow-wave electrode structures inappropriate for use in wide

bandwidth electro-optic modulators. Nees et al also reported a velocity matching structure using a GaAs superstrate deposited directly on top of the coplanar strip electrodes; though the bandwidth reaches 100 GHz, the half wave voltage is too high, 288 V for a 5-mm modulator length [38].

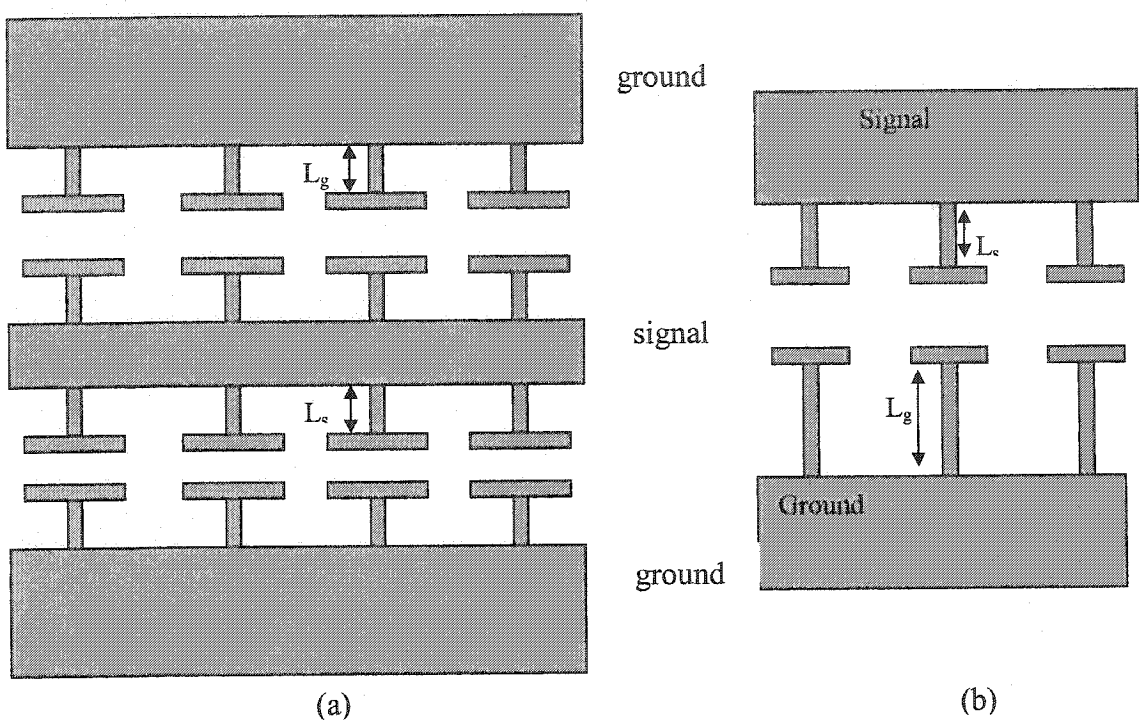

Figure 1.6 Top view of schematic of a GaAs/AlGaAs modulator Electrode (a) CPW loaded line (b) CPS loaded line.

More recently, the most common slow wave structures to be used are obtained by periodically loading a uniform transmission line. The loading element is typically capacitive. This can be achieved using either doped or undoped epitaxial layers. Spickermann et al has proposed three conductor coplanar waveguide (CPW) slow wave structures on GaAs using undoped epitaxial layers [39]. The device electrode is a modified coplanar line, in which T-rails stem from either side of the center conductor and from the

inner side of the both ground planes, as shown in Figure 1.6 (a). These T-rails form tiny capacitors, which periodically load the line, increase its capacitance per unit length, and thus slow the microwave signal propagating on the electrode. Microwave losses are mainly determined by the uniform transmission line, for the T-rails do not carry the axial transmission line current. As a result, the microwave losses can be kept low. The measured small signal electrical bandwidth of the device at 1.55 μm is in excess of 40 GHz and the measured V_π is about 16.8 V. Khazaei's thesis work is also based on both coplanar waveguide (CPW) and coplanar strip (CPS) slow wave structures on GaAs using undoped epitaxial layers as shown in Figure 1.6. In his study, the device, in which L_s no longer equals L_g,, is modified on the basis of Spickermann's device for the CPW case. The measured electrical 3 dB bandwidth exceeds 40 GHz with Vπ of 8.5 V for CPW while the bandwidth also extends over 40 GHz with V_π of 9 V for CPS [40]. The microwave losses of these structures are still very low at 40 GHz. The parallel push pull modulation reduces the half voltage by a factor of 2. However, The values for Vπ are still high for a high-speed modulator. The source of this difficulty is the poor overlap of the vertical component of the applied electric field with the optical mode. As the electrode gap gets smaller, applied field intensity increases. However, field lines start to become more tangential to the surface and the increase in its vertical component is not as much.

One way to improve the overlap is to use a doped layer [41]. Walker reported a GaAs MZI traveling wave modulator using doped epitaxial layers. Figure 1.7 shows the schematic of such a traveling wave MZI modulator [42]. The optical structure is a MZI utilizing multimode interference sections at the input and output for power splitting and combining.

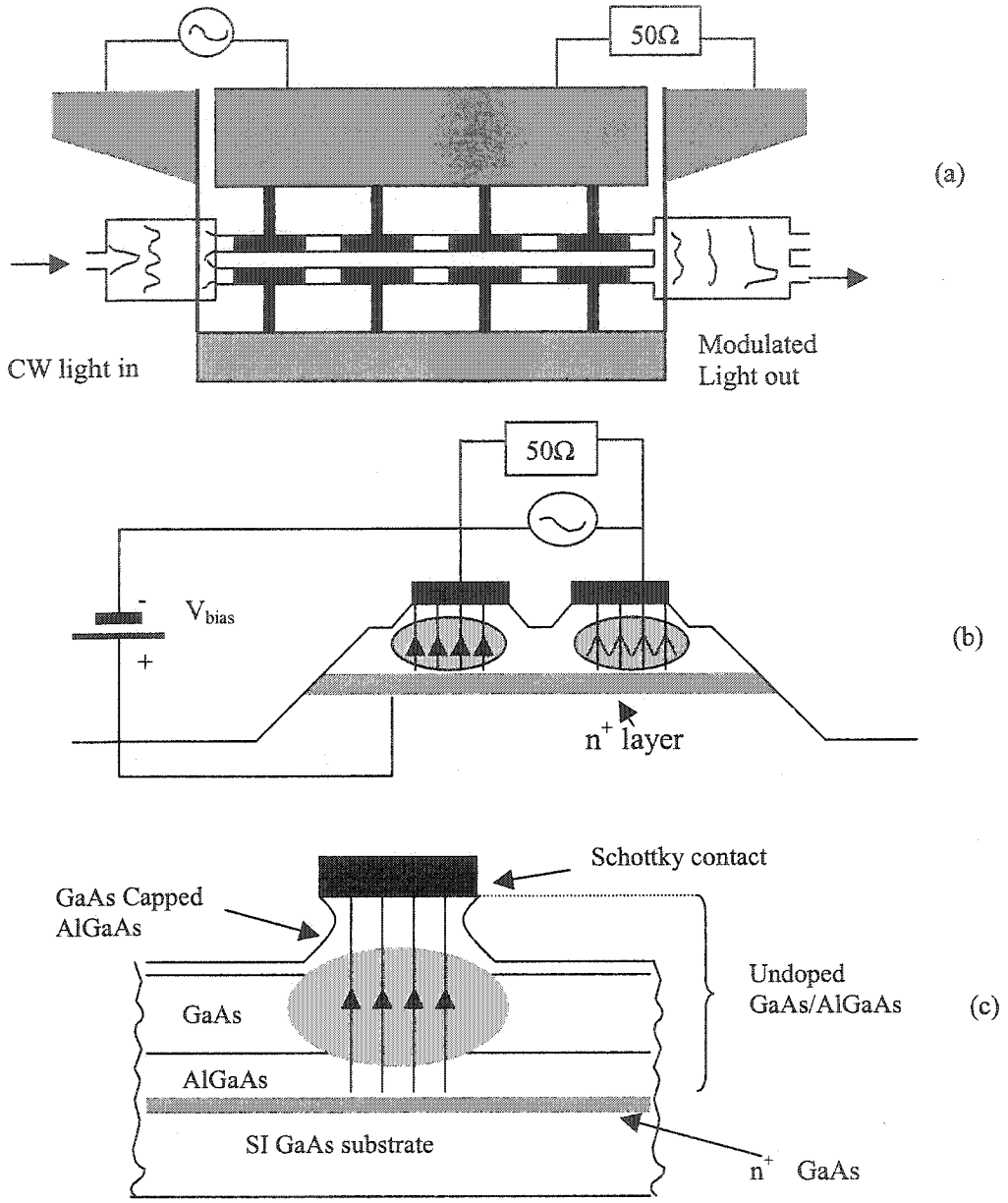

Figure 1.7 Schematic of traveling-wave Mach-Zehnder modulator using capacitively loaded CPS [42. Fig.1]. (a) top view (b) cross sectional view (c) layer structure.

GaAs/AlGaAs epitaxial layer is grown on a semi-insulating (SI) GaAs substrate. Underneath the GaAs core, there is a buried n^+ layer which works as a ground plane. The main electrode CPS is periodically loaded by narrow and small capacitive elements. The capacitive elements used are the reverse-biased capacitance of Schottky-i-n junction. This

contributes to good overlap between the vertical electric field and the optical mode. Such a device demonstrated an electrical 3 dB bandwidth of 50 GHz and Vπ of 13 V at 1530 nm [42]. However, unlike the parallel push pull, series push pull operation can only reduce the effective loading capacitance to reduce the half wave voltage to some degree, but cannot reduce it by a factor of 2. Consequently, The combination of a good overlap and series push pull operation still leads to a higher half wave voltage.

1.3 Thesis Objectives and Outline

External optical modulators of high bandwidth are key components in optical communication systems. Although TW-EA modulators have been demonstrated with the electrical bandwidth approaching 43Ghz and low drive voltage around 1.3V [18], there still exist some problems with this kind of modulator. First of all, chirping is an essential problem in EA modulators. Next, high insertion loss in produced. Besides, EA modulators cannot handle very large optical power. The space charge effect degrades the frequency response of EA modulators when the input light power is very high. Directional coupler switch modulators are usually used for lower speed switching applications [19]-[20]. For higher modulation switching, interferometric modulators are preferred because they permit higher modulation speed for a given drive voltage and a larger extinction ratio at high speed. Traveling wave electro-optic modulators based on GaAs have been demonstrated with the electrical bandwidth as high as 50 GHz and high V_π [40][42]. These values of V_π are still too high for a high-speed modulator.

The general objective of this research is to design, characterize, and optimize GaAs traveling wave electro-optic modulators through modeling and simulation. The design targets GaAs traveling wave electro-optic modulators with wide bandwidth over 40 GHz, half wave voltage less than 5 V, 50 Ω characteristic impedance and low optical insertion loss. The specific objectives include: (a) analyzing two kinds of slow wave electrodes, Planar Microstrip (PMS) Structure [34], and Coplanar Strip (CPS) lines periodically loaded with small capacitors [41]. For both structures, a thin n^+ is utilized in the layer structure with semi-insulating GaAs (SI-GaAs) as the substrate; (b) designing two kinds of electro-optic modulators, polarization conversion modulators and MZI intensity modulators; (c) investigating the optical properties of the designed waveguides, such as effective refractive index, group refractive index, mode size, and propagation loss as well as the coupling efficiency to a single mode fiber. This thesis is organized as follows:

Chapter 2 (**Theory of Electro-Optic Modulation**) presents the basic theory of electro-optic modulation. This includes a description of the electro-optic effect along with its physical origin. Three representative materials, KDP, $LiNbO_3$, and GaAs are introduced, and among them, GaAs is discussed in great detail, including its refractive index tensor. Intensity modulation and modulation chirp are also discussed.

Chapter 3 (**Theory and Design of Traveling Wave Electro-Optic Modulators**) presents several issues key to the design of traveling wave electro-optic modulators such as factors limiting the modulation bandwidth of traveling wave electro-optic modulators. In addition, slow wave structures are briefly reviewed.

Chapter 4 (**Design and Modeling of GaAs Traveling Wave Electro-optic Modulators Based on Planar Microstrip Structure**) provides an analysis of Planar Microstrip Structures (PMS) serving as the microwave electrodes in high speed GaAs traveling wave electro-optic modulators. The design of heterostructure optical layers, and of PMS slow wave electrodes are fully covered. More important, the design space of PMS slow wave structure serving as the GaAs traveling wave electro-optic modulator electrodes is characterized.

Chapter 5 (**Design and Modeling of GaAs Traveling Wave Electro-optic Modulators Based on Capacitively Loaded Coplanar Strips Using Doped Layers**) presents design and modelling results for GaAs traveling wave electro-optic modulators using different schemes. A MZI is integrated with periodically loaded coplanar strips and a n+ doping layer is used in the layer structure. The microwave properties of this slow wave structure are analyzed. The design space of loaded CPS lines are characterized. The potential of such a slow wave structure as the electrodes of high speed GaAs traveling wave electro-optic modulators is also discussed.

Chapter 6 (**Conclusion**) gives a review and concluding remarks on the design and modeling of traveling wave electro-optic modulators on GaAs. Research topics for future work are proposed. Thesis contributions are also mentioned.

CHAPTER 2

Theory of Electro-Optic Modulation

In this chapter, a number of topics related to electro-optic theory are discussed. The electro-optic effect and its physical origin are introduced, followed by a discussion of electro-optic materials with the help of three typical examples. Among them, GaAs is discussed in great detail, including its refractive index tensor. In addition, intensity modulation and modulation chirp are reviewed.

2.1 Electro-Optic Effect

Wave propagation in a crystal is usually expressed in terms of the so-called index ellipsoid [43]

$$\frac{x_1^2}{n_1^2}+\frac{x_2^2}{n_2^2}+\frac{x_3^2}{n_3^2}=1 \qquad (2.1)$$

where the directions x_1, x_2, x_3 are the principal dielectric axes - that is, the directions in the crystal along which D and E are parallel (D and E are the electric displacement vector and the electric field vector, respectively), n_1, n_2 , n_3 are the corresponding refractive indices.

When an electric field is applied to an electro-optic crystal, the refractive indices change. This phenomenon is known as the electro-optic effect. If the refractive index changes are proportional to the applied electric field, then it is called the linear electro-optic effect (the

Pockels effect). The linear electro-optic effect exists only in crystals that do not possess inversion symmetry.

A small change in the refractive indices by the application of an electric field leads to a small change in the shape, size and orientation of the index ellipsoid. Linear field-induced changes of the coefficients can be expressed as

$$\Delta(\frac{1}{n^2})_{ij} = \sum_k r_{ijk} E_k \tag{2.2}$$

or

$$(\Delta n)_{ij} = -\frac{n^3}{2} \sum_k r_{ijk} E_k \tag{2.3}$$

where E_k is the applied electric field, r_{ijk} are the components of the linear electro-optic tensor, and the subscripts i, j and k run from 1 to 3. The tensor is expressed in contracted matrix notation (an example is shown in (2.6) below). In the presence of an applied electric field, the general index ellipsoid becomes

$$\sum_{i,j,k} [\frac{1}{n_{ij}^2} + r_{ijk} E_k] x_i x_j = 1 \tag{2.4}$$

The linear electro-optic effect in piezoelectric crystals, above their acoustic resonance frequencies (i.e clamped electro-effect), appear mainly due to two types of microscopic interactions: an applied electric field modifies the electronic polarizability directly in the absence of lattice displacements, and an applied field produces a lattice displacement, which in turn modifies the electronic polarizability [44]. The first type, a purely electronic contribution to the electro-optic effect, is also the physical origin of optical mixing or second –harmonic generation and its magnitude can be obtained from second-harmonic

measurements. The second type, the lattice contribution to the electro-optic effect, can be determined from a combination of Raman scattering and infrared absorption measurements. In addition, there is a third contribution to the electro-optic coefficients when the frequency of the applied electric field falls below or near the acoustic resonant frequencies of the sample. The applied field strains the crystal via piezoelectric and or electrostrictive coupling, and the indices of refraction change due to the strain-optic effect. This component of electro-optic coefficients can be neglected if the frequency of the applied field is far above the acoustic resonant frequencies, in which case the crystal is effectively clamped.

2.2 Electro-Optic Materials

Electro-optic materials can be divided into the following groups, based on their general crystallographic and physical properties: 1) KDP, ADP and their isomorphs, 2) ABO_3 crystals similar to perovskites, 3) AB-type semiconductors with cubic or hexagonal ZnS structure, and 4) various miscellaneous crystals.

2.2.1 KDP Type Crystals

For KDP-ADP type, potassium dihydrogen phosphate (KDP) and ammonium dihydrogen phosphate (ADP) are the most widely known electro-optic crystals. Their general properties are reviewed elsewhere [45]. Both KDP and ADP belong to the piezoelectric point group $\bar{4}$2m at room temperature where they are normally used.

Here take KDP as an example to show the electro-optic properties of this type of materials. KDP is anisotropic and uniaxial: the fourfold axis of symmetry is the z (optic) axis while two mutually orthogonal twofold axes of symmetry lie in the plane normal to z; thus in the absence of applied electric field, the index ellipsoid equation (2.1) becomes:

$$\frac{x^2}{n_0^2}+\frac{y^2}{n_0^2}+\frac{z^2}{n_e^2}=1 \tag{2.5}$$

where $x_1=x$, $x_2=y$, $x_3=z$, and $n_1=n_2=n_0$, $n_3=n_e$. The electro-optic tensor is of the form

$$r_{ij}=\begin{vmatrix} 0 & 0 & 0 \\ 0 & 0 & 0 \\ 0 & 0 & 0 \\ r_{41} & 0 & 0 \\ 0 & r_{41} & 0 \\ 0 & 0 & r_{63} \end{vmatrix} \tag{2.6}$$

so the only nonvanishing electro-optic coefficients are $r_{41}=r_{52}$ and r_{63}.

From equation (2.4), (2.5) and (2.6), the equation of the index ellipsoid can be obtained in the presence of an arbitrary electric field $\mathbf{E}(E_x, E_y, E_z)$ as

$$\frac{x^2}{n_0^2}+\frac{y^2}{n_0^2}+\frac{z^2}{n_e^2}+2r_{41}E_x yz+2r_{41}E_y xz+2r_{63}E_z xy=1 \tag{2.7}$$

When an electric field is applied along the z-axis, the principal axes become z', x' and y' with z' parallel to z, and x' and y' at 45° to the x and y axes, as shown in Figure 2.1. The refractive index along z' remains n_e, while

$$n_{x'}=n_0+\frac{n_0^3}{2}r_{63}Ez \qquad\qquad n_{y'}=n_0-\frac{n_0^3}{2}r_{63}Ez \tag{2.8}$$

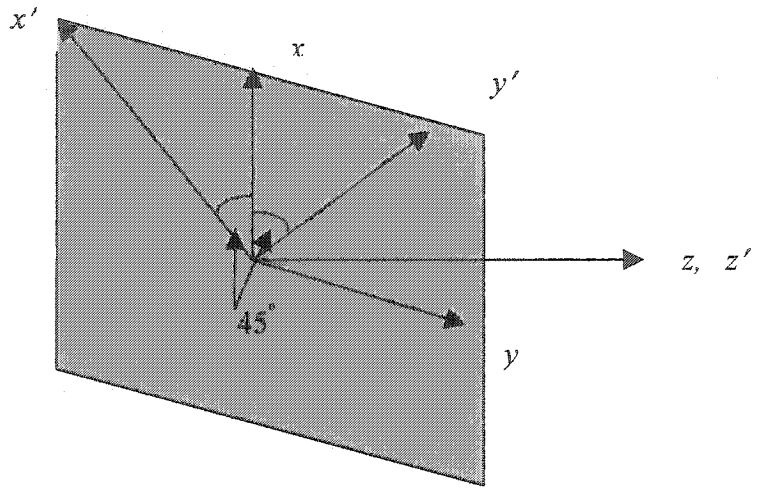

Figure 2.1 The x, y, and z axes of KDP and the x' and y' , and z' axes where z is the fourfold optic axis and x and y are the twofold axes of crystals with 42m symmetry.

If the overlap integral between the applied electric field and the optical mode is close to1, light polarized along x' or y' traveling through a crystal of length L experiences a phase modulation with index

$$\phi = \frac{\pi n_0^3 r_{63} E_z L}{\lambda} \tag{2.9}$$

Light traveling along z and initially polarized along x or y experiences a phase retardation

$$\Gamma = 2\phi \tag{2.10}$$

The voltage required to produce a phase retardation of π radians is called the half-wave voltage

$$V_\pi = \frac{\lambda}{2n_0^3 r_{63}} \tag{2.11}$$

2.2.2 ABO_3 Type Crystals

The perovskite family refers to the large group of crystals with structure resembling that of the mineral perovskite, $CaTiO_3$. Among them, the oxides $A^{2+}B^{4+}O_3$ and $A^{1+}B^{5+}O_3$ are attractive due to their strong electro-optic effect, such as $LiNbO_3$ and $LiTaO_3$.

$LiNbO_3$ is an anistropic uniaxial crystal with 3m crystal symmetry. From equation (2.1), the index ellipsoid without an applied electric field is reduced to

$$\frac{x^2}{n_0^2}+\frac{y^2}{n_0^2}+\frac{z^2}{n_e^2}=1 \tag{2.12}$$

where $x_1 = x$, $x_2 = y$, $x_3 = z$, and $n_1 = n_2 = n_0$, $n_3 = n_e$. The electro-optic tensor is

$$r_{ij} = \begin{vmatrix} 0 & -r_{22} & r_{13} \\ 0 & r_{22} & r_{13} \\ 0 & 0 & r_{33} \\ 0 & r_{51} & 0 \\ r_{51} & 0 & 0 \\ -r_{22} & 0 & 0 \end{vmatrix} \tag{2.13}$$

here the nonvanishing electro-optic coefficients are $r_{13} = r_{23}$, r_{22}, r_{33}, $r_{42} = r_{51}$, $r_{12} = r_{61} = -r_{22}$, thus depending on the orientation of the applied electric field, different electro-optic coefficients are possible. The most commonly used coefficient is r_{33}, which is the largest diagonal coefficient. Utilization of r_{33} can be achieved by applying an electric field along the z-axis, and two configurations are possible. For x-cut y propagating crystals, a horizontal electric field parallel to the surface of the crystal, i.e., along the z-axis, is utilized. This configuration, as shown in Figure 2.2 (a), modulates the TE polarized optical mode, in which the main electric field component of the optical mode is also parallel to the

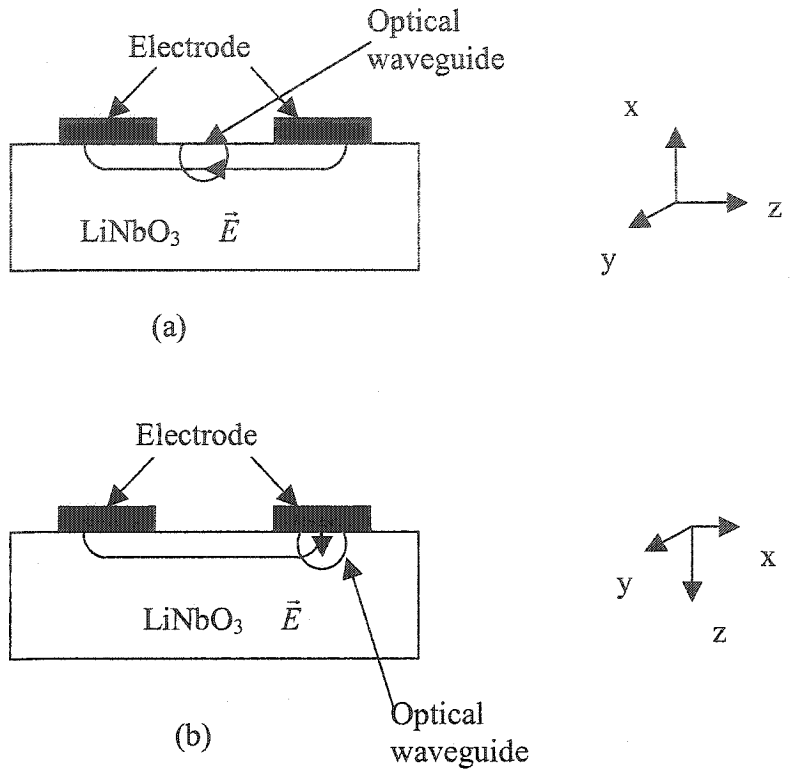

Figure 2.2 Typical electrode configuration for waveguide modulators on $LiNbO_3$: (a) for x-cut y propagating crystals, horizontal electric field is applied (b) for z-cut y propagating crystals, vertical electric field is used. The optical waveguide is also shown as a circular region.

surface of the crystal, i.e., it is along the z-axis of the crystal. For z-cut y propagating crystals, an electric field vertical to the surface of the crystal is used. This configuration, as shown in Figure 2.2 (b), modulates the TM polarized optical mode most efficiently. For TM modes, the main electric field component of the optical mode is also perpendicular to the surface of the crystal, i.e., it is along the z-axis of the crystal. For both configurations, the modulating external field and the main electric field component of the optical mode are parallel to each other and to the z-axis of the crystal.

With the applied field E_z along the z-axis, the index ellipsoid is obtained from equations (2.4), (2.12) and (2.13) as

$$\frac{x^2}{(n_0+\Delta n_0)^2}+\frac{y^2}{(n_0+\Delta n_0)^2}+\frac{z^2}{(n_e+\Delta n_e)^2}=1 \tag{2.14}$$

$$\Delta n_0=-\frac{n_0^3}{2}r_{13}E_z \tag{2.15}$$

$$\Delta n_e=-\frac{n_e^3}{2}r_{33}E_z \tag{2.16}$$

thus the resulting index change for light polarized along the z-axis, which sees the extraordinary index and strong r_{33} coefficient, is Δn_e.

2.2.3 AB Semiconductors

AB semiconductors are the group of binary compounds that crystallize in either the cubic ($\bar{4}3m$) zincblende structure or the hexagonal (6mm) wurtzite structure. The fact that III-V semiconductors are cubic and hence optically isotropic makes them particularly attractive for modulation applications. Among them, GaAs and InP and their alloys become the favorite materials due to their excellent optical properties and increasingly mature technology.

For III-V group semiconductors, like GaAs , equation (2.1) is simplified to

$$\frac{x^2}{n_0^2}+\frac{y^2}{n_0^2}+\frac{z^2}{n_0^2}=1 \tag{2.17}$$

where $x_1 = x$, $x_2 = y$; $x_3 = z$, and $n_1 = n_2 = n_3 = n_0$. Thus for GaAs, in the absence of an applied electric field, the refractive index tensor $n(0)$ can be expressed as

$$n(0) = \begin{vmatrix} n_0 & 0 & 0 \\ 0 & n_0 & 0 \\ 0 & 0 & n_0 \end{vmatrix} \tag{2.18}$$

The only nonvanishing electro-optic coefficients of GaAs are r_{41}, r_{52}, r_{63}, and $r_{41}=r_{52}=r_{63}$; the electro-optic tensor then becomes:

$$r_{ij} = \begin{vmatrix} 0 & 0 & 0 \\ 0 & 0 & 0 \\ 0 & 0 & 0 \\ r_{41} & 0 & 0 \\ 0 & r_{41} & 0 \\ 0 & 0 & r_{41} \end{vmatrix} \tag{2.19}$$

From equations (2.3), (2.18) and (2.19) the refractive index tensor $n(E)$ under the perturbation of an arbitrary applied electric field E (E_x, E_y, E_z),can be obtained as

$$\begin{aligned} n(E) &= n(0) + \Delta n_{ij} \\ &= \begin{vmatrix} n_0 & 0 & 0 \\ 0 & n_0 & 0 \\ 0 & 0 & n_0 \end{vmatrix} + \begin{vmatrix} 0 & \frac{-n_0^3}{2} r_{41} E_z & \frac{-n_0^3}{2} r_{41} E_y \\ \frac{-n_0^3}{2} r_{41} E_z & 0 & \frac{-n_0^3}{2} r_{41} E_x \\ \frac{-n_0^3}{2} r_{41} E_y & \frac{-n_0^3}{2} r_{41} E_x & 0 \end{vmatrix} \\ &= \begin{vmatrix} n_0 & \frac{-n_0^3}{2} r_{41} E_z & \frac{-n_0^3}{2} r_{41} E_y \\ \frac{-n_0^3}{2} r_{41} E_z & n_0 & \frac{-n_0^3}{2} r_{41} E_x \\ \frac{-n_0^3}{2} r_{41} E_y & \frac{-n_0^3}{2} r_{41} E_x & n_0 \end{vmatrix} \end{aligned} \tag{2.20}$$

It is noted that *n(E)* here is the refractive index tensor in the old principle axes(x,y,z) in the presence of an applied electric field. In order to understand better the effect of the applied electric field on light propagation, the refractive index tensor in the new principle axes (x′, y′, z′), $n'(E)$ needs to be known. The new set of principle axes can always be found by a coordinate system rotation, which is known as the principle-axis transformation of a quadratic form. Suppose the eigenvalues of *n(E)* are $n_{x'}, n_{y'}, n_{z'}$, while X′, Y′, Z′ are its eigenvectors, then $n'(E)$ can be expressed by

$$n'(E) = \begin{vmatrix} n_{x'} & 0 & 0 \\ 0 & n_{y'} & 0 \\ 0 & 0 & n_{z'} \end{vmatrix} \tag{2.21}$$

where X′, Y′, Z′ are the new principle axis vectors, and they are mutually orthogonal. Once the refractive index tensors are known both in the old principle axes and in the new principle axes, light propagation in GaAs in the presence of an applied electric field can be thoroughly understood.

With an electric field applied to the crystal, the index ellipsoid of equation (2.4) becomes:

$$\frac{x^2}{n_0^2} + \frac{y^2}{n_0^2} + \frac{z^2}{n_0^2} + 2r_{41}(E_x yz + E_y xz + E_z xy) = 1 \tag{2.22}$$

Thus the application of an electric field in a general direction relative to the crystal axes makes the initially isotropic crystals biaxial.

Taking the crystal growth and practical application of GaAs into consideration, three orientations are of interest: a) the applied electric field E is along the [001] direction and

light propagates along the $[\bar{1}\bar{1}0]$ direction, b) the applied electric field is along the [110] direction and light propagates along the $[\bar{1}10]$ direction c) the applied electric field is along the [111] direction and light propagates normal to the [111] direction. Each case will be considered in turn, with appropriate orientation of epitaxial layers.

(a) E along the [001] direction, and epitaxial layers grown on the (001) plane of GaAs

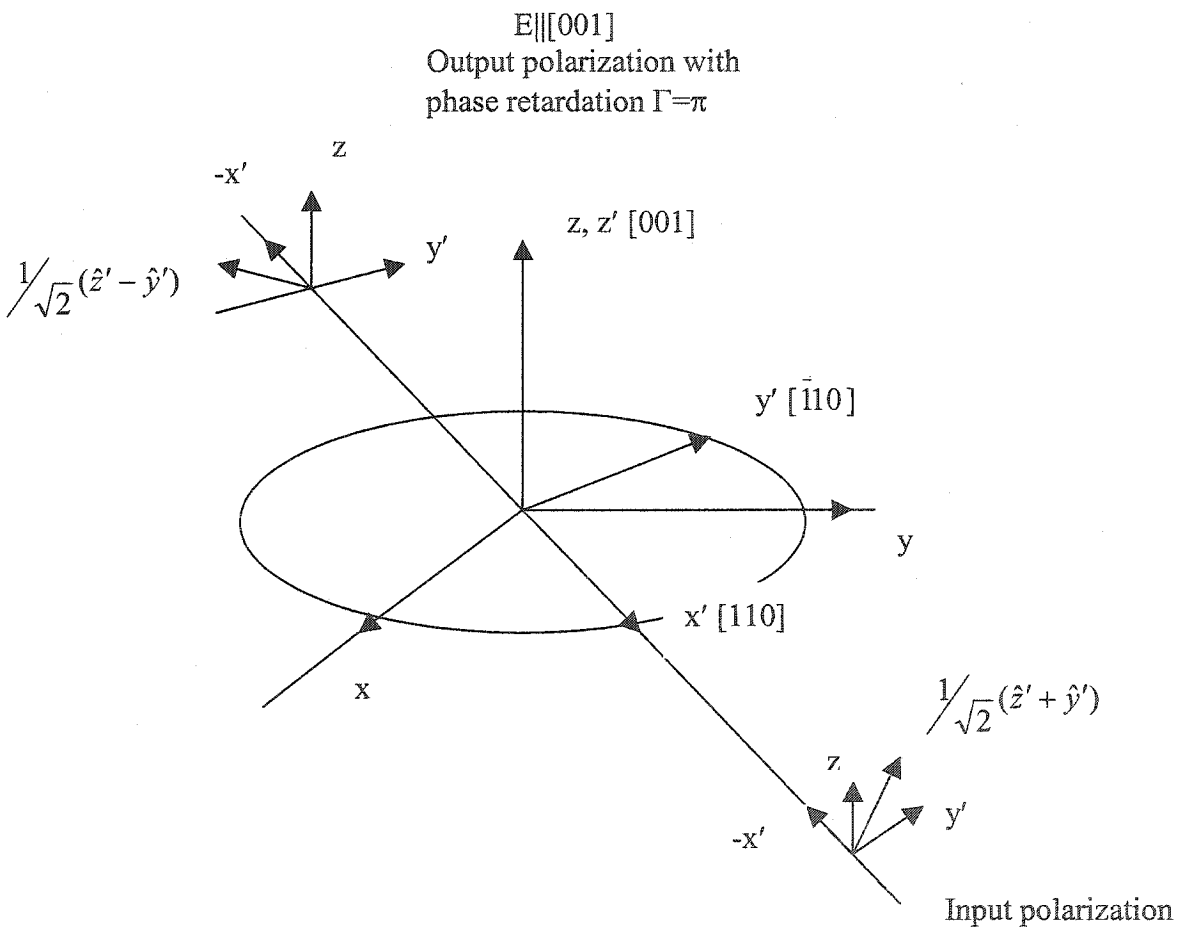

Figure 2.3 Index ellipsoid and polarization transformation in a zincblende crystal family for an applied electric field in the [001] direction and light propagating in the $[\bar{1}\bar{1}0]$ direction.

For E along the [001] (E_x= E_y=0, E_z=E), the index ellipsoid equation (2.22) becomes:

$$\frac{x^2}{n_0^2}+\frac{y^2}{n_0^2}+\frac{z^2}{n_0^2}+2r_{41}Exy=1 \tag{2.23}$$

The new principal axes are x', y', z', and z' is parallel to z along the [001] direction, while x', y' are along [110] and [$\bar{1}$10] respectively (at 45° to the x and y axes), as shown in Figure 2.3.

The new principal indexes of refraction become:

$$n_{x'}=n_0+\frac{n_0^3}{2}r_{41}E\ ,\quad n_{y'}=n_0-\frac{n_0^3}{2}r_{41}E\quad ,\quad n_{z'}=n_0 \tag{2.24}$$

It is seen from the above that the application of an electric field causes a refractive index change in the [110] direction and thus affects the TE mode but does not affect the refractive index in the [001] direction along the field of the TM mode. The input polarization of light propagating in the [$\bar{1}\bar{1}$0] will have a phase modulation for polarization along the [$\bar{1}$10] direction and a polarization modulation for polarization 45° to the [001] direction, but have no phase retardation or polarization modulation along the [001] direction. In other words, a vertically applied electric field to an (001)-oriented crystal will only modulate the TE mode of the optical waveguide. The phase retardation for light propagating along the [$\bar{1}\bar{1}$0] and E along [001] is given by [46], [24]:

$$\phi_{[\bar{1}\bar{1}0]}=\frac{\pi L}{\lambda d}n_0^3r_{41}V\xi \tag{2.25}$$

where λ is the optical wavelength, V is the applied voltage, L is the interaction length between the optical and electrical signals, d is the space charge width or the electrode gap, ξ is the overlap integral between the applied electric field and the optical mode, given by:

$$\xi = \frac{d}{V}\iint E\left|E_{opt}\right|^2 dA \qquad (2.26)$$

where E_{opt} is the normalized optical electric field and the integration is over the cross sectional area of the optical mode, A.

For E along [001], two electrode configurations are possible. One is the microstrip configuration using a p-i-n structure as shown in Figure 2.4 (a), the other is a coplanar strip electrode configuration shown in Figure 2.4 (b). In the p-i-n structure, the metal electrodes are in contact to the p-layer and the back of the substrate providing the electric field along the [001] direction. In the coplanar strip configuration Figure 2.4 (b), the optical guide is dielectrically loaded with one electrode crossing over the guide. This provides electric field predominantly along the [001] direction.

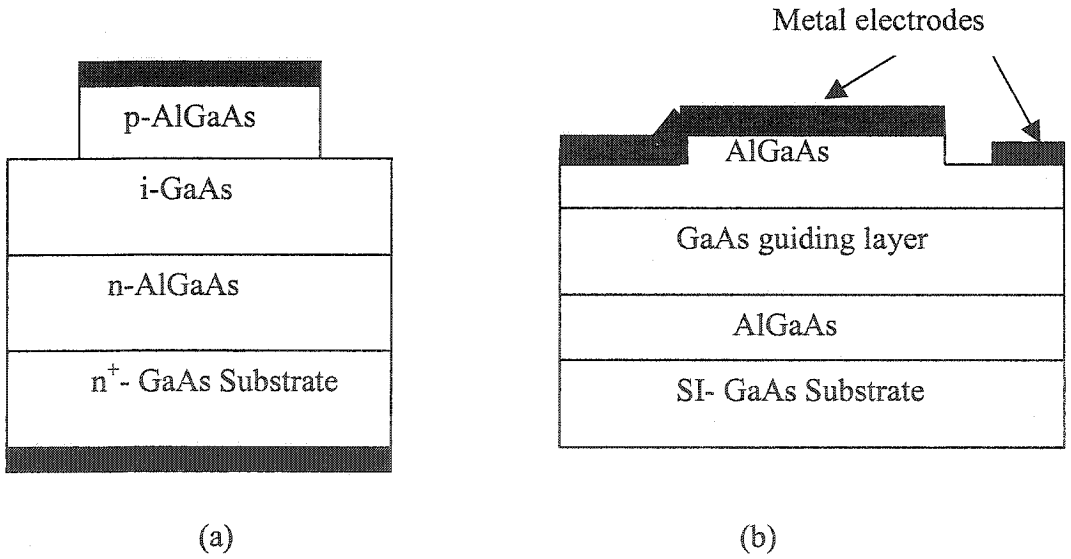

Figure 2.4 Two electrode configurations for applied electric field along [001] direction. (a) Cross section of a p-i-n waveguide microstrip configuration modulator on n+(001) GaAs substrate with a double heterostructure cladding layers of AlGaAs of the p and n type. (b) Cross section of a double heterostructure waveguide modulator fabricated on semi-insulating GaAs (001) substrate with coplanar strip electrodes.

(b) E along the [110] direction, and epitaxial layers grown on the (001) plane of GaAs

For E along [110] direction ($E_x = E_y = E/\sqrt{2}$, $E_z = 0$), the index ellipsoid equation (2.22) becomes:

$$\frac{x^2}{n_0^2} + \frac{y^2}{n_0^2} + \frac{z^2}{n_0^2} + \sqrt{2} r_{41} E(yz + zx) = 1 \qquad (2.27)$$

The new principal axes are x', y', z', and z' is along the $[1\bar{1}0]$ direction, while x' and y', the two orthogonal axes located in the plane of $(1\bar{1}0)$, are at 45° to –z and z respectively, as shown in Figure 2.5. The new principal indexes of refraction become:

$$n_{x'} = n_0 + \frac{n_0^3}{2} r_{41} E \ , \quad n_{y'} = n_0 - \frac{n_0^3}{2} r_{41} E \ , \quad n_{z'} = n_0 \qquad (2.28)$$

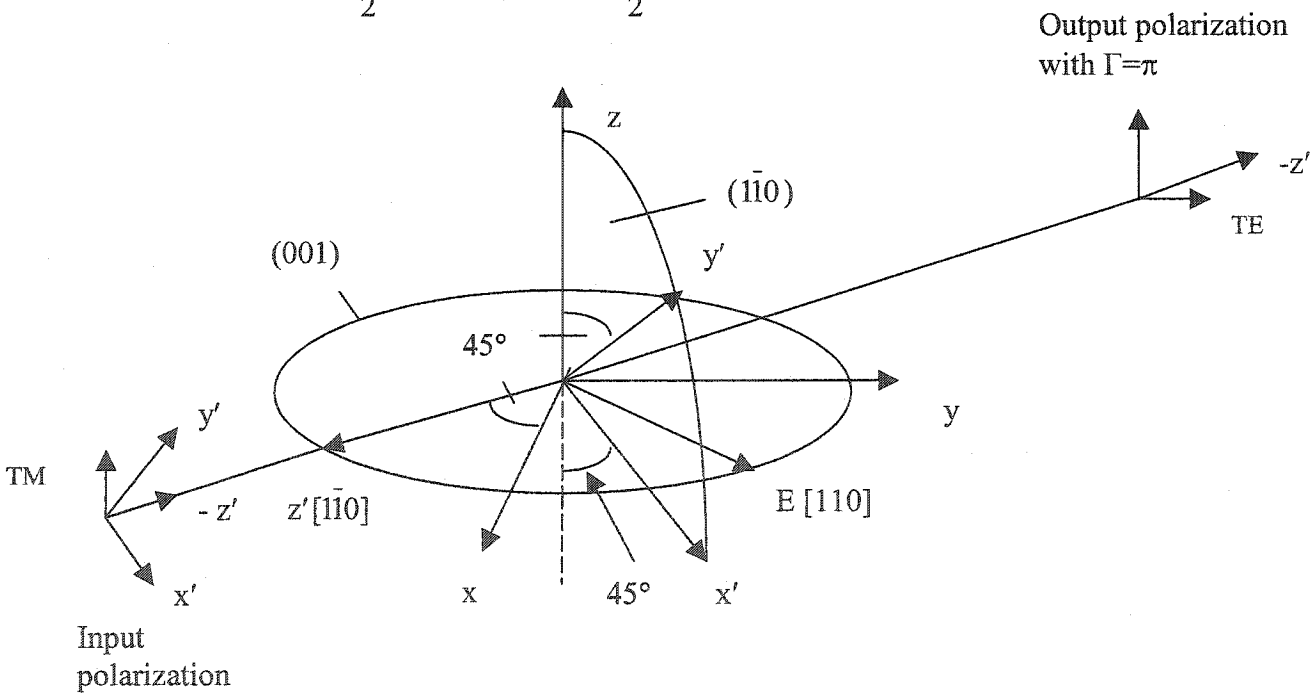

Figure 2.5 Index ellipsoid and polarization transformation in a zincblende crystal family for the applied electric field in the [110] direction and light propagating in the $[1\bar{1}0]$ direction. In this orientation, the projection of $\vec{E}_o$ is on two electro-optically active axes x′ and y′ rather just one for the case with E ‖ [001] and propagating along $[1\bar{1}0]$.

As light propagates along $[\bar{1}10]$ (-z') with either TE or TM polarization, it will project on both the fast and slow axis of the new index ellipsoid, thus giving a push-pull mode of operation that alters the polarization state of input optical signal. The application of half wave voltage can convert TE (TM) mode to TM (TE) mode. The phase retardation for light propagating along $[\bar{1}10]$ and E along [110] is [46][24]:

$$\phi_{[\bar{1}10]} = 2\frac{\pi L}{\lambda d} n_0^3 r_{41} V \xi \tag{2.29}$$

with the definition of the terms given above. The phase retardation for this orientation is a factor of 2 greater than the former case with E|| [001] . This is the optimum orientation for maximum phase retardation per volt.

For E along [110], a coplanar strip electrode configuration is utilized with a ridge single heterostructure optical guide. The electrodes are on either side of the guide as shown in Figure 2.6. This provides a predominantly horizontal electric field in the [110] direction.

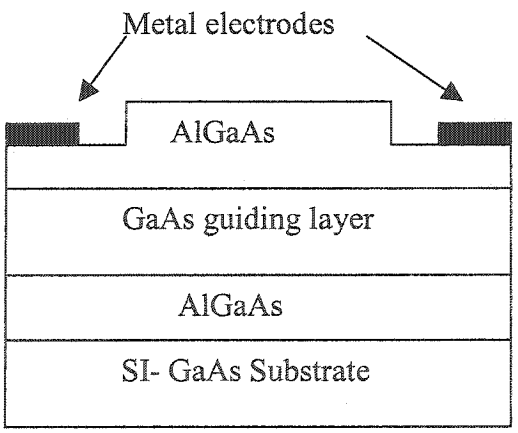

Figure 2.6 Cross section of a double heterostructure waveguide modulator fabricated on semi-insulating GaAs (001) substrate with coplanar strip electrodes. The electrodes on either side of the optical waveguide provide the electric field in the [110] direction.

(c) E along the [111] direction, and epitaxial layers grown on the (111) plane of GaAs

For E applied along the [111] direction, in other words, $E_x = E_y = E_z = \frac{E}{\sqrt{3}}$, the index ellipsoid equation (2.22) reduces to

$$\frac{x^2}{n_0^2} + \frac{y^2}{n_0^2} + \frac{z^2}{n_0^2} + \frac{2}{\sqrt{3}} r_{41} E(yz + zx + xy) = 1 \qquad (2.30)$$

The new principal axes are x', y', z', and z' is along the [111] direction, parallel to the direction of the applied electric field, while x' and y' are two orthogonal axes located in the plane normal to [111], as shown in Figure 2.7. The new principal indices of refraction become:

$$n_{x'} = n_{y'} = n_0 + \frac{n_0^3}{2\sqrt{3}} r_{41} E \quad , \quad n_{z'} = n_0 - \frac{n_0^3}{\sqrt{3}} r_{41} E \qquad (2.31)$$

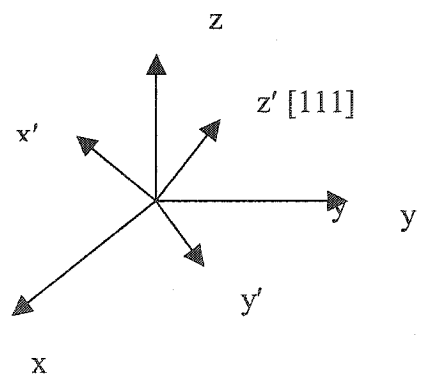

Figure 2.7 The index ellipsoid of a zincblende crystal family for the applied electric field in the [111] direction.

For light propagating along x' (or y') and polarized along z', a maximum change in index of refraction of $-\frac{n_0^3}{\sqrt{3}} r_{41} E$ is found. The advantage over using a field in (001) plane is

$2/\sqrt{3}$ and a given phase modulation can be obtained with $3/4$ of the drive power. This crystal orientation is one that gives the maximum change in index of refraction for a specific linear polarization and hence is most suitable for phase modulation.

2.3 Intensity Modulation

In current optical communication systems, Intensity modulation/Direct detection is the most popular modulation/detection scheme due to its low cost and simple transmitter and receiver circuitry. Therefore some means are necessary to convert electro-optically induced phase modulation or polarization modulation into intensity modulation. Here, we briefly discuss some basic conversion schemes, taking GaAs as an example.

2.3.1 Polarization Modulation Conversion

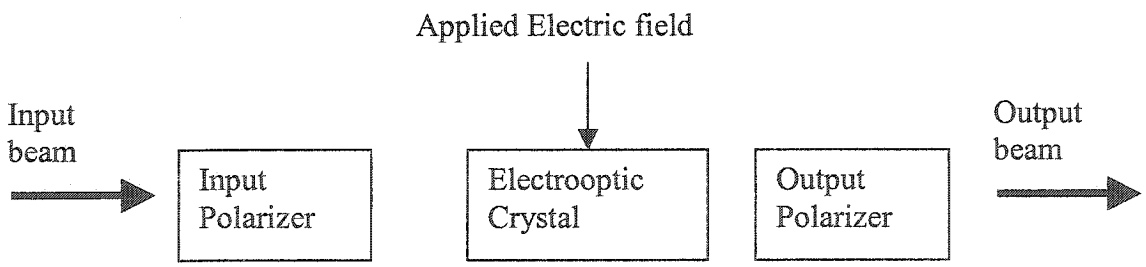

Figure 2.8 A simple electro-optic intensity modulator.

The structure shown in Figure 2.8 provides the easiest conversion scheme. With linear polarizers placed before and after the electro-optic waveguide, the conversion from polarization modulation to intensity modulation has been accomplished; the polarizer before

the waveguide selects one polarization state and eliminates the other, while the polarizer after the waveguide completes the intensity modulation.

To be specific, we show how this arrangement is achieved using a GaAs crystal. Suppose the waveguide is the one shown in Figure 2.4 (a) or (b). An electric field is applied along the [001] direction, as shown in Figure 2.3. With the input polarizer in the direction of $1/\sqrt{2}(\hat{z}'+\hat{y}')$, and the output polarizer along the direction of $1/\sqrt{2}(\hat{z}'-\hat{y}')$, polarization modulation is converted into intensity modulation. After passing the input polarizer, the optical field is polarized along $1/2(\hat{z}'+\hat{y}')$ at the input face of the waveguide, thus having equal-in-phase components along z′ and y′ that are taken as:

$$\begin{aligned} e_{z'} &= A\cos\omega t \\ e_{y'} &= A\cos\omega t \end{aligned} \tag{2.32}$$

or , using the complex amplitude notation :

$$\begin{aligned} E_{z'}(0) &= A \\ E_{y'}(0) &= A \end{aligned} \tag{2.33}$$

The incident intensity is thus:

$$I_i \propto \mathrm{E}\bullet\mathrm{E}^* = \left|E_{z'}(0)\right|^2 + \left|E_{y'}(0)\right|^2 = 2A^2 \tag{2.34}$$

The phase retardation at the output plane x′=L between the two components can be obtained based on equations (2.24) and (2.25)

$$\Gamma = \phi_{y'} - \phi_{z'} = \frac{\pi L}{\lambda d} n_0^3 r_{41} V \xi \tag{2.35}$$

thus z′ and y′ components at the output face x′=L can be expressed

$$\begin{aligned} E_{y'}(L) &= Ae^{-i\Gamma} \\ E_{z'}(L) &= A \end{aligned} \tag{2.36}$$

The total field emerging from the output polarizer is the sum of $E_{z'}(L)$ and $E_{y'}(L)$

$$E_o = -\frac{A}{\sqrt{2}}(e^{-i\Gamma} - 1) = \sqrt{2} A \sin\frac{\Gamma}{2} e^{i(\frac{\pi}{2} - \frac{\Gamma}{2})} \tag{2.37}$$

which corresponds to an output intensity

$$I_o \propto [E_o E_o^*] = \frac{A^2}{2}[(e^{-i\Gamma} - 1)(e^{i\Gamma} - 1)] = 2A^2 \sin^2\frac{\Gamma}{2} \tag{2.38}$$

where the proportionality constant is the same as in equation(2.34). The ratio of the output intensity to the input is thus

$$\frac{I_o}{I_i} = \sin^2\frac{\Gamma}{2} = \frac{1}{2} + \frac{1}{2}\sin\Gamma_{ac} = \frac{1}{2} + (\frac{I_o}{I_i})_{ac} \tag{2.39}$$

with

$$\Gamma = \Gamma_{dc} + \Gamma_{ac} = \frac{\pi}{2} + \frac{\pi}{V_\pi} V(\omega) \tag{2.40}$$

where Γ dc is induced by the dc bias to the quadrature operating point, V_π is the half-wave voltage (the voltage required to produce a π phase shift), and $V(\omega)$ is the small signal modulation voltage.

Suppose that a small sinusoidal modulation voltage is applied $V(\omega) = V_m \sin(\omega t)$, thus equation (2.39) becomes:

$$\frac{I_o}{I_i} = \frac{1}{2} + \frac{1}{2}\sin\Gamma_{ac} = \frac{1}{2}(1 + \sin(\frac{\pi}{V_\pi} V_m \sin(\omega t))) \tag{2.41}$$

which , for $\frac{\pi}{V_\pi} V_m \ll 1$, becomes:

$$\frac{I_o}{I_i} \approx \frac{1}{2}(1 + \frac{\pi}{V_\pi} V_m \sin(\omega t)) \tag{2.42}$$

so that the intensity modulation is a linear replica of the modulating voltage $V(\omega)$. If the condition $\frac{\pi}{V_\pi} V_m \ll 1$ is not fulfilled, it follows from Equation (2.41) that the intensity variation is distorted and will contain an appreciable amount of the higher harmonics.

The above simple scheme converts polarization modulation to intensity modulation. The disadvantage for this scheme is that external polarizers cause higher optical loss and high cost, and add complexity for integration with a laser source.

2.3.2 Mach-Zehnder Intensity Modulators

Integrated intensity modulators have been made using a variety of waveguide structures. Among them, the most popular are the directional coupler and Mach-Zehnder interferometer (MZI) integrated with phase modulation on each arm, as shown in Figure

1.4. Although the first gigabit per second digital fiber optic transmission experiments investigating external modulation used directional coupler switch modulators, MZI modulators have come to be preferred because they permit higher modulation speed for a given drive voltage and a larger extinction ratio at high speed. Various kinds of combination of waveguide and electrodes can be taken to set up MZI modulators.

(a) CPS MZI

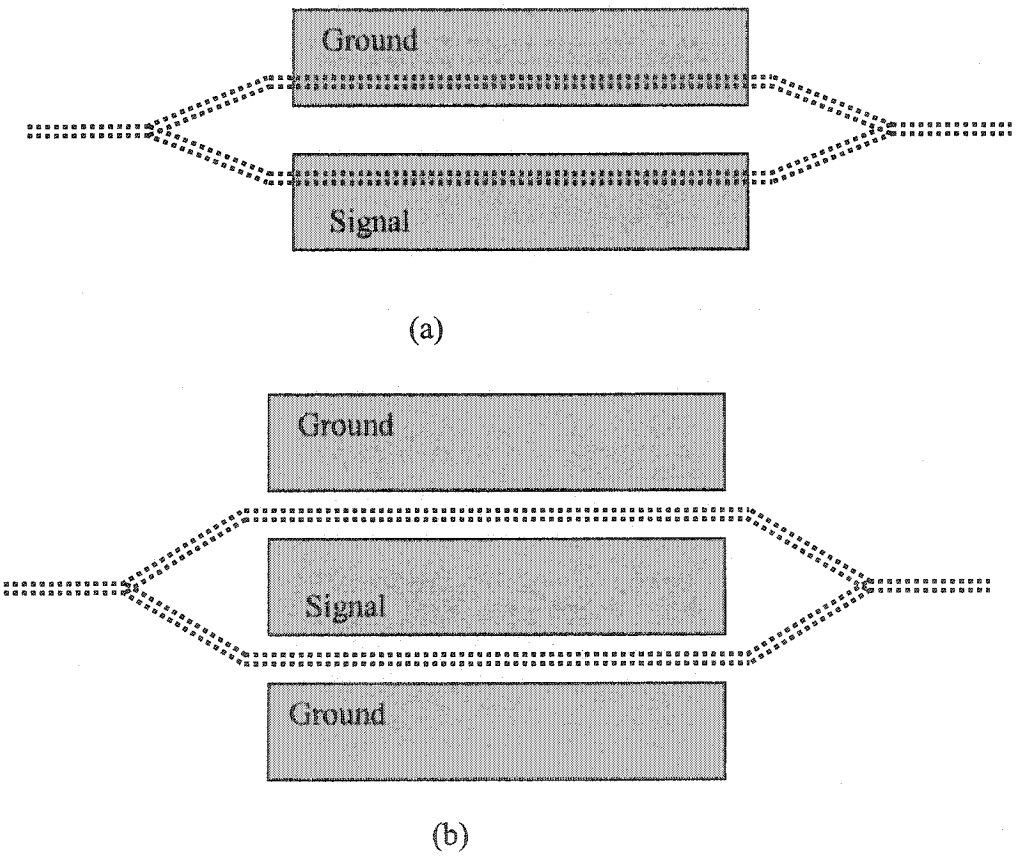

Figure 2.9 MZI modulator integrated with different electrodes: (a) integrated with CPS (b) integrated with CPW.

Figure 2.9 (a) shows a MZI integrated with a coplanar strip (CPS) used as the RF electrode. The two arms of MZI are placed under the inner edge of signal and ground electrodes, and

the cross section of the device in the optical waveguide area and relative position of the RF electrode to optical waveguide are illustrated in Figure 2.4. In this case, the applied electric field is along the [001] direction (see Figure 2.3), so only TE mode can be modulated, and the phase modulation in each arm of this device is governed by equation (2.25). This device operates as follows: In the absence of any applied electric field, light entering the single mode waveguide is divided equally into the two identical waveguide arms with zero relative phase difference between the split fields, and the two signal propagates the same length of optical paths thus are constructively added at the output Y-branch. When the half wave voltage is applied to the electrodes, a π phase shift is introduced between the separated fields. The split fields are added destructively at the output Y-branch with half wave voltage applied.

(b) CPW MZI

As shown in Figure 2.9 (b), MZI can also be integrated with CPW with the two arms of MZI placed symmetrically relative to the center (signal) electrode, and the cross section of optical waveguide is that shown in Figure 2.6. An electric field is applied along the [110] direction (see Figure 2.5), thus either the TE or the TM mode can be modulated.

Suppose that the complex amplitude of the electric field at the input y-junction is $E(0) = A$ and ϕ_0 is the phase difference between the two arms when no electric field is applied, then the incident intensity can be expressed as below

$$I_i \propto \mathrm{E} \bullet \mathrm{E}^* = |E(0)|^2 = A^2 \qquad (2.43)$$

With an applied voltage, phase changes are induced on each arm. At the output y branch, the complex amplitude of the electric field of each arm is obtained:

$$E_1(L) = \frac{A}{2} e^{-i\phi(V_1)} \tag{2.44}$$

$$E_2(L) = \frac{A}{2} e^{-i(\phi(V_2)-\phi_0)} \tag{2.45}$$

where $\phi(V_1)$ and $\phi(V_2)$ are the phase induced by the voltages $V_1$and V_2 applied to each arm, and L is the length of interaction between the optical signal and the electrical signal. The values of $\phi(V_1)$ and $\phi(V_2)$ are calculated using equation (2.25) or (2.29) depending on the situation.

From equations (2.44) and (2.45), the complex amplitude of the total field from the output Y- branch can be expressed:

$$E_o(L) = E_1(L) + E_2(L) = \frac{A}{2} e^{-i\phi(V_1)} + \frac{A}{2} e^{-i(\phi(V_2)-\phi_0)}$$

$$= A\cos\left(\frac{\phi(V_1) - \phi(V_2) + \phi_0}{2}\right) e^{i(\phi(V_1)+\phi(V_2)-\phi_0)/2} \tag{2.46}$$

The output intensity is then:

$$I_o \propto [E_o E_o^*] = A^2 \cos^2\left(\frac{\phi(V_1) - \phi(V_2) + \phi_0}{2}\right) \tag{2.47}$$

where the proportionality constant is the same as in equation (2.43). The ratio of the output intensity to the input is thus:

$$\frac{I_o}{I_i} = \cos^2\left(\frac{\phi(V_1) - \phi(V_2) + \phi_0}{2}\right) = (1/2)(1+\cos(\phi(V_1) - \phi(V_2) + \phi_0)) \tag{2.48}$$

2.4 Modulation Chirp

As discussed before, direct modulation of a semiconductor laser causes the frequency chirp and thus limits the transmission bandwidth of single –mode fiber systems. On the other hand, external modulators theoretically may be operated without producing any chirp or producing negative chirp as needed on some occasions.

By definition, the chirp parameter α of a modulator is the ratio of the phase modulation to the amplitude modulation [47] :

$$\alpha = \frac{(d\phi / dt)}{((1/E)(dE/dt))} \tag{2.49}$$

or

$$\alpha = \frac{2(d\phi / dt)}{((1/I)(dI/dt))} \tag{2.50}$$

where E and ϕ are the amplitude and phase of an electric field, respectively, and I is the intensity. Here, Modulation chirp in polarization conversion modulators and in Mach Zehnder intensity modulators are investigated respectively.

2.4.1 Chirp in Polarization Modulation Conversion

As discussed in section 2.2.1, the output electric field in the case of polarization conversion can be expressed by equation (2.37) with the amplitude $|E_o| = \sqrt{2}A\sin\frac{\Gamma}{2}$ and the phase

$\phi = \frac{\pi}{2} - \frac{\Gamma}{2}$. According to the definition of the chirp parameter α (equation 2.49), α for this case can be obtained

$$\alpha = -\tan\frac{\Gamma}{2} \tag{2.51}$$

If the modulator is dc biased to the quadrature operating point, and a small sinusoidal modulation voltage is applied $V(f) = V_m \sin(\omega t)$, then based on equation (2.40), the above equation can be rewritten as follows

$$\alpha = -\tan(\frac{\pi}{4} + \frac{\Gamma_{ac}}{2}) = -\frac{\cos\frac{\Gamma_{ac}}{2} + \sin\frac{\Gamma_{ac}}{2}}{\cos\frac{\Gamma_{ac}}{2} - \sin\frac{\Gamma_{ac}}{2}} \tag{2.52}$$

with $\Gamma_{ac} = \frac{\pi}{V_\pi} V_m \sin(\omega t)$. For $\frac{\pi}{V_\pi} V_m \ll 1$, $\frac{\Gamma_{ac}}{2} \ll 1$, then the above equation be simplified to

$$\alpha \approx -\frac{1 + \frac{\Gamma_{ac}}{2}}{1 - \frac{\Gamma_{ac}}{2}} = -\frac{1 + \frac{\pi}{2V_\pi} V_m \sin(\omega t)}{1 - \frac{\pi}{2V_\pi} V_m \sin(\omega t)} \tag{2.53}$$

The above equation along with the condition $\frac{\pi}{V_\pi} V_m \ll 1$ indicates that α is close to –1.

In conclusion, polarization modulation conversion can produce small negative chirp.

2.4.2 Chirp in Mach-Zehnder Intensity Modulators

In section (2.3.1), the common case of Mach-Zehnder intensity modulators is discussed, that is the input optical power is equally split into and out of two arms. Here, Mach-Zehnder intensity modulators are being dealt with more generally.

In the following, we discuss and explore what happens to a Mach-Zehnder Modulator when the split ratio deviates from 1:1 with regards to chirp. Suppose the amplitude of the electric field in the input waveguide is E_0, deviation quantity from $\frac{E_0}{\sqrt{2}}$ is $a\frac{E_0}{\sqrt{2}}$, and $0 \le |a| < 1$, then one arm input electric field $E_1 = \frac{E_0}{\sqrt{2}}(1-a)$ and the other arm input electric field $E_2 = \frac{E_0}{\sqrt{2}}(1+a)$, and the output combination ratio is 1, as shown in Figure 2.10.

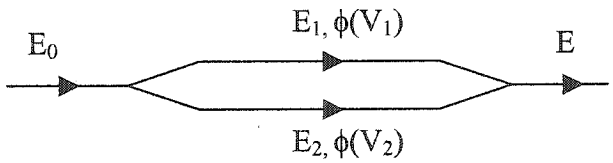

Figure 2.10 Schematic structure of Mach-Zehnder interferometer type modulator.

Assume that the phase difference between the two arms when no electric field is applied is zero. The incoming optical field undergoes a phase change in each arm of the MZ modulator, with the respective change induced by the applied voltage on the corresponding arm, thus the output electric field E is given by:

$$E = \frac{E_0}{2}(1-a)\exp(-i\phi(V_1)) + \frac{E_0}{2}(1+a)\exp(-i\phi(V_2)) \qquad (2.54)$$

where $\phi(V_1)$ and $\phi(V_2)$ are the phase shifts induced by the voltages $V_1$and V_2 applied to each arm.

If

$$\Gamma = (\phi(V_1) - \phi(V_2))/2 \tag{2.55}$$

$$\overline{\Gamma} = (\phi(V_1) + \phi(V_2))/2 \tag{2.56}$$

then equation (2.54) is reduced to:

$$E = E_0(\cos(\Gamma) + ia\sin(\Gamma))\exp(-i\overline{\Gamma}) \tag{2.57}$$

Assume that $E_0(\cos(\Gamma) + ia\sin(\Gamma)) = A\exp(i\phi)$, then we can obtain:

$$A = E_0(\cos^2(\Gamma) + a^2\sin^2(\Gamma))^{\frac{1}{2}} \tag{2.58}$$

$$\Phi = \arctan(a\tan(\Gamma)) \tag{2.59}$$

With equations (2.58) and (5.29), equation (2.57) becomes:

$$E = A\exp(i(-\overline{\Gamma} + \Phi)) \tag{2.60}$$

Thus the phase of the output light is $-\overline{\Gamma} + \Phi$, and the amplitude of the output field is A given by equation (2.58). Based on the above three equations and equation (2.49), an analytical expression for α in Mach-Zehnder intensity modulator can be obtained with tedious mathematics. Here instead of deriving this complex expression, we discuss several cases of common interest.

When V_1=-V_2 is satisfied, $\overline{\Gamma}$ is zero, thus the phase of the output light becomes Φ. The α parameter defined by equation (2.49) can be calculated by using equations (2.58) and (2.59)

$$\alpha = \frac{2a}{(a^2 - 1)\sin 2\Gamma} \tag{2.61}$$

Based on the above equations, some conclusions can be drawn:

A. If a=0, then α=0. When the light is equally split into both arms, the phase modulation can be completely compensated if the voltage applied to the arms of the MZI are of opposite polarity and of equal amplitude, V_1=-V_2, such as a push-pull operation of the MZI modulators. This achieves zero chirp modulation

B. When $a \neq 0$, then α might be positive or negative, which depends on both a and Γ. When light is split unequally into the two arms, both cases of "red shift" and "blue shift" chirping possibly occur even if the voltage applied to the arms of the MZI are of opposite polarity and of equal amplitude, V_1=-V_2.

If a=0 and V_1≠-V_2 are satisfied, then $\overline{\Gamma} \neq 0$, $\Phi = 0$ and $A = E_0 \cos\Gamma$. The α parameter in this case can be obtained

$$\alpha = \frac{A^* d(-\overline{\Gamma})/dt}{dA/dt} = \frac{d\overline{\Gamma}/dt}{d\Gamma/dt}\cot\Gamma \tag{2.62}$$

Assume that the arms of the modulator are driven with $V_1(t) = V_1 \sin(\omega t) + V_b$ and $V_2(t) = V_2 \sin(\omega t)$, V_b is the bias voltage, then Γ and $\overline{\Gamma}$ can be expressed as

$$\begin{aligned} \Gamma &= \frac{1}{2}\frac{\pi}{V_\pi}(V_1 \sin(\omega t) - V_2 \sin(\omega t) + V_b) \\ \overline{\Gamma} &= \frac{1}{2}\frac{\pi}{V_\pi}(V_1 \sin(\omega t) + V_2 \sin(\omega t) + V_b) \end{aligned} \tag{2.63}$$

thus equation (2.62) becomes

$$\alpha = \left(\frac{V_1 + V_2}{V_1 - V_2}\right)\cot\left(\frac{1}{2}\frac{\pi}{V_\pi}(V_1 \sin(\omega t) - V_2 \sin(\omega t) + V_b)\right) \qquad (2.64)$$

Since V_b usually refers to the dc bias to the quadrature operating point, $\frac{\pi}{V_\pi}V_b = \frac{\pi}{2}$. For small signal case, $V_1 << V_b$ and $V_2 << V_b$, then equation (2.64) can be simplified as

$$\alpha = \frac{V_1 + V_2}{V_1 - V_2} \qquad (2.65)$$

Although this expression applies rigorously only in the small-signal regime, it is accurate to relatively large values of the modulation depth because of the shape of the Mach-Zehnder switching curve. It is noted that choosing the relative magnitude and sign of the drive amplitudes, values of α in the range of $-\infty \le \alpha \le \infty$ may be selected.

In summary, Mach- Zehnder intensity modulators offer flexibility in controlling the chirp. With light equally split into both arms and operation in push-pull fashion, MZI intensity modulator can achieve zero chirp modulation. This, in fact, is the most attractive feature of the electro-optic modulators compared to electro-absorptive modulators for long haul transmission systems. Furthermore, MZI intensity modulators can provide either positive chirp or negative chirp as needed, depending on the split ratio or driving schemes. The flexibility of controlling the chirp is beneficial to the performance of optical fiber transmission systems. In the case of systems that must operate far from the zero-dispersion wavelength, low negative chirp is necessary to ensure low dispersion penalties.

CHAPTER 3

Theory and Design of Traveling Wave Electro-Optic Modulators

In this chapter, we discuss several issues key to the design of traveling wave electro-optic modulators. These issues include bandwidth limitation factors in traveling wave electro-optic modulators and the target specifications for designing a traveling wave electro-optic modulator. In addition, slow wave structures, closely related to the design of traveling wave electro-optic modulators on GaAs, are reviewed.

3.1 Bandwidth Limitation of Traveling Wave Modulators

3.1.1 Modulation Bandwidth

A key parameter of external electro-optic modulators is their modulation frequency response, which is often represented by the modulation bandwidth. The definition of the modulation frequency response for electro-optic modulators is closely related to how these modulators are used in systems. As shown in Figure 3.1, this typical optical communication link based on an external electro-optic modulator can define the

modulation frequency response and indicate one method to measure it. The link consists of a continuous wave (CW) optical laser source, an electro-optic modulator, and a square-law photodetector. The light from the optical source is coupled into the modulator, the electrical signal is applied to the electro-optic modulator, and then the modulated optical signal is transmitted onto the photodetector. In the photodetector, the modulated optical signal is converted to an electrical signal.

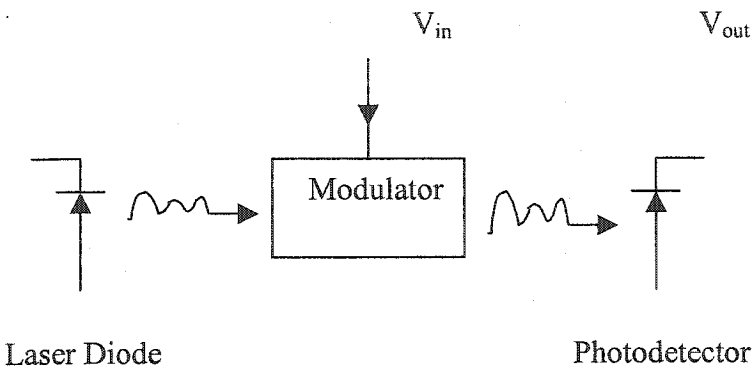

(a)

$$M(dBE)=20\log_{10}\left[\frac{V_{out}(f)}{V_{out}(f_0)}\right]$$

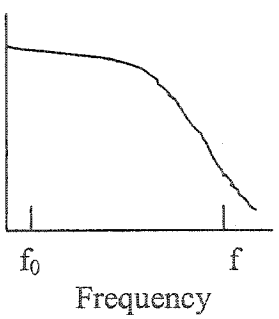

(b)

Figure 3.1 Modulation bandwidth of electro-optic modulators. (a) Typical measurement arrangement. (b) Schematic modulation response.

To define and measure the modulator's frequency response, the input signal is chosen to be a sinusoidal waveform, the frequency of which is denoted as f. Because all intensity modulators will demonstrate some degree of nonlinearity in their switching curves, the magnitude of the drive waveform is chosen to be small compared with the switching voltage. This linear approximation is valid and hence the modulation frequency response is uniquely specified (see theoretical analysis in section 2.3). In the small signal, or linear regime, the electrical signal produced by the photodetector will predominantly be a sinusoidal waveform at the same frequency as the modulator drive signal, f. If $V_{out}(f_0)$ represents the amplitude of the output of the detector at a reference f_0 (f_0 usually refers to low frequency or dc), then the magnitude of the modulation frequency response $M(f)$ expressed in electrical decibels (dBE) maybe defined as

$$\mathrm{M(dBE)} = 20\log_{10}\left[\frac{V_{out}(f)}{V_{out}(f_0)}\right] \tag{3.1}$$

Thus, $M(f)$ represents the relative efficiency of transferring RF power over the optical link. The modulation bandwidth f_{-3dBE} is defined as the frequency range over which the modulation response is greater than –3 dBE relative to the maximum response. In other words, the modulation bandwidth is defined by the frequency at which the output voltage decreases by $2^{-1/2}$ from its value at low frequency or dc. For clarity, this modulation bandwidth is called the electrical 3 dB bandwidth throughout the thesis. In some cases, the 3 dB bandwidth may be defined in terms of the frequency at which the optical modulation depth decreases to 50% of its maximum value. This corresponds to the frequency at which the received electrical RF power has fallen by 6 dBE, or the output voltage decreases by ½ from the value at low frequency or dc. This modulation bandwidth is quoted as the optical 3 dB bandwidth to differ from the electrical 3 dB bandwidth.

3.1.2 Conventional Modulators: Lumped Element Type

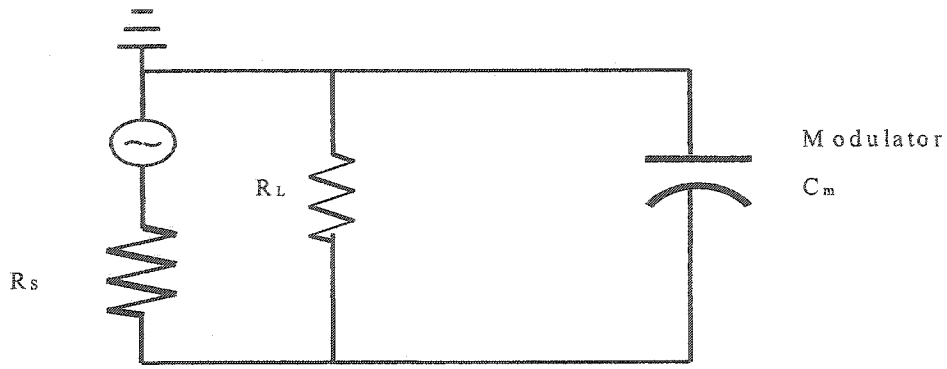

Figure 3.2 The simplified modulation circuit of lumped element modulators.

The lumped element modulators refer to those whose electrode length is small compared to RF wavelength. The lumped element modulators can be simply characterized by the equivalent circuit as illustrated in Figure 3.2. The modulator is modeled as a capacitance C_m, and a load resistor R_L matched to the source impedance R_S is placed in parallel with the capacitance of the modulator. The electrical 3 dB bandwidth based on equation (3.1) can be expressed as

$$f_{3dBe} = \frac{1}{2\pi(\frac{R_L R_s}{R_L + R_s})C_m} = \frac{1}{\pi R_L C_m} \tag{3.2}$$

where R_L is the load resistance, and R_L=R_S.

As the modulation frequency increases, the reciprocal of the frequency approaches the transit time over which the modulated light passes through the modulator. The modulating signal voltage begins to change before the modulated light has passed through the modulator, and the shape of the modulated output light is deformed by other voltage signals. The transit time for a lightwave, τ_m, is given by

$$\tau_m = n_r L / c_0 \tag{3.3}$$

where n_r and c_0 are the effective refractive index of the waveguide and the velocity of light in vacuum, respectively, and L is the interaction length (the interaction between the optical signal and the electrical signal). The electrical 3 dB bandwidth is therefore given by the following equation [43]

$$f_{3dBe/tr} \approx (1.4/\pi)/\tau_m = 1.4c_0/\pi n_r L \tag{3.4}$$

For example, the refractive index of GaAs waveguide at λ=1.55 μm is about 3.3737, and thus the calculated $f_{3dBe/tr}$ calculated for a modulator 500 μm long is about 79 GHz. The transit time of optical signal essentially determines the frequency response of modulators if they are used in the frequencies at around or more 100 GHz.

In summary, for lumped element modulators, the modulation bandwidth is limited by the RC time constant of the equivalent circuit and transit time.

3.1.3 Traveling Wave Modulators

One well-known method to overcome the RC time constant and transit time limitation occurring in lumped element modulators lies in applying the modulation signal in the form of a traveling wave. In a traveling wave design, the electrodes work as a transmission line; thus with distributed electrode capacitance, there is no RC time constant limitations to the modulator speed.

Consider the planar electrode formed on GaAs substrate surface as a transmission line. Figure 3.3 shows an equivalent circuit for the modulator.

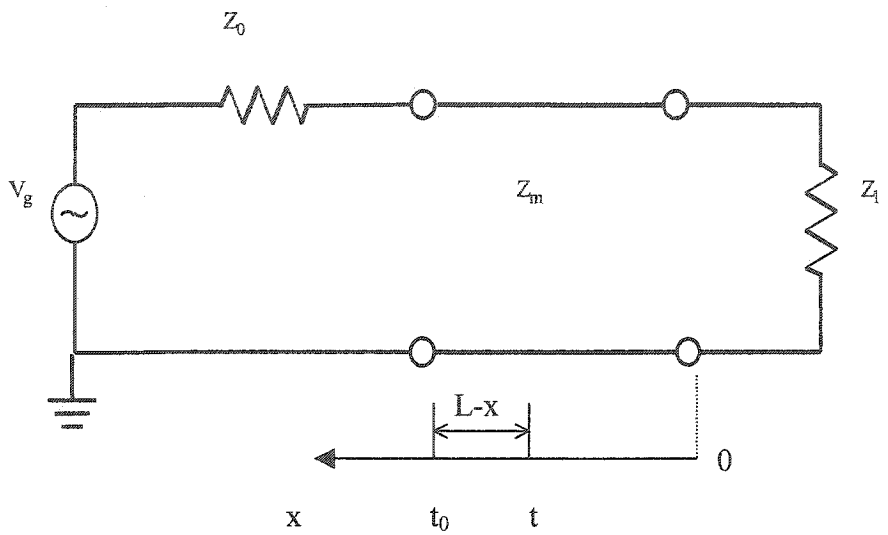

Figure 3.3 Traveling wave modulator equivalent circuit. Z_m is the characteristic impedance of the modulator. Z_l and Z_0 are the load and source impedance, respectively. L is the modulator electrode length (the length of the transmission line). V_g is the amplitude of the driving voltage.

According to the transmission line theory, the voltage at an arbitrary moment t at the position L-x (x is the distance from the shunted load resistor) can be expressed as:

$$V(x,\omega_m) = V_0^+ e^{i\beta_e x} + V_0^- e^{-i\beta_e x} = V_0^+ (e^{i\beta_e x} + \rho_2 e^{-i\beta_e x}) \tag{3.5}$$

with

$$\beta_e = \frac{\omega_m}{c_0} n_m - i\alpha_m \tag{3.6}$$

$$\rho_2 = \frac{Z_l - Z_m}{Z_l + Z_m} \tag{3.7}$$

where ω_m is the modulation frequency, α_m is the field attenuation constant, n_m is the microwave effective refractive index and c_0 is the speed of light in vacuum.

V_0^+ can be found from the voltage at the generator end of the line, where $x=L$:

$$V(L) = V_g \frac{Z_{in}}{Z_{in} + Z_0} = V_0^+ (e^{i\beta_e L} + \rho_2 e^{-i\beta_e L}) \tag{3.8}$$

With

$$Z_{in} = z_m (\frac{Z_l + iZ_m \tan \beta_e L}{Z_m + iZ_l \tan \beta_e L}) \tag{3.9}$$

so that

$$V_0^+ = V_g (\frac{Z_{in}}{Z_{in} + Z_0})(\frac{1}{e^{i\beta_e L} + \rho_2 e^{-i\beta_e L}}) \tag{3.10}$$

where V_g is the amplitude of driving voltage, and Z_{in} is the input impedance looking into the terminated transmission line from the generator end.

Equation (3.10) can be rewritten, using equations (3.7) and (3.9):

$$V_0^+ = V_g (\frac{Z_m}{Z_m + Z_0})(\frac{1}{e^{i\beta_e L} - \rho_1 \rho_2 e^{-i\beta_e L}}) = \frac{V_g}{2}(1 - \rho_1)(\frac{1}{e^{i\beta_e L} - \rho_1 \rho_2 e^{-i\beta_e L}}) \tag{3.11}$$

with

$$\rho_1 = \frac{Z_o - Z_m}{Z_o + Z_m} \tag{3.12}$$

With equation (3.11), equation (3.5) becomes

$$V(x, \omega_m) = \frac{V_g}{2}(1 - \rho_1)(\frac{1}{e^{i\beta_e L} - \rho_1 \rho_2 e^{-i\beta_e L}})(e^{i\beta_e x} + \rho_2 e^{-i\beta_e x}) \tag{3.13}$$

However, this is not the effective voltage contributing to the electro-optic modulation, for there is a phase walk-off between the optical signal and the microwave signal.

Consequently, the effective voltage seen at position L-x (0≤x≤L) by photons that enter the interaction region (x=L) at t_0 can be written as:

$$V_e(x,\omega_m) = \frac{V(x,\omega_m)}{e^{-i\beta_o(L-x)}} = V(x,\omega_m)e^{i\beta_o(L-x)}$$
$$= \frac{V_g}{2}(1-\rho_1)e^{i\beta_o L}\frac{(e^{i(\beta_e-\beta_o)x} + \rho_2 e^{-i(\beta_e+\beta_o)x})}{e^{i\beta_e L} - \rho_1\rho_2 e^{-i\beta_e L}} \tag{3.14}$$

where $\beta_o = \frac{\omega_m}{c} n_o$,and n_o is the optical effective refractive index.

According to the equation above, the average effective voltage along a length of L can be expressed as:

$$V_{ave}(\omega_m) = \frac{1}{L}\int_0^L V_e(x,\omega_m)dx$$
$$= \frac{V_g(1-\rho_1)e^{i\beta_o L}}{2(e^{i\beta_e L} - \rho_1\rho_2 e^{-i\beta_e L})}(V_+ + \rho_2 V_-) \tag{3.15}$$

where

$$V_+ = e^{j\phi_+}\cdot\frac{\sin\phi_+}{\phi_+}$$
$$V_- = e^{-j\phi_-}\cdot\frac{\sin\phi_-}{\phi_-}$$
$$\phi_+ = \frac{(\beta_e-\beta_o)L}{2} \tag{3.16}$$
$$\phi_- = \frac{(\beta_e+\beta_o)L}{2}$$

At the dc applied voltage, $V_{ave}(0)$ can be expressed with equations (3.7) and (3.12) as

$$V_{ave}(0) = V_g\left(\frac{Z_l}{Z_l+Z_0}\right) = \frac{V_g}{2}\frac{(1+\rho_2)(1-\rho_1)}{(1-\rho_1\rho_2)} \tag{3.17}$$

Based on the definition of modulation frequency response equation (3.1), the small-signal modulation frequency response of a traveling wave modulator can be obtained:

$$M(\omega_m) = \left| \frac{V_{ave}(\omega_m)}{V_{ave}(0)} \right|^2 = \left| \frac{(1-\rho_1\rho_2)}{(1+\rho_2)} \frac{(V_+ + \rho_2 V_-)}{(e^{i\beta_e L} - \rho_1\rho_2 e^{-i\beta_e L})} \right|^2 \tag{3.18}$$

In the case of a perfect impedance match, that is the characteristic impedance of the modulator is matched to both the driver and load impedance ($\rho_1 = 0$, $\rho_2 = 0$), equation (3.18) can be simplified as:

$$M(\omega_m) = e^{-\alpha_m L} \cdot \left| \frac{\sin\phi_+}{\phi_+} \right|^2 \tag{3.19}$$

In order to see clearly what factors influence the modulation frequency response, ξ is defined as an indicator of velocity mismatch between the modulating signal and the modulated signal:

$$\xi = (n_m - n_o)\frac{\omega_m}{c} \tag{3.20}$$

Thus ϕ_+ can be expressed in terms of velocity mismatch and microwave loss:

$$\phi_+ = \frac{(\beta_e - \beta_o)L}{2} = \frac{L}{2}(\xi - j\alpha_m) \tag{3.21}$$

With (3.20), and (3.21), equation (3.19) becomes:

$$M(\omega_m) = e^{-(\alpha_m L)} \left[\frac{\sinh^2(\frac{\alpha_m L}{2}) + \sin^2(\frac{\xi L}{2})}{(\frac{\alpha_m L}{2})^2 + (\frac{\xi L}{2})^2} \right] \tag{3.22}$$

The above equation describes the small –signal modulation frequency response of a traveling wave modulator with the characteristic impedance matched to both the driver and

load impedance. The modulation frequency response can be written in terms of f instead of ω_m, with $\omega_m=2\pi f$.

When velocity and impedance matching are both satisfied, equation (3.22) reduces to

$$M(f)=\frac{[1-e^{-\alpha_m L}]^2}{(\alpha_m L)^2} \tag{3.23}$$

According to this equation, 6.34 dB microwave loss determines the electrical 3dB bandwidth ($M(f)$=0.5), and 13.84 dB microwave loss determines the optical 3dB bandwidth($M(f)$=0.25). The loss requirement is greatly relaxed for the optical 3dB bandwidth.

On the other hand, if there is impedance matching and no microwave loss, then (3.22) becomes:

$$M(f)=\frac{\sin^2(\frac{\xi L}{2})}{(\frac{\xi L}{2})^2} \tag{3.24}$$

The electrical 3dB bandwidth derived from (3.24) is:

$$f_{3dBe}=\frac{1.4c}{\pi|n_m-n_o|L} \tag{3.25}$$

Correspondingly, the optical 3dB bandwidth based on (3.24) becomes

$$f_{3dBo}=\frac{2c}{\pi|n_m-n_o|L} \tag{3.26}$$

Velocity mismatch causes a phase walk off between the optical signal and the microwave signal, which reduces the modulation bandwidth. If the velocity of the microwave signal

closely matches that of the optical signal along the whole interaction length L, the 3 dB bandwidth (either electrical or optical) can be extremely large.

Equation (3.22) completely predicts the modulation bandwidth of a traveling wave modulator in terms of velocity mismatch and microwave loss in the case of perfect impedance matching.

Based on equation (3.22), a family of curves showing the effect of velocity mismatch and loss can be plotted. Figure 3.4 (a)-(e) demonstrates the modulation frequency response versus microwave frequency as a function of velocity mismatch ($|n_m - n_o|/n_m$) and loss (α_m). The characteristic impedance of the line is 50 Ω to match that of the source and of the load, the length of the electrode is normalized to 1 cm, and the microwave loss is assumed to be α_0 in $dB/(\sqrt{GHz}\cdot cm)$. These families of curves clearly demonstrate that microwave losses dominantly limit the electrical 3 dB bandwidth within 5% velocity mismatch while velocity mismatch begins to affect the bandwidth increasingly when it is beyond 15%. Thus for a large electrical 3 dB bandwidth (>40GHz), velocity mismatch needs to be kept within 5% and the microwave losses can reach up to 1 dB/ ($\sqrt{GHz}\cdot cm$) depending on velocity mismatch. Of course, these two numbers can be relaxed to some extent for the optical 3 dB bandwidth. In short, a low loss, velocity matched electrode is the key to wide bandwidth operation (both electrical and optical) of a traveling wave modulator in the case of perfect impedance matching.

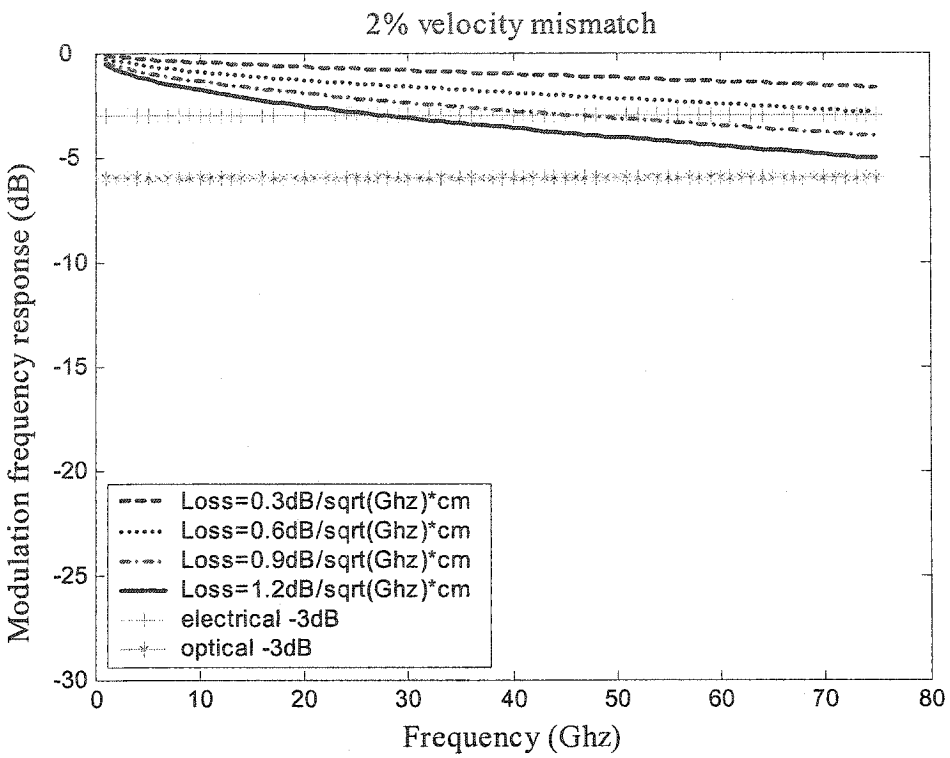
2% velocity mismatch
Modulation frequency response (dB)
Frequency (Ghz)
0
-5
-10
-15
-20
-25
-30
0
10
20
30
40
50
60
70
80
Loss=0.3dB/sqrt(Ghz)*cm
Loss=0.6dB/sqrt(Ghz)*cm
Loss=0.9dB/sqrt(Ghz)*cm
Loss=1.2dB/sqrt(Ghz)*cm
electrical -3dB
optical -3dB

(a)

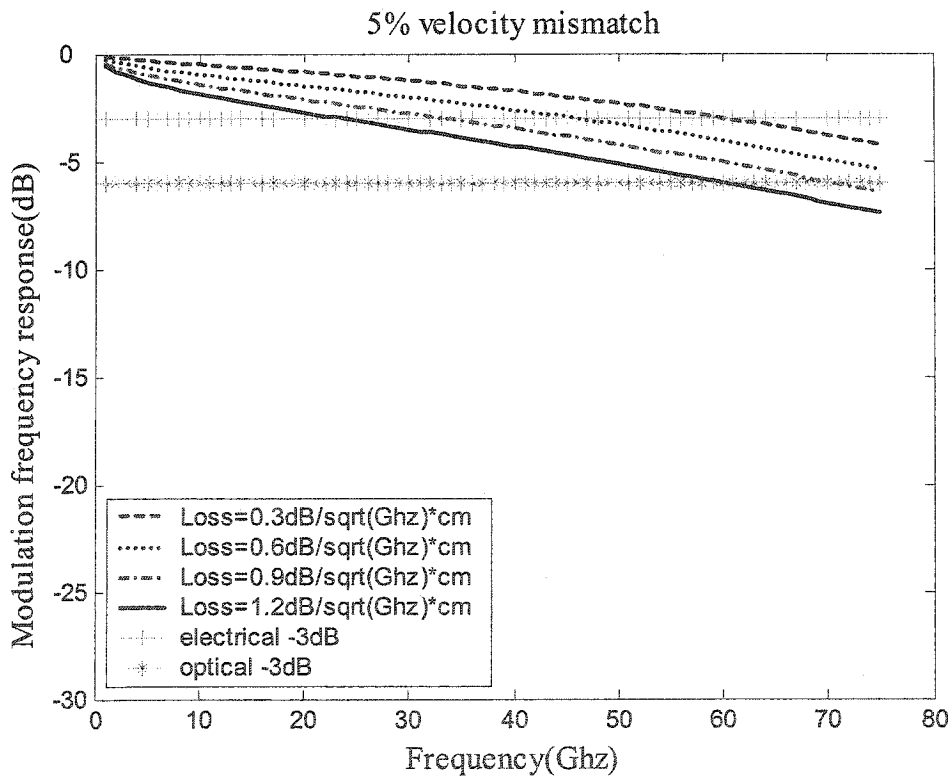
5% velocity mismatch
Modulation frequency response(dB)
Frequency(Ghz)
0
-5
-10
-15
-20
-25
-30
0
10
20
30
40
50
60
70
80
Loss=0.3dB/sqrt(Ghz)*cm
Loss=0.6dB/sqrt(Ghz)*cm
Loss=0.9dB/sqrt(Ghz)*cm
Loss=1.2dB/sqrt(Ghz)*cm
electrical -3dB
optical -3dB

(b)

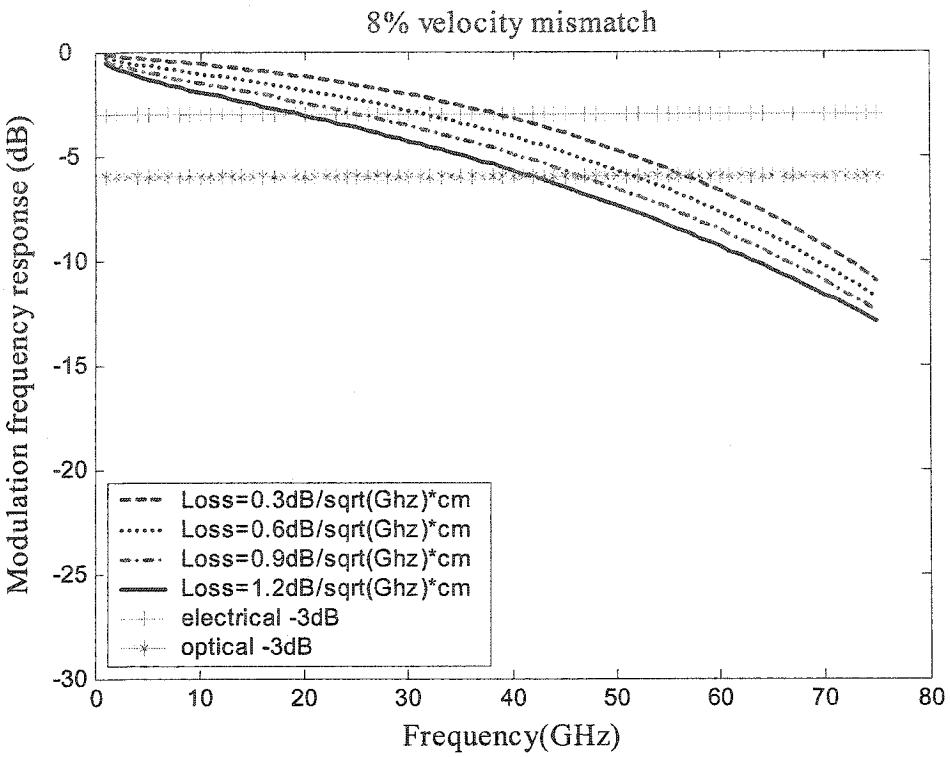
8% velocity mismatch
Modulation frequency response (dB)
Frequency(GHz)
Loss=0.3dB/sqrt(Ghz)*cm
Loss=0.6dB/sqrt(Ghz)*cm
Loss=0.9dB/sqrt(Ghz)*cm
Loss=1.2dB/sqrt(Ghz)*cm
electrical -3dB
optical -3dB

(c)

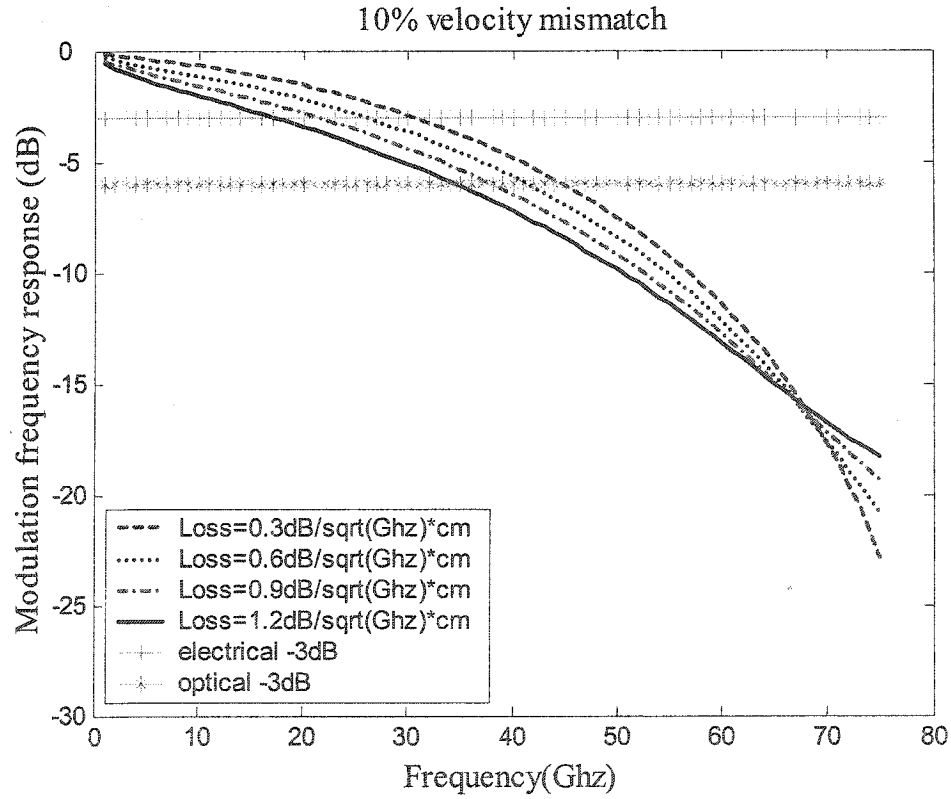
10% velocity mismatch
Modulation frequency response (dB)
Frequency(Ghz)
Loss=0.3dB/sqrt(Ghz)*cm
Loss=0.6dB/sqrt(Ghz)*cm
Loss=0.9dB/sqrt(Ghz)*cm
Loss=1.2dB/sqrt(Ghz)*cm
electrical -3dB
optical -3dB

(d)

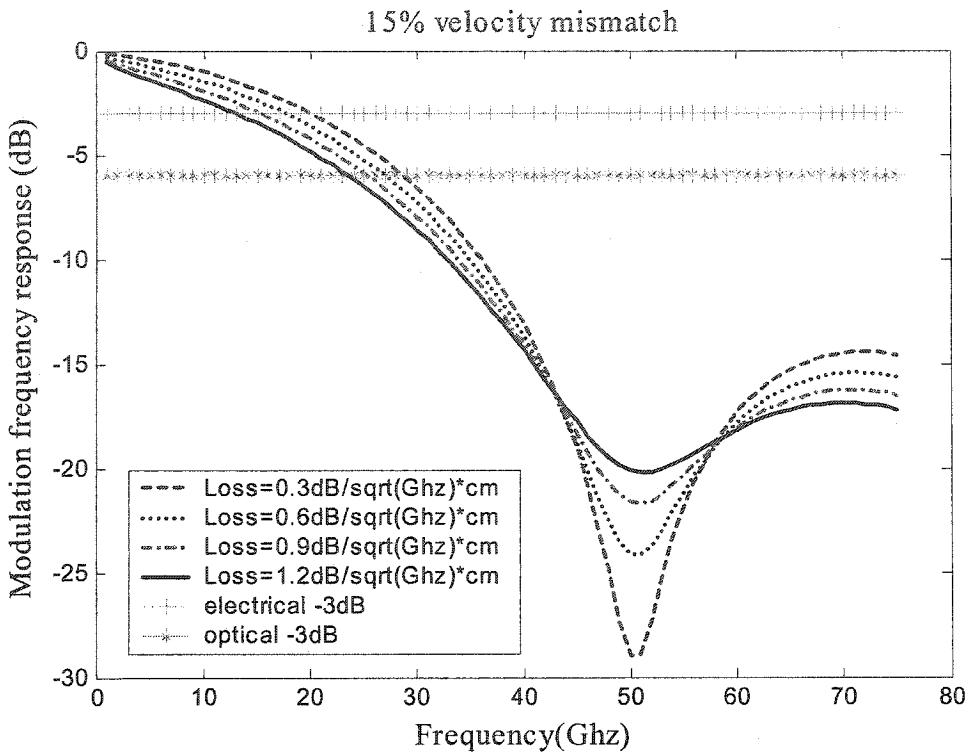

(e)

Figure 3.4 Modulation Frequency response versus microwave frequency for a traveling wave modulator with various percentages of velocity mismatch between the microwave signal and the optical signal (a) 2% velocity mismatch (b) 5% velocity mismatch (c) 8% velocity mismatch (d) 10% velocity mismatch (e) 15% velocity mismatch.

However, when there exist impedance mismatch, the modulation frequency response can be degraded. Equation (3.18) offers a comprehensive prediction of the modulation frequency response of a traveling wave modulator concerning all kinds of cases of impedance mismatch. Based on equation (3.18), the effect of impedance mismatch on modulation response can be evaluated. As demonstrated in Figure 3.5, the modulation frequency response is greatly reduced by the impedance mismatch while it achieves the best level when perfect impedance matching is satisfied, with the electrical 3dB bandwidth beyond 75 GHz. The impedance mismatch at the termination end (indicated by ρ_2)

degrades the modulation response more severely than the impedance mismatch at the generator end (indicated by ρ_1). Furthermore, the impedance mismatch causes ripples in the modulation response. The most notable of these effects is a sudden decrease in the modulation efficiency at low microwave frequencies. In addition, according to Equation (3.18), as far as the output is matched to the characteristic impedance of the modulator (ρ_2=0), the modulation frequency response does not decrease regardless of the impedance mismatch at the generator end.

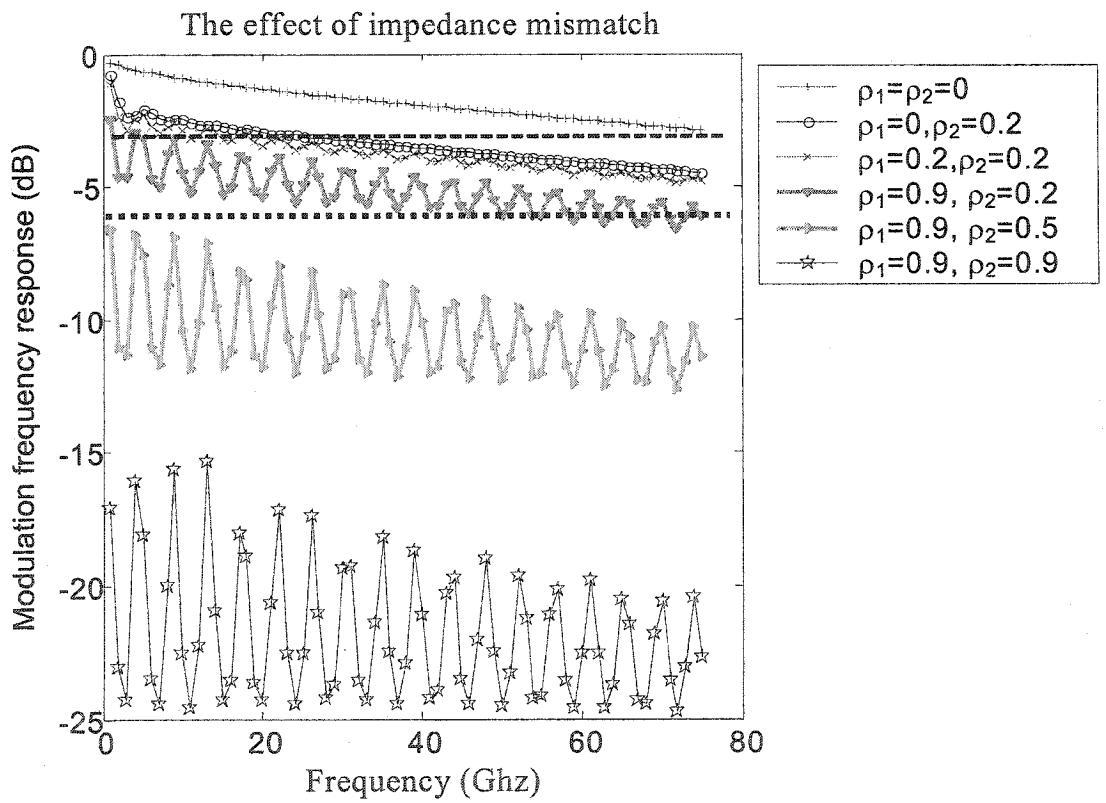

Figure 3.5 Modulation frequency response versus Frequency as a function of the reflection coefficient at the termination ρ_2, and of the reflection coefficient at the generator ρ_1. Assume n_o=3.3737, velocity mismatch $(n_m-n_o)/n_m$=2% and microwave loss=0.6 dB/$\sqrt{Ghz}\cdot cm$. The straight dashed line and the straight dotted line represent the electrical 3 dB and the optical 3 dB, respectively.

The reasons for these phenomena lie in that a standing –wave pattern will be generated on the electrode if the termination is different from the characteristic impedance of the modulator and this pattern will be frequency dependent, and hence the effective voltage on the electrode will change as a function of frequency. This, in turn, changes the modulation efficiency and creates ripples on the modulation response as a function of frequency. A standing wave consists of forward and backward propagating waves. The velocity mismatch for the counterpropagating (the backward counterpropagates the optical signal) interaction is severe because it depends on the sum, rather than the difference, of the optical and microwave indices. Consequently, the counterpropagating contribution to the modulation efficiency is strongly peaked at low frequency, thus the backward wave can be dominant factor determining the –3 dB electrical bandwidth, even for a small impedance mismatch.

The standing-wave effects can be eliminated by terminating the modulator electrode with a load having the same impedance as the characteristic impedance of the modulator electrode. Therefore, to ensure the flat and wide band modulation response, traveling wave modulators are designed to be matched to 50 Ω or to include a custom-matched termination. Though the impedance matching at the generator end is less critical from the modulation frequency response point view, microwave drive power requirement will be increased and some of the available power from the generator will be lost due to reflections originating from the impedance mismatch between the generator and electrode. Since almost all microwave sources have 50 Ω output impedance, it is imperative that the modulator electrode characteristic impedance is as closely matched to 50 Ω as possible.

3.1.4 Target Specification of Designing a Traveling Wave Electro-Optic Modulator

The efficiency of a traveling wave electro-optic modulator is often characterized by the figure of merit, rather than simply by the bandwidth itself. The figure of merit is defined as the ratio of bandwidth (f_{3dBe}) to the half wave voltage $V\pi$. Ideally, one should increase the bandwidth without increasing $V\pi$. Therefore, wide bandwidth and low half wave voltage is the target of designing a high speed traveling wave electro-optic modulator. As the above analysis demonstrated, wide bandwidth requires a velocity and impedance matched electrode with low microwave losses. Low $V\pi$ requires the electrode to generate a strong electric field overlapping very well with the optical mode in a certain direction dictated by the electro-optic material, and it also requires the material to possess a higher electro-optic coefficient. All these requirements are often conflicting and need to be traded off.

Similarly, the target of this research is to design a high speed traveling wave modulator with velocity matched and impedance matched (50 Ω characteristic impedance), and low microwave losses and a low half voltage. To achieve a low half wave voltage, a highly doped n^+ layer is utilized in the layer structures, providing high overlap integral (close to 1) of the optical mode and the electric field.

3.2 Slow Wave Structures

Several common microwave structures can be used to design a traveling wave electro-optic modulator, such as a microstrip line, a coplanar strip (CPS) and coplanar waveguide (CPW). As for dispersion, coplanar transmission lines are advantageous over microstrip lines for the phase and group velocity are almost the same in coplanar transmission lines. The dielectric constant of GaAs is about 13.2. The effective microwave index of a microstrip line on GaAs with zero conductor thickness and top dielectric as air is approximated by [48]:

$$n_m = \sqrt{\frac{\varepsilon_r + 1}{2} + \frac{\varepsilon_r - 1}{2} \cdot \frac{1}{\sqrt{1 + 12\frac{d}{w}}}} \tag{3.27}$$

where w is the width of the conductor and d is the thickness of the substrate, ε_r is the dielectric constant. For w$<d/2$, n_m is less than 2.89. Similarly, the effective microwave index of coplanar transmission lines such as CPS and CPW on GaAs with zero conductor thickness and a top dielectric as air is given by [49]:

$$n_m = \sqrt{\frac{\varepsilon_r + 1}{2}} \tag{3.28}$$

which is around 2.66. On the other hand, optical refractive index of GaAs at a wavelength of λ=1.55 μm is around 3.3737, thus the modulating microwave signal in the above structures travels faster than the modulated optical signal. In conclusion, for GaAs, and other III-V semiconductors, velocity matching requires slowing down the microwave signal. The most commonly used technique to slow a microwave signal is to use a slow wave transmission line.

3.2.1 Fundamentals of Slow Wave Structures

Slow wave propagation is related to particular electromagnetic modes of the structure of interest, and its fundamental characteristic parameters are slow wave factor and propagation loss. Maxwell's equations are required to describe accurately the guided wave properties of slow wave structures. The slow wave structures are usually assumed to be infinitely long for the study of guided wave properties. This assumption is very useful in practical designs of a finite but sufficiently long structure, and results from this assumption are completely accurate for a finitely long structure with impedance matching at both ends. In this case, slow wave propagation can be simply described by an equivalent transmission line model having the distributed elements denoted by RGLC. R and G are caused by conductor loss and dielectric loss in the material respectively. L, C are produced by the longitudinal current flow and transverse electric field.

In the frequency domain, the transmission line equations are:

$$\frac{dV(z)}{dz} = -(R + j\omega L)I(z) \tag{3.29a}$$

$$\frac{dI(z)}{dz} = -(G + j\omega C)V(z) \tag{3.29b}$$

This leads to uncoupled wave equations for the voltage and current on the line

$$\frac{d^2V(z)}{dz^2} = \gamma^2 V(z) \tag{3.30a}$$

$$\frac{d^2I(z)}{dz^2} = \gamma^2 I(z) \tag{3.30b}$$

where $\gamma = \alpha + j\beta = \sqrt{(R + j\omega L)(G + j\omega C)}$ is the complex propagation constant and the complex characteristic impedance of the line is given by

$$Z_o = Z_{or} + jZ_{oi} = \sqrt{(R + j\omega L)/(G + j\omega C)}\,. \tag{3.31}$$

The complex propagation constant γ can be rearranged as

$$\gamma = \sqrt{(j\omega L)(j\omega C)(1 + \frac{R}{j\omega L})(1 + \frac{G}{j\omega C})}$$

$$= j\omega\sqrt{LC}\sqrt{1 - j(\frac{R}{\omega L} + \frac{G}{\omega C}) - \frac{RG}{\omega^2 LC}} \tag{3.32}$$

In the high frequency range and low loss case such that $R << \omega L$ and $G << \omega C$, the above equation reduces to

$$\gamma = j\omega\sqrt{LC}\sqrt{1 - j(\frac{R}{\omega L} + \frac{G}{\omega C})} \tag{3.33}$$

The first two terms of the Taylor series expansion is used to give the first higher order real term for γ

$$\gamma \cong j\omega\sqrt{LC}\left[1 - \frac{j}{2}(\frac{R}{\omega L} + \frac{G}{\omega C})\right] \tag{3.34}$$

so that

$$\alpha \cong \frac{1}{2}(R\sqrt{\frac{C}{L}} + G\sqrt{\frac{L}{C}}) \tag{3.35a}$$

$$\beta \cong \omega\sqrt{LC} \tag{3.35b}$$

Similarly, the complex characteristic impedance can be approximated for low loss lines such that the real and imaginary parts are given by

$$Z_{or} \cong \sqrt{\frac{L}{C}} \tag{3.36a}$$

$$Z_{oi} \cong -\frac{1}{2\omega}\sqrt{\frac{L}{C}}\left(\frac{R}{L}-\frac{G}{C}\right) \tag{3.36b}$$

The phase velocity of a slow wave structure can be directly derived from above:

$$V_p \cong \frac{1}{\sqrt{LC}} \tag{3.37}$$

The above simple equation provides the basic requirements for a guided wave structure to generate slow wave propagation: either a large inductance or a large capacitance per unit length (or per period), or both, through the spatial separation of electric and magnetic energy.

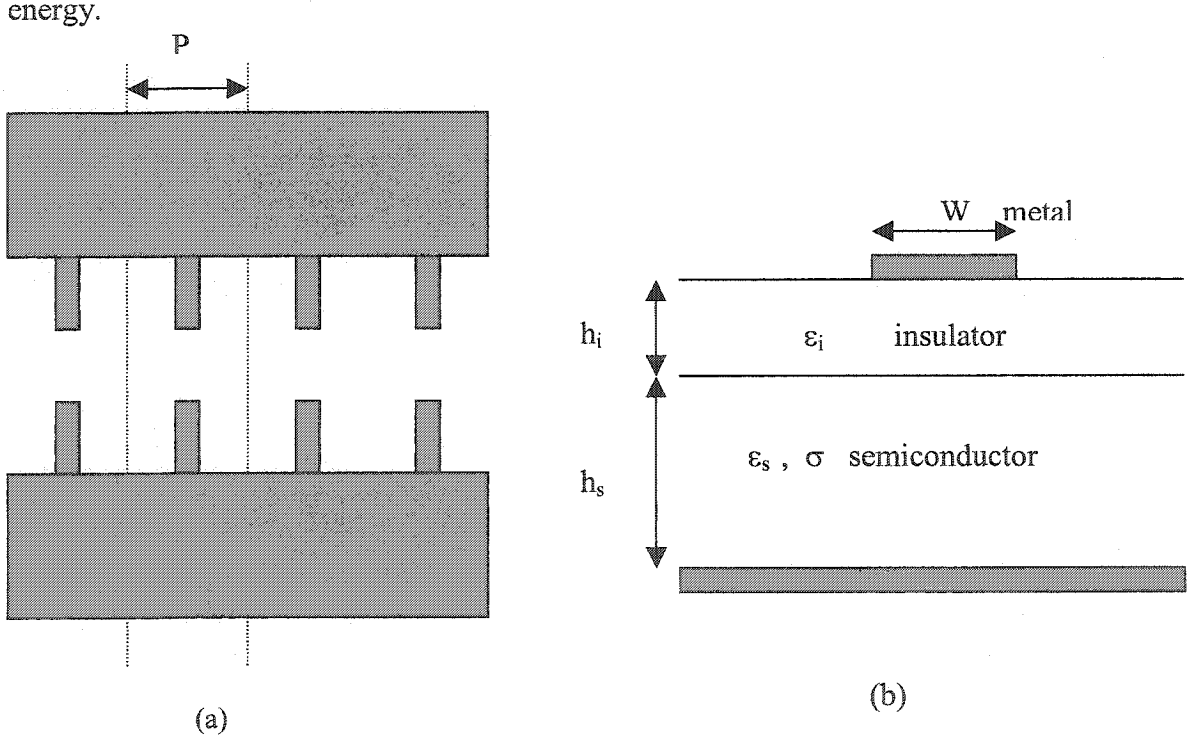

Figure 3.6 Two typical slow wave structures. (a) a periodic structure (b) metal insulator semiconductor structure (MIS).

There are two fundamental classes of slow wave structures: one is a periodic structure in the axial direction and the other is a uniform structure with special geometry designed in

the transverse direction. The most commonly found periodic structures are formed by periodic loading uniform structures with capacitive elements or inductive elements, as shown in Figure 3.6 (a). Slow wave propagation in periodic structures depends on the separate storage of electric and magnetic energy along the longitudinal direction. By periodic loading, a large capacitance or inductance is induced in periodic structures.

The uniform slow wave structures usually consist of multi-layered or composite materials with specially arranged thickness ratio and dielectric / magnetic properties. A typical example of this class of structure is a metal-insulator –semiconductor (MIS) transmission line, as shown in Figure 3.6 (b). In this case, planar transmission lines such as CPW or other planar patterns are fabricated on a doped thin or thick semiconductor substrate such as n+ Si or GaAs. Because the lossy semiconductor is always essential in the construction of a MIS structure, both conductance and resistance may be significant at high frequency. Therefore, loss may be higher in an MIS compared to the periodic structure. The storage of electric and magnetic energy is separated in the transverse direction for yielding slow wave propagation. The MIS structure generates only larger capacitance and basically unchanged inductance compared to its normal line counterpart.

3.2.2 Semiconductor loss

When a highly doped semiconductor layer is used in a slow wave structures, either MIS or periodic structures, microwave losses due to the high carrier density of the doped layer cannot be neglected. The conductivity of this doped layer,σ_0 is given by:

$$\sigma_0 = qu_n n + qu_p p \tag{3.38}$$

where n and p are the free electron and hole carrier concentrations respectively, u_n and u_p are the electron and hole mobilities respectively, and q is the electron charge. For n+ doped material, p<<n, equation (3.38) can be simplified to:

$$\sigma_0 = qu_n n \tag{3.39}$$

For GaAs, u_n can be given by [50]

$$u_n = \frac{7200}{[1+(5.51\times10^{-17})N_d]^{0.233}} \tag{3.40}$$

where N_d is the donor doping density (is equivalent to n) in cm^{-3} and u_n is in $cm^2/V\text{-}s$.

With equations (3.39) and (3.40), semiconductor losses can be estimated.

3.3 Summary

This chapter has reviewed some fundamental issues to traveling wave modulators, and slow wave structures applicable to III-V semiconductor modulators for velocity matching. This review suggests some design criteria for III-V traveling wave electro-optic modulators.

(1) The electro-optic overlap integral should be as large as possible to increase modulation efficiency. This leads to p-i-n structures over purely coplanar geometries.

(2) The microwave loss should be minimized. Conductors of low resistance need to be used.

(3) Slow wave structures should be used to slow down the speed of the microwave signal in order to match that of the optical signal.

(4) The characteristic impedance should be adjusted, if possible, 50 Ω for impedance matching of the load, generator and modulator.

(5) Microwave design and optical design should be decoupled as far as possible to allow independent optimization.

The next two chapters will focus on designing and modeling GaAs traveling wave modulators based on above design considerations.

CHAPTER 4

Design and Modeling of GaAs Traveling Wave Electro-Optic Modulators Based on Planar Microstrip Structure

A variant on the MIS slow wave structure, called Planar Microstrip Structure (PMS), has been studied in the design of traveling wave modulators with an optical 3 dB bandwidth of over 40 GHz and a half wave voltage less than 6 V predicted [34]. This structure combines the p-i-n and coplanar features to achieve wide-band velocity match. In this chapter, we will investigate the potential of PMS being used as the electrode of high-speed GaAs traveling wave electro-optic modulators. This will cover the design of heterostructure optical layers, and of PMS slow wave electrodes. This study goes beyond that of [34] in several respects. A full structure is simulated instead of planar approximation and lossy metal is used in the design and simulation instead of lossless metal. Furthermore, a modulator with impedance and velocity matched is designed and optimized. More importantly, the design space of the PMS electrodes is characterized so that it provides guidance for the future design and optimization of GaAs traveling wave electro-optic modulators with PMS electrodes.

4.1 Planar Microstrip Traveling Wave Electro-Optic Modulators

A microwave transmission line with low loss and velocity matched to a lightwave for III-V traveling wave electro-optic modulator has been analyzed using the spectral domain technique [34]. This structure, as shown in Figure 4.1, has the ground plane on the top of the

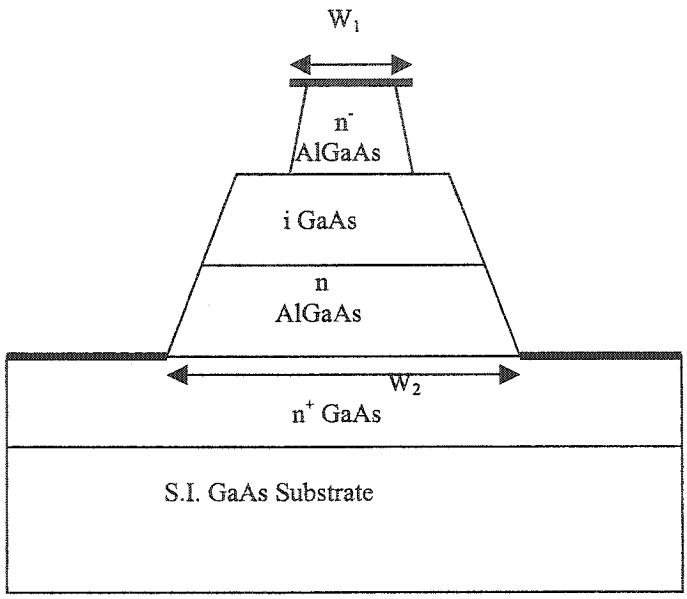

Figure 4.1 Cross sectional view of a new planar microstrip configuration modulator on a semi-insulating (100) GaAs substrate with double heterostrucutre cladding layers of n- and n. The bottom electrode of the conventional p-i-n structure is placed on the top of n+ epitaxial layer. The top signal strip width is W_1, and the slot width of the ground strips is W_2. (Fig. 2 of [34])

n+ epitaxial layer. Epitaxial layers of n^+ GaAs, n AlGaAs buffer, i GaAs guiding, and n^- AlGaAs buffer layers are grown on a semi-insulating (SI) GaAs substrate. Microwave losses are reduced due to the fact that a thin n^+ layer and a SI GaAs substrate are used instead of a n^+ GaAs substrate. The doped n^+ epitaxial layer contributes to velocity matching and ensures the excellent overlap of the optical mode and the microwave field.

The dimensions and conductivities are as follows: 250 μm thick GaAs semi-insulating substrate with $\sigma=1\times10^{-6}$ moho/m; 2 μm thick n^+ GaAs layer with $\sigma=5\times10^{4}$ mho/m; 2.7 μm thick n $Al_{0.03}Ga_{0.97}As$ layer with $\sigma=5.88\times10^{3}$ mho/m; 3.3 μm thick undoped GaAs guiding layer fully depleted with $\sigma=0$; 2.7 μm thick n^- $Al_{0.03}Ga_{0.97}As$ layer on the top which is easily depleted with $\sigma=0$. The width of the top electrode W_1 is 8 μm and the slot width W_2 is 24 μm [34].

A single optical mode is guided in the i-layer. The top n^- epitaxial layer and undoped i layer are easily depleted by the Schottky contact. Intensity modulation of the light is achieved by launching the light with a polarizer along the direction of $(1/\sqrt{2})(\hat{z}'+\hat{y}')$ at the input of the waveguide, and orienting an analyzer in the direction of $(1/\sqrt{2})(\hat{z}'-\hat{y}')$ at the output of the waveguide, where $\hat{z}'$ and $\hat{y}'$ are the [001] and $[\bar{1}10]$ optical axes of GaAs, respectively (see Figure 2.3 and Figure 2.8, for the wafer orientation is (001)). The modulator based on this architecture can only modulate the TE optical mode due to the direction of the applied electric field, which is predominantly vertical.

4.1.1 Slow Wave Propagation of Planar Microstrip Structure

As mentioned before, for traveling wave electro-optic modulators on III-V semiconductor materials, slow wave electrodes need to be used for velocity matching and one kind of slow wave electrodes is the MIS structure. For PMS, with the top metal on the n^- epitaxial

layer, a Schottky contact is formed so that the n^- epitaxial layer and the undoped i layer are easily depleted. The PMS can be regarded as a special MIS structure. In a PMS line, a depletion region is formed by a reverse voltage bias over the top strip with respect to the ground plane and such a depletion region is equivalent to the insulator of a MIS structure.

It is indicated that there exists three different modes of propagation along a MIS structure as the frequency varies [36][51]. They are called the slow wave mode, the dielectric quasi-TEM mode, and the skin effect mode, respectively. In general, they can be distinguished with three characteristic frequencies, the dielectric relaxation frequency f_d, the characteristic frequency of the skin effect f_s, and the relaxation frequency of interfacial polarization f_p. f_d, f_s and f_p are expressed, respectively by:

$$f_d = \frac{1}{2\pi}\frac{\sigma}{\varepsilon_s} \tag{4.1}$$

$$f_p = \frac{1}{2\pi}\frac{\sigma}{\varepsilon_i}\frac{h_i}{h_s} \tag{4.2}$$

$$f_s = \frac{1}{2\pi}\frac{2}{\mu_0 \sigma h_s^2} \tag{4.3}$$

where μ_0 is the permeability of free space, ε_i and ε_s are the permittivity of the insulator and of the semiconductor, respectively, σ is the conductivity of the semiconductor, h_i is the thickness of the insulator layer while h_s is the thickness of the semiconductor layer (see Figure 3.6 (b)). And the skin effect depth of the semiconductor δ_s is given by:

$$\delta_s = \sqrt{\frac{2}{\omega \mu_0 \sigma}} \tag{4.4}$$

The dielectric quasi-TEM mode exists in the region where $f_d < f$. In this region, $\omega\varepsilon_s >> \sigma$ is satisfied so that the doped semiconductor behaves like a normal dielectric and confines most of the guided wave energy in it. This propagation is usually lossy.

The skin effect mode propagates when $f_s < f < f_d$ is satisfied. In this region, the doped semiconductor layer acts as a lossy conductor wall to the wave since $\omega\varepsilon_s << \sigma$. The microwave field only penetrates into the semiconductor up to the skin depth δ_s and does not penetrate further; therefore the dispersion behavior is governed by the skin effect in the semiconductor. That's why this mode is called skin effect mode.

The slow wave mode occurs in the region with $f \ll f_d$ *and* $f \ll f_s$. When the frequency f is not so high and conductivity of the semiconductor is moderate, the electric field is confined within the insulator while the magnetic field penetrates freely over the cross-section. Consequently, the energy separation in space occurs and slow wave mode propagates.

For the PMS modulator, the operating frequency is much lower than the dielectric relaxation frequency f_d ($f_d = \frac{1}{2\pi}\frac{\sigma}{\varepsilon_s} \cong 68192$ GHz with $\sigma=5\times10^4$ mho/m for the n^+ doped GaAs), so the dielectric quasi-TEM mode does not propagate. The thickness of the n^+ layer 2 μm is smaller than the skin depth up to 500GHz ($\delta_s = \sqrt{\frac{2}{\omega\mu_0\sigma}} \cong 3.185$ μm for 500 GHz), so the skin effect mode does not propagate either under 500 GHz. Thus only slow wave mode exists in PMS for operating frequency below 100 GHz.

4.1.2 Validation of Modeling

In order to examine the validity of modeling, simulating the original PMS structure as shown in Figure 4.1 (Fig.2 (a) in [34]) is necessary. The spectral domain analysis (SDA) was used in [34] to investigate the microwave propagation characteristics: dispersion and loss. However, there are two drawbacks to this technique:1) ridge or strip-loaded structures are approximated by planar structures and 2) electrodes are assumed to be perfect conductors with zero thickness. The planar approximation (Fig.2 (b) in [34]) does not overestimate the microwave loss due to the fact that the ridges of the n^- and i layers are completely depleted of carriers at the operating bias voltage. However, the planar approximation does overestimate the fringing capacitance of the structure, resulting in a slightly larger value of the microwave index n_u. The assumption that electrodes are lossless metal with zero thickness may lead to two problems: a) only dielectric loss can be calculated from SDA, b) the effect of lossy metal with finite thickness on dispersion (microwave index) cannot be detected. The dispersion and dielectric loss calculated from the SDA for the PMS modulator is shown in Fig.7 of [34]. The microwave index n_u is 3.58 up to frequencies > 60 GHz, and the dielectric loss is around 0.9 dB/mm at 55 GHz.

In this research, the modeling and design of microwave structures has been accomplished by using a commercially available CAD package, the Sonnet Suites, based on a modified Method of Moments [52]. *Em* of the Sonnet Suites performs a complete electromagnetic analysis for arbitrary 3-D geometry at any frequency. The analysis inherently includes dispersion, stray coupling, discontinuities, surface waves, moding, metalization loss, dielectric loss and radiation loss. *Emvu* of the Sonnet Suites can be used to view results

from an *Em* analysis as a color shaded plot. The colors can represent either the magnitude of current density or charge. The view of current density or charge density at a different frequency is particularly useful for the analysis of periodic structure such as the CPS loaded structure studied in the next chapter, for current density distribution can be used to explain why the CPS loaded line is essentially a low loss microwave structure and charge density distribution can show where a strong electric field is produced.

On the other hand, there are some limitations of using this tool. First, the vertical electric field cannot be viewed, though the tangential electric field can be sensed. Next, when thick metal are used as the electrodes, more complex geometry are used to set up the structure and more memory are needed for the simulation.

As for the design of PMS electrodes and for the design of CPS loaded structures, dielectric bricks and reference planes have to be used in the simulation. The reasons lie in the fact that a highly doped n^+ layer is used in the layer structure, and if such a highly doped layer directly contacts the ports, it will short out the ports. To overcome this difficulty, reference planes have to be used to make the studied structure far away from the ports. The highly doped layer has to be defined as dielectric brick. The use of reference planes will not affect the accuracy of results since the s parameter of the studied structure are dembedded from the analysis. The use of dielectric bricks may slow down the simulation since it needs more memory, but it won't affect the accuracy of results either.

This simulator offers S-parameters at a specific frequency for a given structure. Transmission line parameters such as characteristic impedance, phase velocity, and microwave loss can be extracted from S-parameters as discussed below.

The ABCD matrix of the entire transmission line is expressed as a function of the S-parameters as follows [53]:

$$\begin{bmatrix} A & B \\ C & D \end{bmatrix} = \begin{bmatrix} \dfrac{(1+s_{11})(1-s_{22})+s_{12}s_{21}}{2s_{21}} & Z_{0r}\dfrac{(1+s_{11})(1+s_{22})-s_{12}s_{21}}{2s_{21}} \\ \dfrac{1}{Z_{0r}}\dfrac{(1-s_{11})(1-s_{22})-s_{12}s_{21}}{2s_{21}} & \dfrac{(1-s_{11})(1+s_{22})+s_{12}s_{21}}{2s_{21}} \end{bmatrix} \tag{4.5}$$

Where Z_{0r} is the reference characteristic impedance of the measuring system, 50Ω. The characteristic impedance, Z_0, the propagation constant γ of the line can be found:

$$Z_0 = \frac{2B}{D - A \pm \sqrt{(A+D)^2 - 4}} \tag{4.6}$$

$$\gamma = \frac{1}{l}\left[\ln\left(\left(\frac{A+D}{2}\right) \pm \sqrt{\left(\frac{A+D}{2}\right)^2 - 1)}\right)\right] \tag{4.7}$$

Here, l is the length of the transmission line. The propagation constant γ may be decomposed as $\gamma = \alpha + j\beta$, where α is the attenuation coefficient (Np/unit length) and β is the phase constant (rad/unit length). Equations 4.6 and 4.7 produce double values for both Z_0 and γ. The physically meaningful value of Z_0 is positive. The physically meaningful value of γ has a positive α. The phase velocity v_p is found as:

$$v_p = \frac{2\pi f}{\beta} \tag{4.8}$$

The simulation results will be presented below.

First, lossless metal with zero thickness is used in the simulation, in order to compare the modeling results with those from the SDA [34]. The original structure shown in Figure 4.1 is an input structure. The dispersion and the dielectric loss obtained are illustrated in Figure 4.2. The microwave index n_u does not change very much with the frequency. It is about 3.36 at 1 GHz and decreases to 3.33 at 55 GHz. The microwave index calculated from this model is slightly smaller than that from SDA. The reason for this discrepancy is that the full structure is used in the simulation rather than the planar approximation used in SDA, so this result is close to the actual value. The dielectric loss is also around 0.9 dB/mm at 55 GHz, very close to the data shown in Fig.7 of [34].

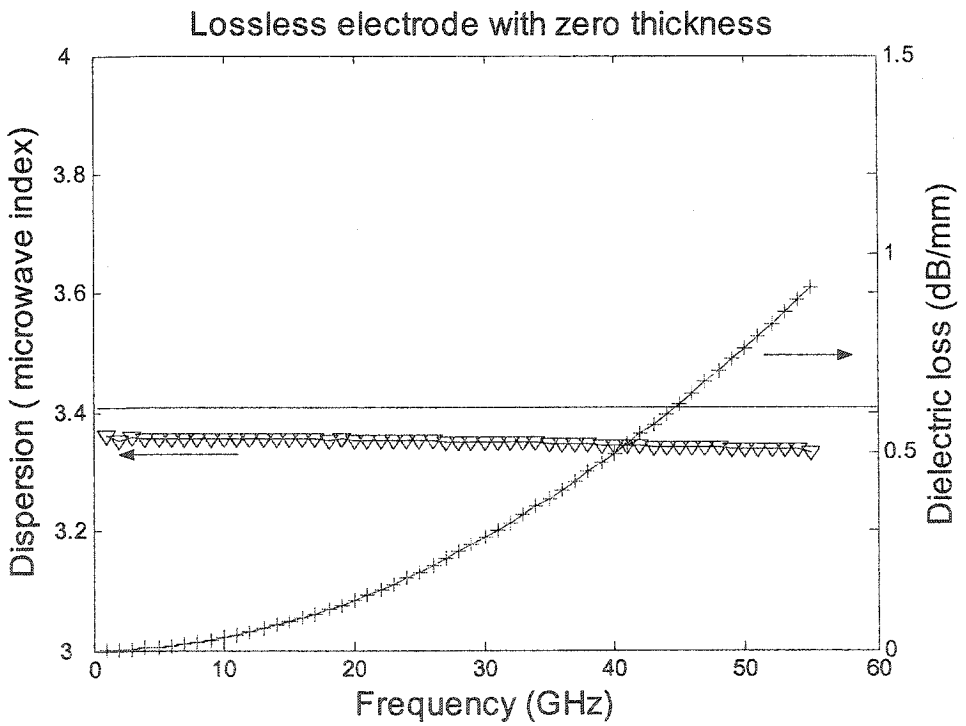

Figure 4.2 Dispersion and dielectric loss calculated from our model for the PMS modulator in Figure 4.1 (Fig. 2 in [34]). The straight line represents the optical index of 3.41 at λ=1.3 μm for GaAs. The electrodes are assumed to be perfect conductors with zero thickness.

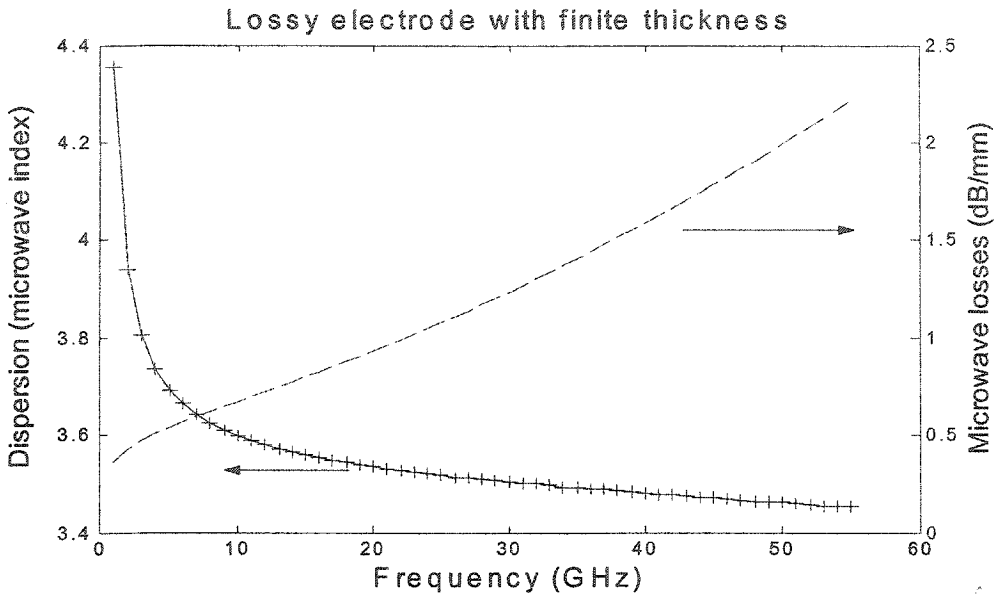

Figure 4.3 Dispersion and dielectric loss calculated from the Sonnet model for the PMS modulator in Figure 4.1 (Fig. 2 in [34]) with lossy metal as electrodes. The electrode here used is 1 μm thick Au.

Second, the effect of a lossy metal with finite thickness on the dispersion of the PMS structure is investigated. Here, 1 μm thick Au is used as electrodes of the structure. As shown in Figure 4.3, the PMS structure becomes quite dispersive under 6 GHz and less dispersive above 6 GHz and microwave losses (dielectric loss plus electrode loss) goes up to 2.2 dB/mm at 55 GHz. Based on Figure 4.2 and Figure 4.3, it can be concluded that lossy metal with finite thickness causes the PMS structure more dispersive at lower frequency than its counterpart, lossless metal with zero thickness does, and that the electrode loss in PMS exceeds the empirical electrode loss of 1 dB/($\sqrt{GHz}$·cm) used in [34]. 1 μm thick electrode causes the structure more dispersive at low frequency because

the skin effect depth is more than 1 μm below 6 GHz so that the electric field fully penetrates 1 μm thick electrode at low frequencies under 6 GHz.

Assuming that impedance matching is satisfied at both the generator end and the load, the modulation frequency response of the PMS modulator with the lossy electrodes of finite thickness, can be estimated with equation (3.22), as shown in Figure 4.4. The electrical 3 dB bandwidth can reach 9 GHz while the optical 3 dB bandwidth can extend to 33 GHz. The optical 3 dB bandwidth predicted by our model is less than 42 GHz, the optical 3dB bandwidth predicated by SDA [34], for the electrode loss is underestimated by using the empirical electrode loss in the latter case.

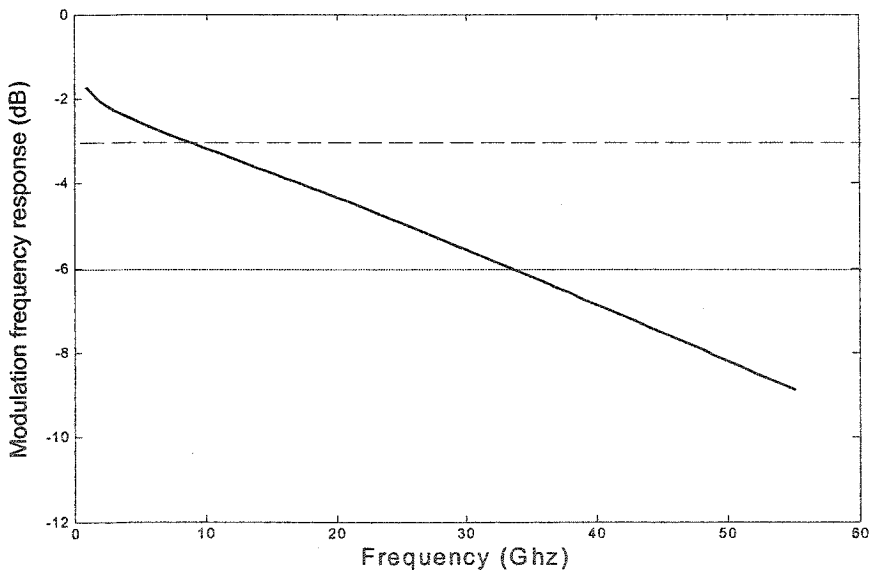

Figure 4.4 The modulation frequency response of the PMS modulator shown in Figure 4.1. 1μm thick Au is used as the electrode. The black dashed line represents the electrical 3 dB, and the black solid line represents the optical 3 dB.

In summary, the Sonnet model of the PMS structure is not only valid, but also provides a more comprehensive and accurate electromagnetic analysis of the PMS structure than the SDA model does, for the Sonnet model uses the real 3D structure rather than the planar approximation, and takes lossy metal with finite thickness into account.

4.2 Optical Structures

4.2.1 Optical Insertion Loss

Generally speaking, there are two types of optical integrated circuits: the hybrid and monolithic types. Though hybrid optical integrated circuits have lots of advantages, the monolithic type represents the ultimate development trend. Therefore, the development of optical waveguides on semiconductor materials with low insertion loss is imperative to the success of monolithic integration of optical circuits. The optical insertion loss is composed of coupling loss due to mode mismatch and misalignment, Fresnel reflection loss due to material index discontinuities, and propagation loss due to scattering, material absorption, free carrier absorption, and electrode loading due to its proximity.

Coupling loss problems usually arise when the optical integrated devices join with single mode optical fibers, for the electromagnetic fields of their modes do not match each other very well. In order to reduce the coupling losses, it is essential to match the electromagnetic fields of the propagation modes in the optical waveguide and optical fiber

as closely as possible. The field distribution of the fundamental mode in a single mode waveguide can be approximated by a Gaussian profile even for ridge waveguide structure [54]. The transverse electric field in the single mode fiber can be expressed by:

$$E_f = (2/\sqrt{\pi}r)\exp[-(x^2+y^2)/2r^2] \tag{4.9}$$

where r is the 1/e field radius and 2r is referred to as the mode spot size of the fiber. The electric field in the ridge waveguide can also be expressed by

$$E_g = 2/\sqrt{w_x w_y}\,\exp(-x^2/2w_x^2 - y^2/2w_y^2) \tag{4.10}$$

where $2w_x$ and $2w_y$ are mode spot size of the waveguide in the lateral and vertical direction, respectively (mode spot size is defined by full width half-maximum of the waveguide mode).

The coupling efficiency between a single mode fiber and a single mode ridge waveguide is given by the overlap integral of the spatial field distributions of the two optical fields

$$P = \frac{\left|\iint E_f E_g\, dxdy\right|^2}{\iint |E_f|^2\, dxdy \iint |E_g|^2\, dxdy} \tag{4.11}$$

With the help of equations (4.9) and (4.10), equation (4.11) can be simplified to

$$P = \frac{4}{(\frac{w_x}{r}+\frac{r}{w_x})(\frac{w_y}{r}+\frac{r}{w_y})} \tag{4.12}$$

and the coupling loss (in dB) is given by

$$C_l = 10 * \log_{10} P \tag{4.13}$$

Theoretical calculations for the coupling efficiency can be achieved analytically using (4.12). Typical results are shown in Figure 4.5.

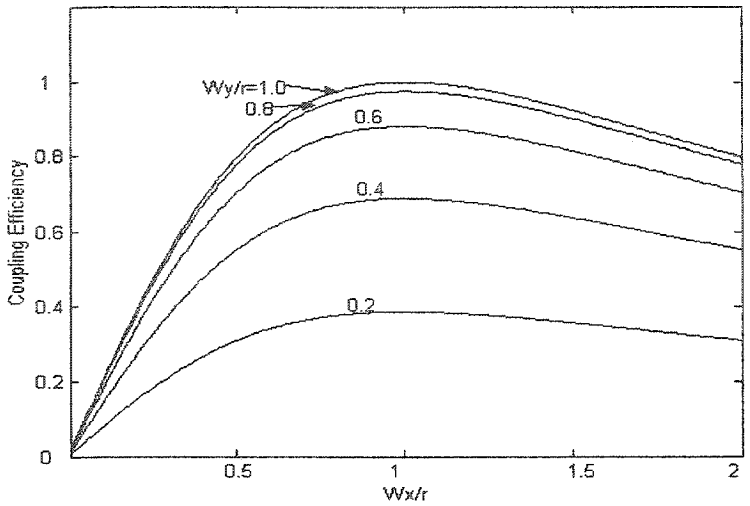

Figure 4.5 Coupling efficiency as a function of mode radii, w_x and w_y are the spot radii of the waveguide in the lateral and vertical directions respectively, and r is the mode radius of the fiber.

Figure 4.5 indicates that the coupling efficiency or coupling loss strongly depends on the mode mismatch through r, w_x and w_y , and that the field distribution of the ridge waveguide should be as circular as possible and similar to the field distribution of the optical fiber. In short, when $w_x = w_y = r$ is satisfied, there is no coupling loss.

The reduction of coupling loss suggests that the optical waveguide designed should be capable of coupling efficiently to a single mode fiber having a 9 μm core diameter. On the other hand, the hybrid or monolithic integration of traveling wave modulators with lasers requires that the mode size of these optical modulators should match that of laser sources to reduce coupling losses. Of course, either lensed optical fibers or micro-lenses can be used to increase the coupling efficiency between the optical fiber and optical waveguides

when the small optical wavguide does not match the optical fiber. Optical mode spot size transformation is another alternative for the reduction of coupling loss.

Alignment is another key to the reduction of coupling loss. With accurate alignment, optimum coupling can be achieved. Misalignment will inevitably cause the coupling loss between the single mode waveguide and the single mode fiber even if their mode sizes are perfectly matched. In fact, the estimation of coupling loss with Equation (4.12) is based on the assumption that alignment is kept.

Fresnel reflection loss can be easily reduced using antireflection coatings such as silicon monoxide or cerium oxide films.

Propagation losses of optical waveguides generally are attributable to three mechanisms: scattering, absorption and radiation. Scattering loss often predominates in glass or dielectric waveguides while material absorption is often the most important in semiconductors and other crystalline materials. Radiation losses can become significant when waveguides are bent through a curve. Reduction in propagation loss can result from improvements in the substrate quality and epitaxial growth techniques as well as waveguide design. Measures also need to be taken to eliminate free carrier absorption when semiconductor waveguides are designed with highly doped materials used. The waveguide design becomes crucial to the reduction of propagation loss when there exists a highly doped n^+ or p^+ layer in the waveguide.

An expression for the absorption coefficient α_{fc} due to free carrier absorption derived from classical electromagnetic theory, is given by [55]:

$$\alpha_{fc} = \frac{Nq^3 \lambda_0^2}{4\pi n (m^*)^2 \mu \varepsilon_0 c^3} \tag{4.14}$$

N is the free carrier concentration per cm^3 and n is the index of refraction, m^* is the effective mass of the carriers, λ_0 is the free space wavelength of operation, μ is the mobility of carriers, c, q and ε_0 have their used meaning. According to this expression, free carrier absorption in heavily doped ($N > 10^{18}$) GaAs can be expected to produce losses of the order of 1-10 cm^{-1}. The major loss due to free carrier absorption occurs in the evanescent tail of optical modes propagating in heavily doped substrates or confining layers. However, by taking proper measures in the waveguide design, one can minimize these losses.

4.2.2 The Design of Single Mode Optical Waveguides

There are some considerations concerning the design of single mode waveguide. The single mode propagation of the optical signal with large waveguide dimensions usually demands a very small difference in refractive indices between the core and the clad region, and this can be realized by changing the material composition in the clad and core layers.

In our design, $Al_xGa_{1-x}As$ with a small mole fraction of Al is used as the cladding material and GaAs is used as the core material, for $Al_xGa_{1-x}As$ is lattice-matched to GaAs for the

full range of composition from GaAs to AlAs. The refractive index of GaAs and $Al_xGa_{1-x}As$ can be determined from Sellmeier equation [55]:

$$n^2 = A(x) + \frac{B}{\lambda_0{}^2 - C(x)} - D(x)\lambda_0^2 \tag{4.15}$$

where x is the atomic fraction of Al atoms in the $Al_xGa_{1-x}As$, λ_0 is the free space wavelength of operation, and A, B, C, D are the functions of x given in Table 4.1. Here λ_0 is 1.55 μm.

Table 4.1 Sellmeier equation coefficient (for λ_0 in μm)

Material	A	B	C	D
GaAs	10.906	0.97501	0.27969	0.002467
$Al_xGa_{1-x}As$	10.906-2.92x	0.97501	$(0.52886-0.735x)^2$ $x \leq 0.36$ $(0.30386-0.105x)^2$ $x \geq 0.36$	$[(0.002467)\cdot(1.41x+1)]$

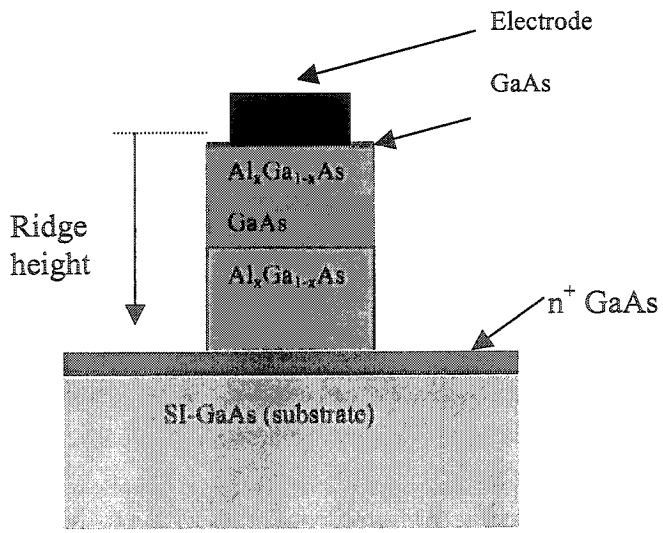

Figure 4.6 Cross section of the ridge optical waveguide of the preliminary design. The width of the waveguide is 8 μm, and the top electrode is 7 μm.

Table 4.2 Parameters of optical waveguide of the preliminary design

Material layers	Layer Thickness (um)	Doping Type	Doping Level (cm^{-3})	Refractive index
GaAs	0.1	-	Fully depleted	3.3704
$Al_{0.07}Ga_{0.93}As$	0.9	-	Fully depleted	3.3382
GaAs	0.8	-	Fully depleted	3.3704
$Al_{0.07}Ga_{0.93}As$	2.7	-	Fully depleted	3.3382
GaAs	0.4	n^+	1×10^{18}	3.3704
GaAs	250	Semi-Insulating	1×10^{8}	3.3704

The ridge waveguide of a preliminary design is shown in Figure 4.6, and detailed dimensions are given in Table 4.2. The waveguide consists of GaAs- $Al_{0.07}Ga_{0.93}As$ with GaAs core layer, approximately 0.8 μm thick and lower and upper claddings of $Ga_{0.93}Al_{0.07}As$ of thickness 2.7 μm and 0.9 μm, respectively. In order to minimize the optical loss due to the proximity of electrode and material absorption loss, both the top cladding layer and bottom cladding layer have been considered for the waveguide design. A thin layer of GaAs is used above the top cladding layer to prevent AlGaAs layer from oxidization. Below the bottom cladding layer lies a thin n^+ GaAs layer on SI GaAs. The Commercial software package Rsoft based on the Beam Propagation Method (BPM) was used to design single mode waveguides[56][57]. Both the thickness of n^+ layer and the ridge height 4.5 μm mainly come from the microwave simulation. Rsoft simulations suggest that the above ridge waveguide supports single mode propagation with the thickness of the core needs to be no more than 0.8 μm. Please note that the supported mode is the TE mode, the focus of our study.

A waveguide with 8 μm can support a single mode when the thickness of the core layer along with the material composition in the clad and core layers are properly selected. In the case of GaAs and $Al_{0.07}Ga_{0.93}As$ used as core and cladding layer, respectively, 0.8 μm thick waveguide core can support a single mode.

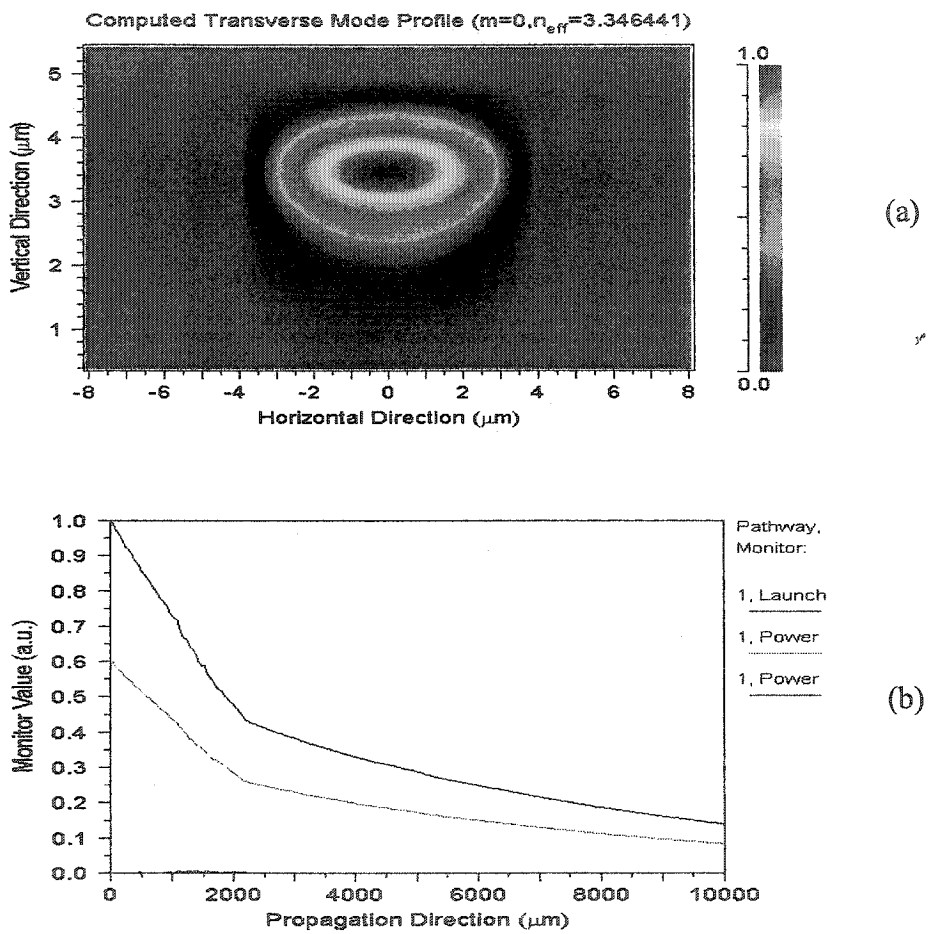

Figure 4.7 Calculated fundamental TE mode of the waveguide shown in Figure 4.6. (a) Transverse mode profile (b) Propagation of the mode. The green line represents the power confined by the GaAs core layer, the red line represents the power contained in the n^+ layer and the blue line represents the power contained in the waveguide.

As shown in Figure 4.7, the fundamental TE mode of this waveguide is very lossy, with the propagation loss around 8.44 dB/cm. The reason for such a high propagation loss can

be traced from Figure 4.7 (a). The optical mode is so close to the n+ layer and the substrate that it leaks much power into the n^+ layer and the substrate as it propagates.

One effective way to prevent the leakage of the mode into the highly doped layer and the substrate is to use a thick bottom cladding layer. As illustrated in Figure 4.8, the propagation loss decreases with an increase of the bottom cladding layer thickness, and propagation loss becomes less than 0.1 dB/cm if the bottom cladding layer is 5 μm thick.

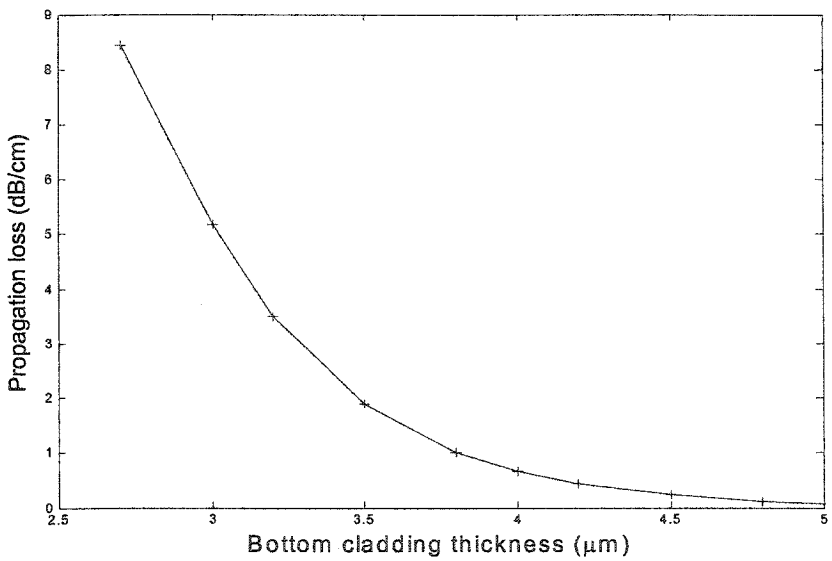

Figure 4.8 Propagation loss vs bottom cladding thickness.

To reduce the propagation loss, one should thicken the bottom cladding layer to prevent the leakage of the optical mode into the region with high free carrier concentration. However, Equation (2.25) indicates that a low drive voltage requires small depletion width d (ridge height), which suggests a thin bottom cladding layer. To solve this conflict, a novel approach has been taken to shape the tail of the optical mode to reduce the leakage into the high free carrier concentration region and to effectively reduce the thickness of

undoped bottom cladding layer [40]. In this technique, thin layers of $Al_yGa_{1-y}As$, $x<y\leq 1$ ($x=0.07$ here), are inserted in the bottom cladding layer. The presence of these thin layers of lower index material suppresses the tail of the fundamental mode and thereby reduces the leakage into the region of high free carrier concentration. Furthermore, the insertion of these thin layers dramatically reduces the thickness of the bottom cladding layer so that drive voltage is lowered effectively. The composition, thickness and the position of the inserted thin $Al_yGa1_{-y}As$ are optimized so that the original waveguide parameters (effective index, ...) do not change significantly while the total cladding thickness is greatly reduced and the mode confinement is improved. In our design, AlAs thin layers are inserted into the undoped bottom cladding layer. The cross section view of this waveguide is shown in Figure 4.9. The only difference between this waveguide and the one shown in Figure 4.6 lies in that thin AlAs layers are inserted into the bottom cladding layer in this waveguide. Table 4.3 presents the layer structure for this waveguide.

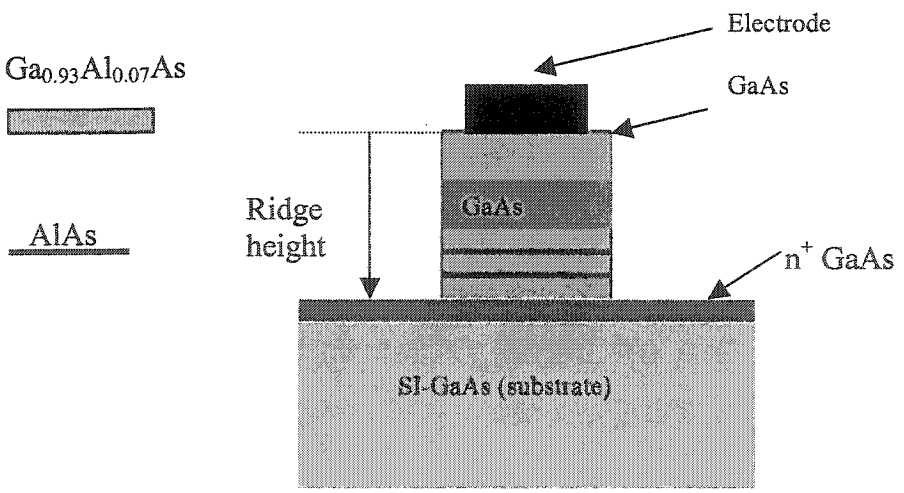

Figure 4.9 Cross section of the ridge optical waveguide of the final design. The width of the waveguide is 8 μm, and the top electrode is 7 μm wide.

Table 4.3 Heterostructure epitaxial layers of a ridge waveguide with two thin layers of AlAs inserted in the bottom clad

Layer#	Material	Thickness (μm)	Function	Doping Level (cm^{-3})	Refractive index
1	GaAs	0.1	Cap layer	Fully depleted	3.3704
2	$Al_{0.07}Ga_{0.93}As$	0.9	Top clad	Fully depleted	3.3382
3	GaAs	0.8	Core	Fully depleted	3.3704
4	$Al_{0.07}Ga_{0.93}As$	0.9	Bottom clad	Fully depleted	3.3382
5	AlAs	0.1	Insert layer	Fully depleted	2.9005
6	$Al_{0.07}Ga_{0.93}As$	0.8	Bottom clad	Fully depleted	3.3382
7	AlAs	0.1	Insert layer	Fully depleted	2.9005
8	$Al_{0.07}Ga_{0.93}As$	0.8	Bottom clad	Fully depleted	3.3382
9	GaAs	0.4	Highly doped layer	1×10^{18}	3.3704
10	GaAs	250	Substrate	1×10^{8}	3.3704

The computed transverse mode profile and propagation of this fundamental TE mode is shown in Figure 4.10. The optical TE mode of this waveguide is more confined in the vertical direction and thus is less lossy compared to that supported by the waveguide of the preliminary design shown in Figure 4.6. The propagation loss reduces to 0.25 dB/cm.

The optical properties, such as effective indices, mode profile, propagation loss and confinement factor for the fundamental TE mode supported in the ridge waveguide for both the preliminary design (optical waveguide without insert layers) and the final design (optical waveguide with insert layers), were calculated. The results are provided in Table 4.4. Here n_{eff} is the effective index for the fundamental TE mode, n_g is the group index of

this mode. PL is the propagation loss of the mode, a_x and a_y are the mode spot size in the lateral and vertical direction, and Γ is the confinement factor for the mode.

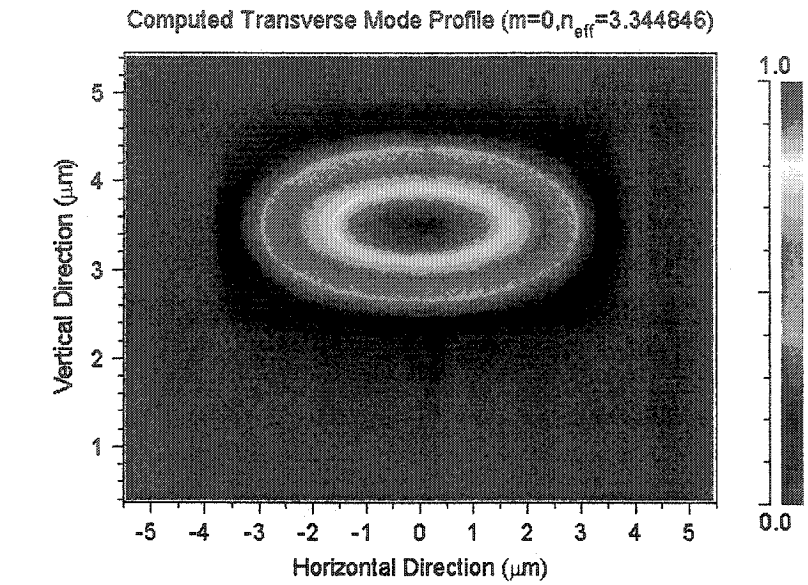

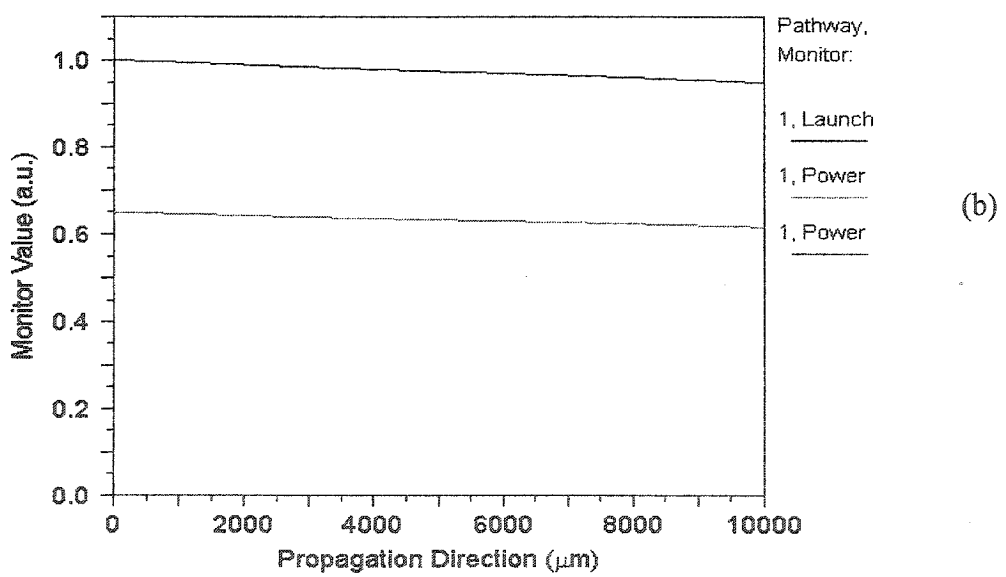

Figure 4.10 Calculated fundamental TE mode of the waveguide shown in Figure 4.9. (a) Transverse mode profile (b) Propagation of the mode. The blue line represents the power confined in the waveguide, the green line represents the power confined by the GaAs core layer, and the red line represents the power contained in the n^+ layer.

Table 4.4 Simulated parameters of the optical guided mode on two different heterostructure optical waveguides

Calculated Parameter	Waveguide with No Insert Layers (preliminary design)	Waveguide with Insert Layers (final design)
n_{eff}	3.346441	3.344846
n_g	3.516941	3.512457
PL (dB/cm)	8.44	0.25
a_x (μm) a_y (μm)	6.11 2.08	6.11 1.81
Γ	0.6 (decreases)	0.65
Coupling loss (dB/facet)	3.9	4.4

Optical waveguides are dispersive due to material and waveguide dispersion. As the above table indicates, there is some difference between the phase and group index of optical signal. The group index of an optical waveguide is given as:

$$n_g = n_{eff} - dn_{eff}/d\lambda \tag{4.16}$$

Where n_{eff} is the effective refractive index of the optical waveguide. Since optical information travels at the optical signal group velocity, the group velocity of the optical signal has to be matched to that of the microwave signal to achieve a maximum bandwidth for a given microwave loss.

4.3 The Design of PMS Traveling Wave Electro-optic Modulator on GaAs

4.3.1 Characterization of the Design Space of PMS

Before the PMS is finally designed, the design space of this structure needs to be characterized so that the rule of design and relationship between key parameters can be fully understood and optimization can be possible. The design space includes several factors such as the thickness of the n^+ layer, capacitance of the structure, inductance of the structure as well as microwave losses.

In order to characterize the design space, the PMS structure shown in Figure 4.11 is assumed to be the first test structure used to investigate the effect of the thickness of the n^+ layer on the microwave losses, capacitance and inductance. This test structure has the following dimensions and conductivities: 250 μm thick SI GaAs substrate with $\sigma=1\times10^{-6}$ mho/m; T μm thick n^+ -GaAs layer with $\sigma=5\times10^4$ mho/m, 2 μm thick undoped $Al_{0.07}Ga_{0.93}As$ layer; 1.4 μm thick undoped GaAs guiding layer; 1 μm thick undoped $Al_{0.07}Ga_{0.93}As$ layer layer on the top. The waveguide is 8 μm wide, and 1 μm Au is used as electrodes.

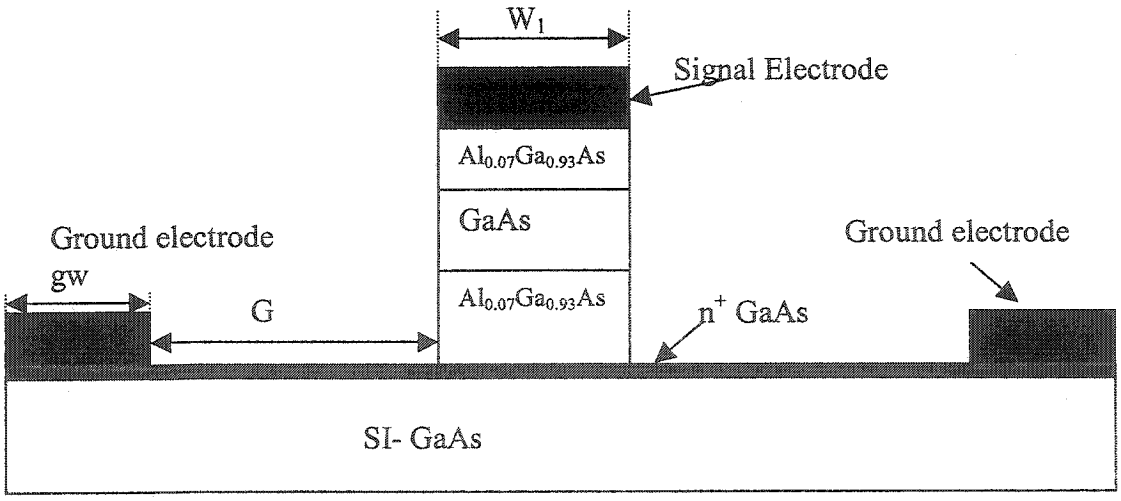

Figure 4.11 The test structure used to investigate the effect of the thickness of the n^+ layer on the microwave losses, capacitance and inductance. The width of the signal electrode W_1 is 8 μm, the width of both ground electrode gw is 6 μm and the gap between the ground electrode and the waveguide G is 8 μm.

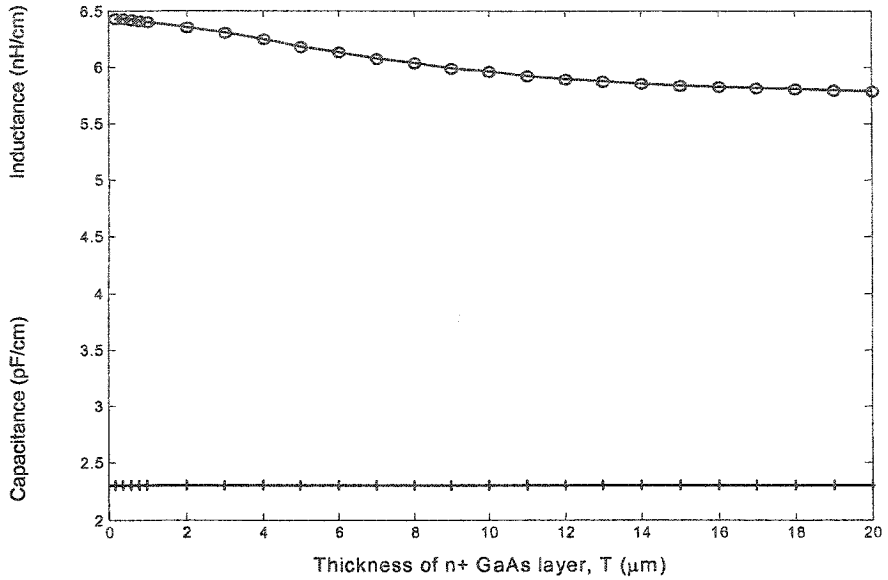

(a)

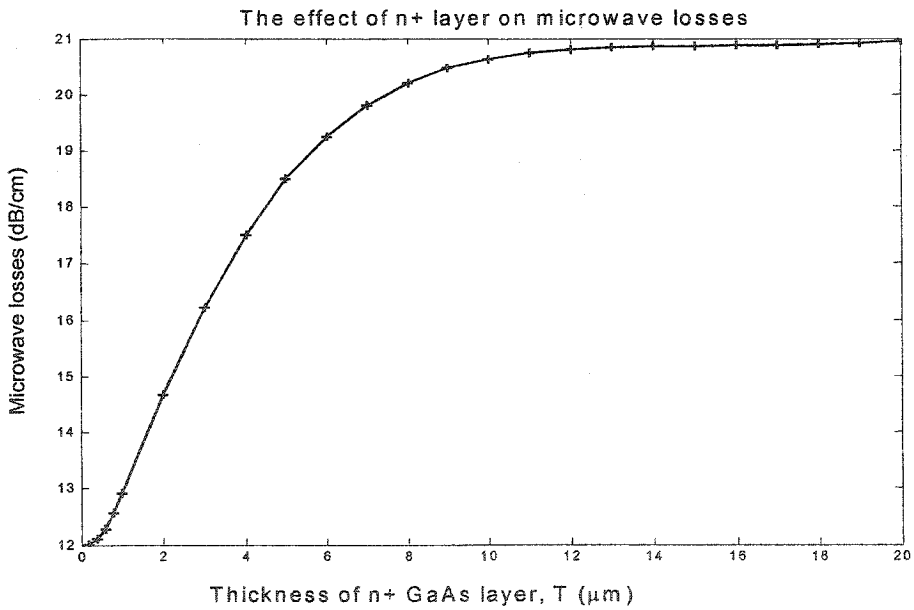

(b)

Figure 4.12 The effect of the thickness of the n^+ layer on the capacitance and inductance (a), and on the microwave losses (b). The simulation frequency is 30 GHz.

Figure 4.12 illustrates the effect of the thickness of n^+ layer on the capacitance, inductance, and microwave losses of the structure. The simulation frequency is 30 GHz. As shown in Figure 4.12 (a), the capacitance of the structure remains constant regardless of the increase

of the n^+ layer thickness while the inductance of the structure increases with the thickness of the n^+ layer until the thickness of the n^+ layer T is around 13 μm and tends to saturate after passing this point. Similarly, the microwave losses increase with the thickness of the n^+ layer to the point T=13 μm and do not increase anymore from this point, as demonstrated in Figure 4.12 (b).

The effect of the n^+ layer thickness on the capacitance and inductance and microwave losses of the PMS structure lies in that the PMS does support slow wave propagation and the electric field is confined above the n^+ layer while the magnetic field penetrates into the n^+ layer, as well as into the substrate depending on the thickness of the n^+ layer. Furthermore, once the thickness of the n^+ layer exceeds the skin effect depth, the magnetic field does not penetrate further. For this case, the test frequency is 30 GHz, thus the skin effect depth $\delta_s = \sqrt{\frac{2}{\omega\mu_0\sigma}} \cong 13$ μm. That's why the capacitance does not change with the thickness of the n^+ layer while both the inductance and microwave losses increase until the thickness of the n^+ layer exceeds the skin effect depth 13 μm and tend to saturate from this point.

From the above analysis, it can be concluded that the thickness of the n^+ layer needs to be kept within 1μm for relatively low microwave losses. In addition, such a thin n^+ layer ensures the propagation of the slow wave mode within the operation frequency (below 100 GHz) since the skin effect mode only starts to propagate when the frequency is around

4500 GHz for the 1 μm thick n^+ layer. In the following simulation, the thickness of the n^+ layer is chosen to be 0.4 μm to keep microwave losses low.

Next, the parameters affecting the capacitance of the structure are investigated. Since the electric field is confined above the n^+ layer, several factors may influence the capacitance, such as the width of the signal electrode, the height of the waveguide, the width of the ground electrode and the gap between the ground electrode and waveguide.

Figure 4.13 illustrates the effect of a varying gap between the ground electrode and the optical waveguide, G, on the capacitance of the structure. Though the inductance increases with G, the capacitance does not change regardless of the change of the gap G. The increase of inductance with increasing G is due to the fact that self-inductance of the ground electrodes increases as G increases.

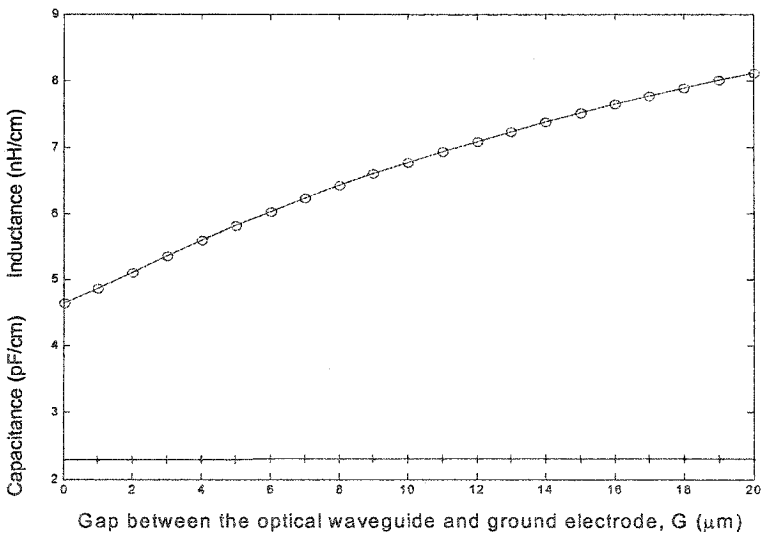

Figure 4.13 The effect of the gap between the ground electrode and the optical waveguide on the capacitance and inductance of the structure. The test structure is shown in Fig. 4.11, 0.4 μm thick n^+ layer is used, and all the other dimensions are kept the same as before except that G varies from 0 to 20 μm. The simulation frequency is 30 GHz.

Figure 4.14 demonstrates the effect of the ground electrode width, gw, on the capacitance and inductance of the structure. Though the inductance changes with the ground electrode width, the capacitance of the structure remains almost constant.

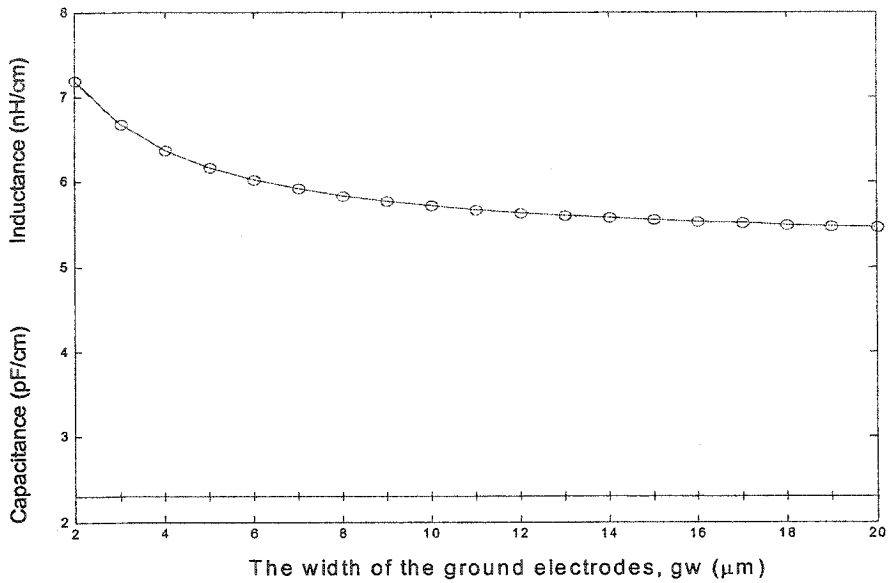

Figure 4.14 The effect of the width of the ground electrodes on the capacitance and the inductance of the structure. The test structure is shown in Figure 4.11, 0.4 μm thick n^+ layer is used, and all the other dimensions are kept as before except that gw varies from 2 to 20 μm. The simulation frequency is 30 GHz.

Figure 4.13 and Figure 4.14 demonstrate that the ground electrode width and the gap between the ground electrode and the optical waveguide only affect inductance, but do not influence the capacitance of the structure. This implication of this conclusion is that the electric field and magnetic field are separated in space with the electric field only confined in the central area (waveguide area) above the n^+ layer.

To investigate the effect of the signal electrode width, and of the waveguide height on the capacitance of the structure, a simplified structure, as shown in Figure 4.15, is utilized as

the test structure. The simplification is valid because the dielectric constant of $Al_{0.07}Ga_{0.93}As$ (12.96) is very close to that of GaAs (13.18) based on the equation $\varepsilon_{alGaAs}=13.18-3.12x$ for $Al_xGa_{1-x}As$ [58]. Thus one layer with the dielectric constant $\varepsilon=(\varepsilon_{alGaAs}+\varepsilon_{GaAs})/2$ is equivalent to the three undoped layers as shown in Fig. 4.11 (this layer height equals to the waveguide height, so we call this layer height H as the waveguide height later on). The simplification here is to speed up the simulation and reduce the variable with only one variable H represents the total thickness of three layers.

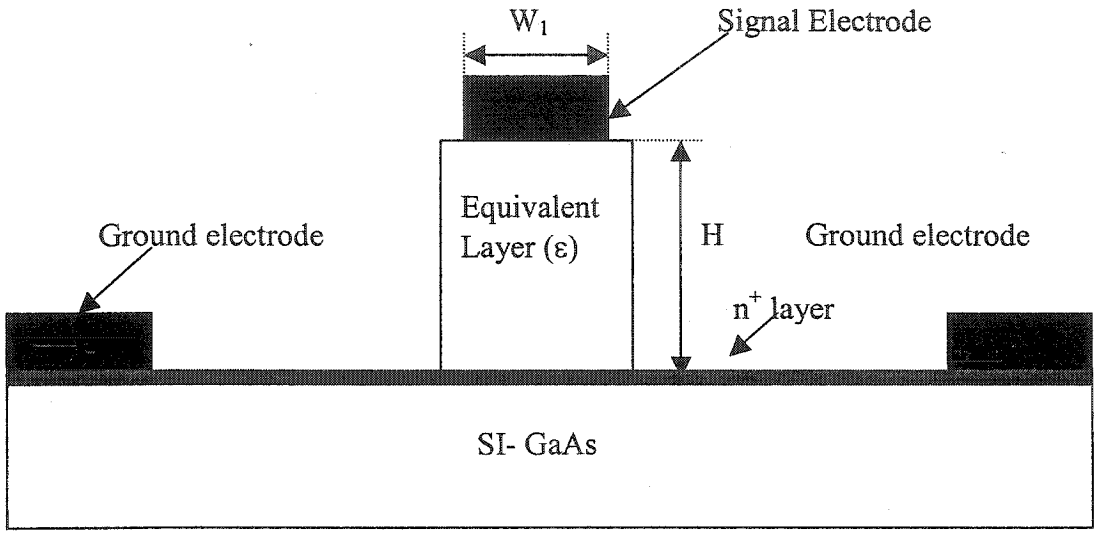

Figure 4.15 The test structure used to investigate the effect of the signal electrode width and the waveguide height on the capacitance of the structure. 0.4 μm thick n^+ layer is used, the ground electrode is 6 μm wide, and the gap between the ground electrode and the width of the equivalent layer is 8 μm. The width of the equivalent layer is 8 μm. The simulation frequency is 30 GHz.

Figure 4.16 provides a contour map of capacitance per unit length vs signal electrode width W_1 and waveguide height H. This "capacitance map" provides guidance for designing the PMS with the designated characteristic impedance and phase velocity. For example, the refractive index of GaAs at λ=1.55 μm, is about 3.37, so the microwave index of PMS needs to be close to it for velocity matching in the traveling wave modulator case, that corresponds to the phase velocity V_p=8.895 cm/ns. According to equations (3.36) and

(3.37), the capacitance per unit length needs to be 2.25 pF/cm while the inductance per unit length needs to be 5.62 nH/cm to obtain an PMS line with the characteristic impedance of 50 Ω and V_p=8.895 cm/ns. From the capacitance map, we can obtain the corresponding pairs of W_1 and H that can offer a specific capacitance per unit length. For example, to obtain the capacitance 2.25 pF/cm, H needs to be about 4.5 μm if W_1=7 μm while H needs to be approximately 3.7 μm if W_1=4 μm.

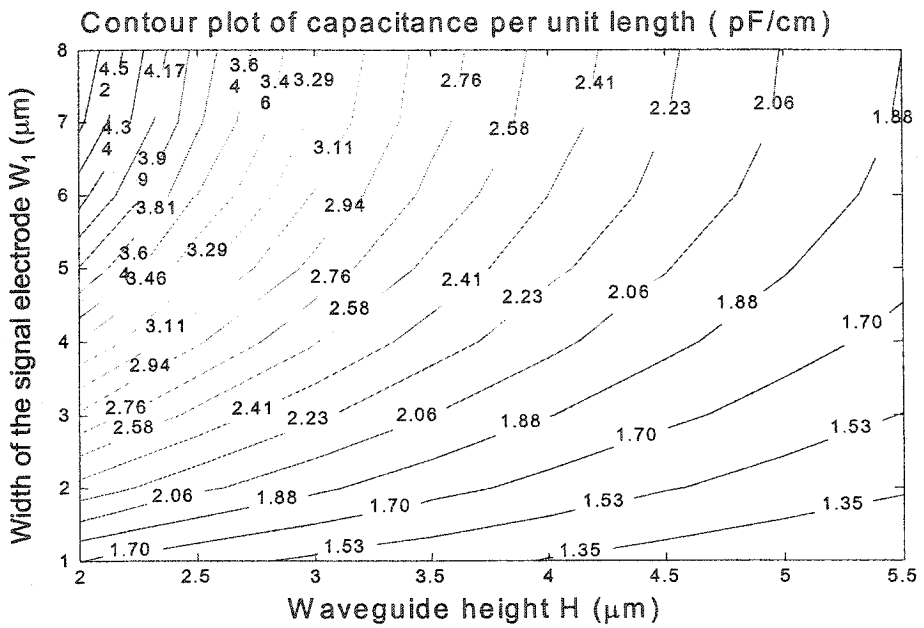

Figure 4.16 Contour plot of capacitance per unit length vs the width of the signal electrode and waveguide height H. The simulation frequency is 30 GHz.

Though different pairs of W_1 and H may offer the same value of capacitance per unit length according to the capacitance map, larger H is more beneficial due to lower microwave loss and lower optical loss. As shown in Figure 4.17, the microwave losses decrease with increasing H while increasing W_1 decreases the microwave losses. With larger H, less magnetic field penetrate into the n^+ layer and the substrate, resulting in less dielectric loss. Furthermore, larger H corresponds to larger W_1, and larger W_1 means less

metal loss. In addition, larger H also causes the optical mode to be further away from the n^+ layer and the substrate, thus suppresses the optical propagation loss.

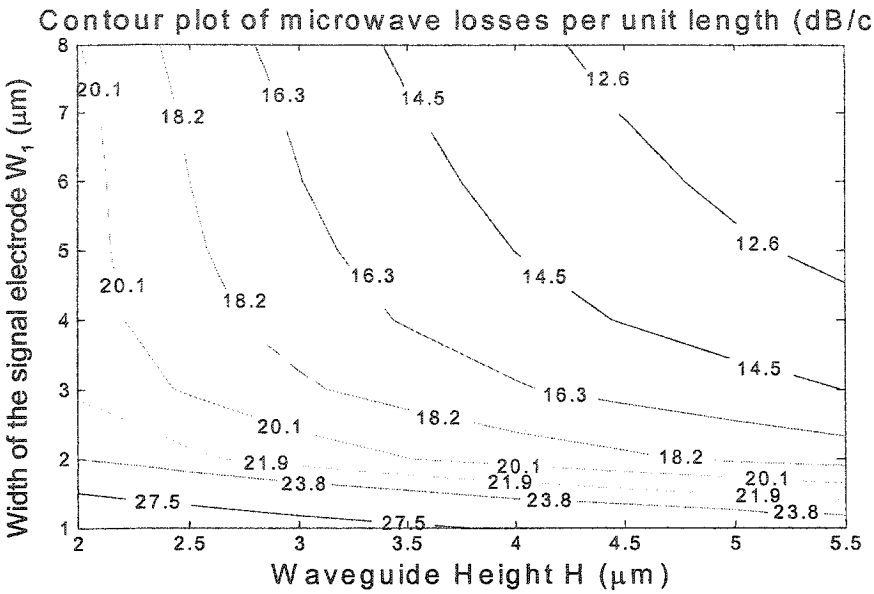

Figure 4.17 Contour plot of microwave losses per unit length vs the width of the signal electrode, W_1, and waveguide height, H. The simulation frequency is 30GHz.

According to the above analysis, to obtain a PMS line with 50 Ω characteristic impedance and phase velocity of 8.895 cm/ns, the waveguide height is chosen to be 4.5 μm and the signal electrode width is 7 μm. These dimensions will be used in the next test structure to obtain the inductance map for a specific inductance per unit length.

Once the signal electrode width and the corresponding waveguide height are chosen, the capacitance per unit length of the PMS line will be known. However, the inductance per unit length needs to be known, depending on the ground electrode width and the gap between the optical waveguide and the ground electrode, and microwave loss needs to be minimized as much as possible. Figure 4.18 shows the test structure used to examine the

effect of the ground electrode width, and of the gap between the optical waveguide and the ground electrode, on inductance, and on microwave losses too.

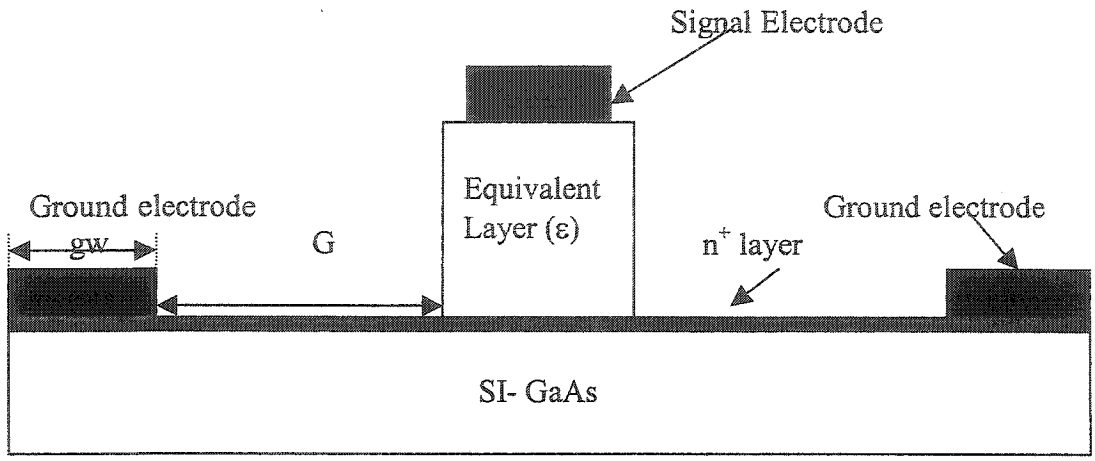

Figure 4.18 The test structure used to investigate the effect of the ground electrode width and of the gap between the ground electrode and the optical waveguide on the inductance, and on microwave losses of the structure. 0.4 μm thick n^+ layer is used, the equivalent layer is 8 μm wide and 4.5 μm thick, and the width of the signal electrode width is 7 μm The simulation frequency is 30 GHz.

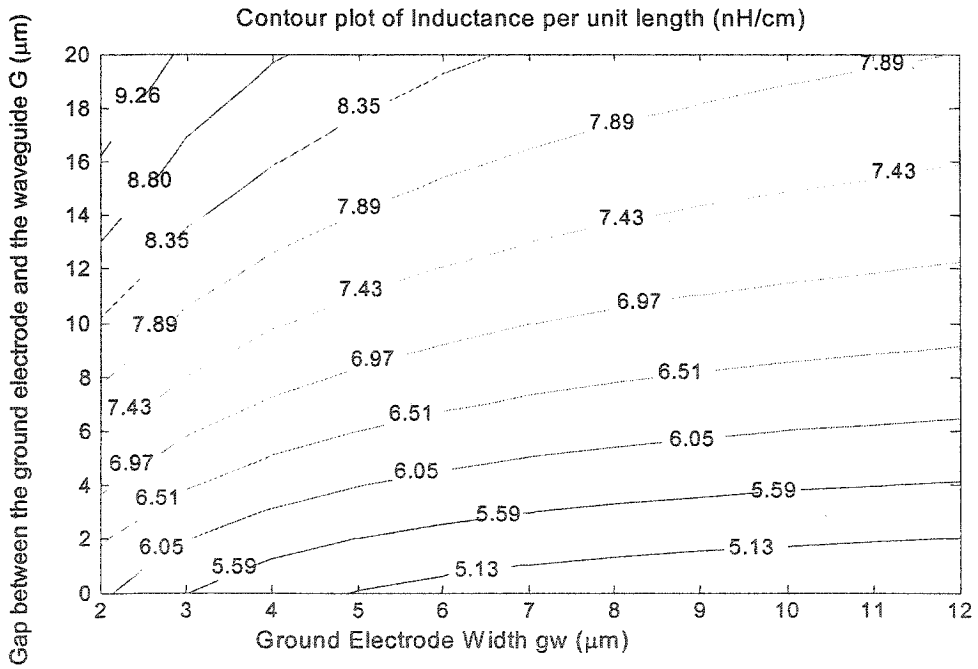

Figure 4.19 Contour plot of inductance per unit length vs the ground electrode width gw and the gap between the ground electrode and the waveguide G. The simulation frequency is 30 GHz.

Figure 4.19 shows the inductance vs the ground electrode width gw and the gap between the ground electrode and the optical waveguide G. As Figure 4.19 shows, increasing gw decreases the inductance and the inductance tends to saturate as gw increases further whereas increasing G increases the inductance.

The effect of the ground electrode width gw, and of the gap between the ground electrode and the optical waveguide G, on the microwave losses are shown in Figure 4.20. Apparently, the microwave losses decrease dramatically with the increase of gw when gw is small, such as 2 μm or 3 μm; however, the microwave losses increase slowly with the increase of gw when gw becomes relatively large, such as 10 μm. It seems that there is always a specific G that offers the minimum microwave losses, and G shifts with the change of gw.

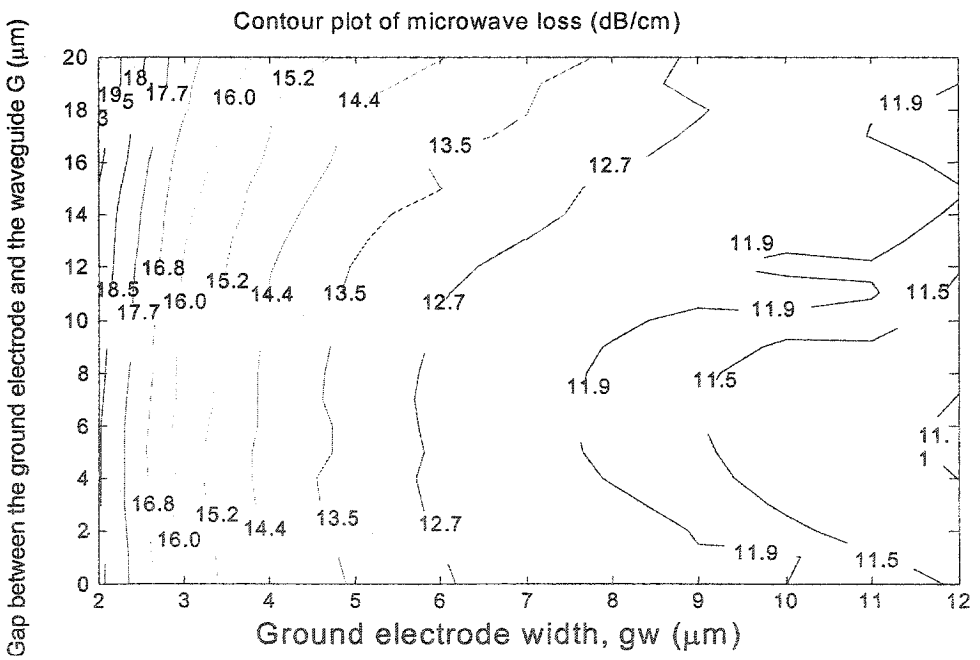

Figure 4.20 Contour plot of microwave losses vs gw and G. The simulation frequency is 30 GHz.

The inductance map and the microwave losses map provide guidance for selecting the ground electrode width gw as well as the gap between the ground electrode and the optical waveguide, and for optimizing the design. For example, to obtain the inductance of 5.62 nH/cm and low microwave losses, gw is chosen to be around 12 μm and G is about 5 μm.

4.3.2 Design of a PMS Traveling Wave Electro-optic Modulator on GaAs with 50 Ω Characteristic Impedance and Velocity Matching

From the design space of PMS, a PMS line with 50 Ω characteristic impedance and velocity matching can be easily designed. To achieve a 50 Ω characteristic impedance and velocity matching, the capacitance per unit length needs to be around 2.25 pF/cm while the inductance per unit length needs to be close to 5.62 nH/cm according to equations (3.36) and (3.37). To obtain a PMS line with 50 Ω characteristic impedance and velocity matching, the required signal electrode width W_1, the waveguide height H, the ground electrode width gw and the gap between the ground electrode and optical waveguide G can be selected using the capacitance map, inductance map and microwave loss maps. Figure 4.21 provides the cross sectional view of the designed PMS traveling wave electro-optic modulator on GaAs, and Table 4.5 illustrates the detailed dimension of the PMS electrode with 50 Ω characteristic impedance and velocity matching. The dimension of the optical waveguide is shown in Table 4.3.

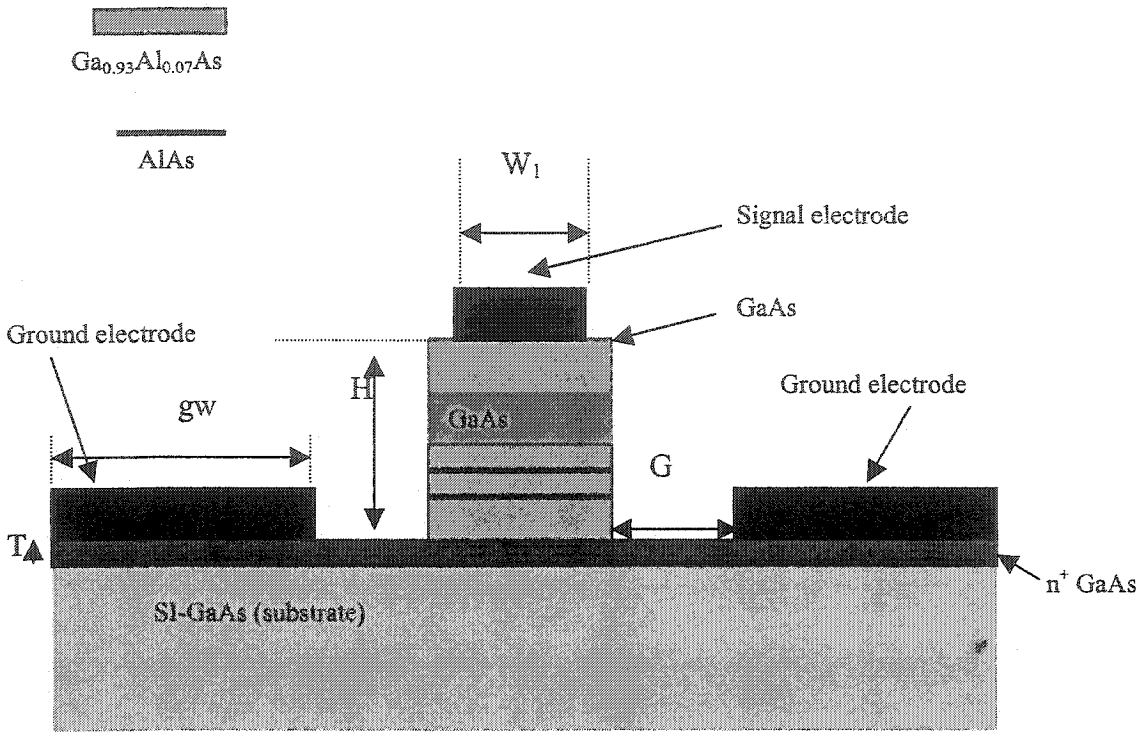

Figure 4.21 Cross sectional view of PMS traveling wave electro-optic modulator. The dimensions of optical waveguide are given in Table 4.3, and the dimensions of the PMS are shown in Table 4.5. The width of the optical waveguide is 8 μm. Here 1 μm thick Au is used as the metal electrode.

Table 4.5 Dimensions of PMS with 50 Ω characteristic impedance and velocity matching

G (μm) (Gap between the waveguide and the ground electrode)	gw (μm) (Ground electrode width)	H (μm) (Waveguide height)	W_1 (μm) (Width of the signal electrode)	T (μm) (Thickness of n^+ layer)
5	12	4.5	7	0.4

Intensity modulation of the PMS traveling wave electro-optic modulator on GaAs is achieved by launching the light with a polarizer along the direction of $(1/\sqrt{2})(\hat{z}' + \hat{y}')$ at the input of the waveguide, and orienting an analyzer in the direction of $(1/\sqrt{2})(\hat{z}' - \hat{y}')$ at the output of the waveguide, where $\hat{z}'$ and $\hat{y}'$ are the [001] and $[\bar{1}10]$ optical axes of GaAs, respectively (see Figure 2.3 and Figure 2.8). The top view of the PMS traveling wave modulator is shown in Figure 4.22.

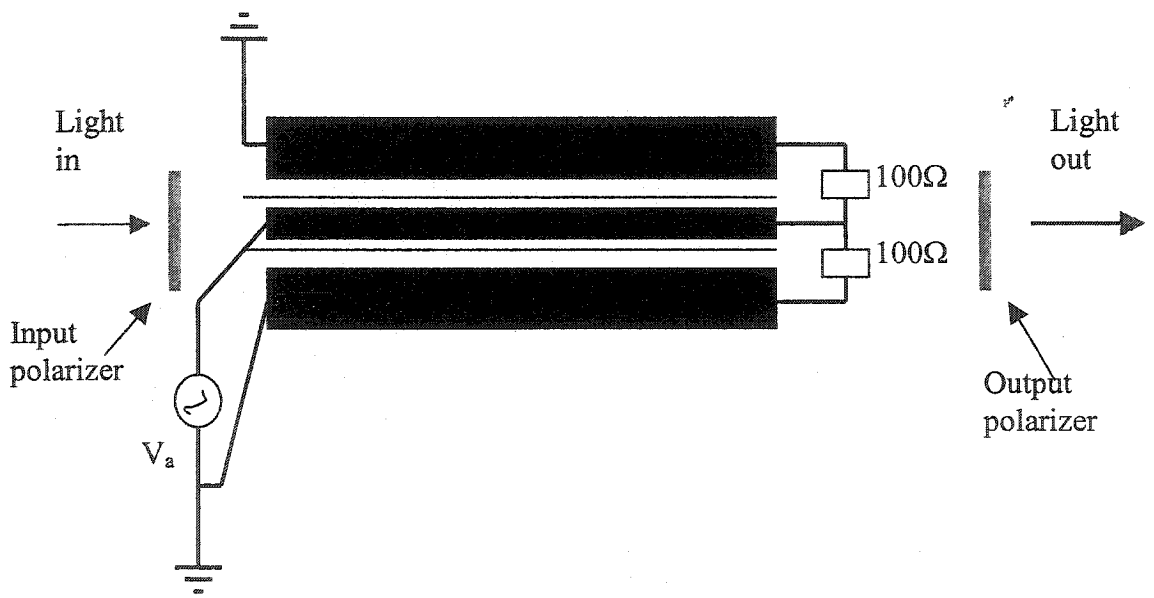

Figure 4.22 The top view of PMS traveling wave electro-optic modulator on GaAs.

Figures 4.23, 4.24, 4.25, 4.26 and 4.27 show the simulated results for the designed modulator. As Figure 4.23 illustrates, the capacitance and inductance per unit length are close to the targeted values, the capacitance per unit length is almost constant for the whole frequency band while the inductance per unit length drops rapidly at low frequency and then decreases very slowly.

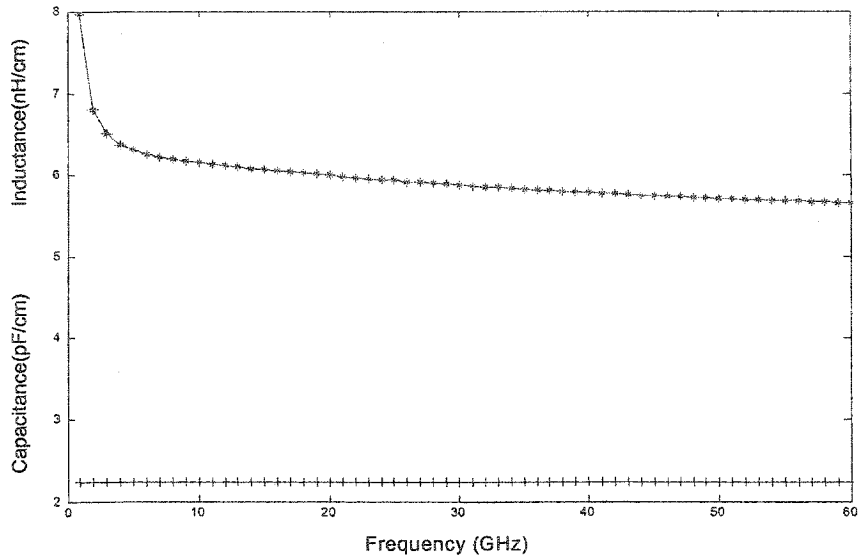

Figure 4.23 Capacitance per unit length and inductance per unit length vs frequency.

The characteristic impedance of the stimulated structure is shown in Figure 4.24. The characteristic impedance is close to 50 Ω for the whole frequency band.

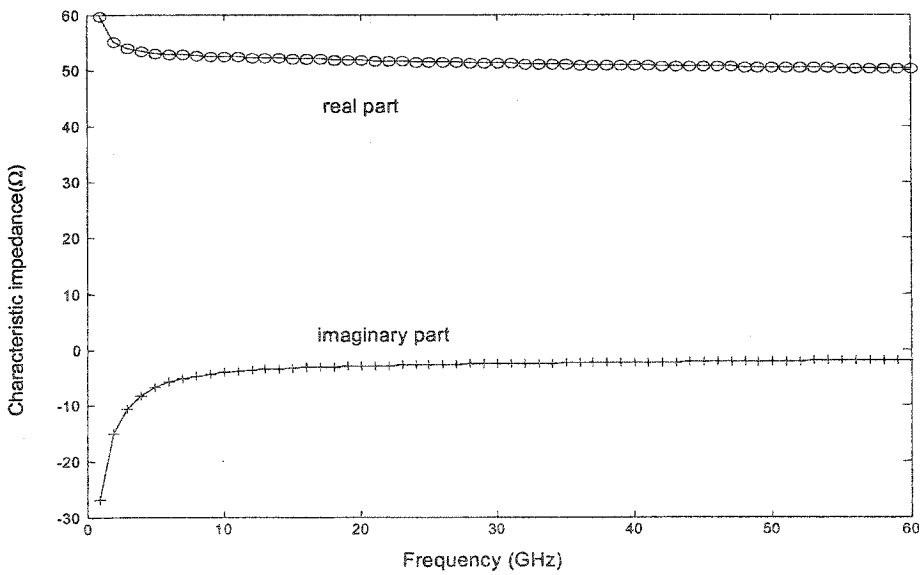

Figure 4.24 Characteristic impedance of the simulated PMS line vs frequency.

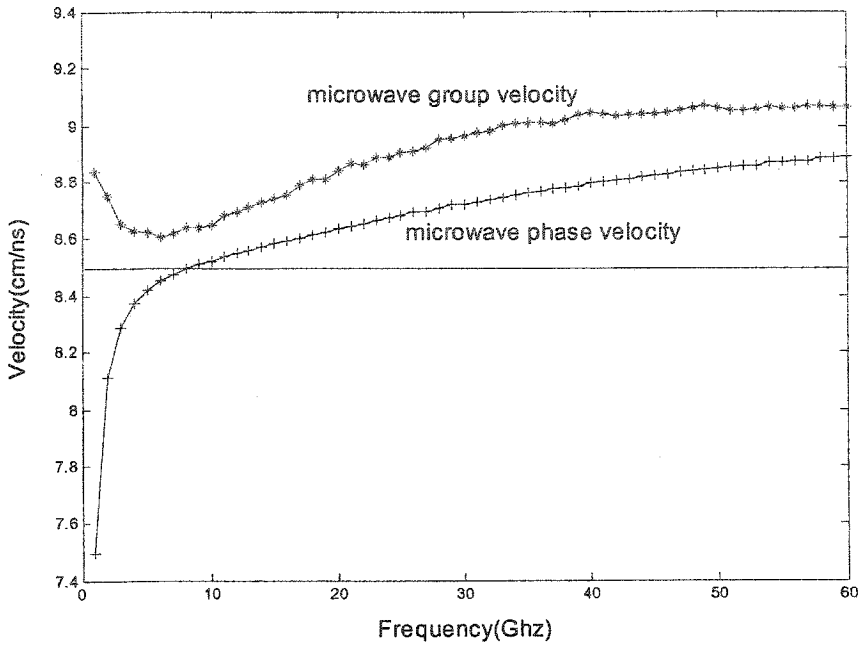

Figure 4.25 Microwave phase velocity and group velocity vs frequency. The black straight line represents the optical group velocity of the waveguide (n_g=3.512457 as shown in Table 4.4 corresponds to the optical group velocity 8.54 cm/ns).

Figure 4.25 demonstrates microwave phase velocity and group velcity versus frequency. As Figure 4.25 shows, PMS structure is quite dispersive under 6 GHz and less dispersive as frequency increases. Since the PMS is dispersive, its phase and group velocities are different, with the phase and group velocities given by

$$v_p = \frac{\omega}{\beta}, \qquad v_g = \frac{\partial \omega}{\partial \beta} \tag{4.17}$$

where ω and β have their usual meaning. Since the energy is transmitted at the group velocity, thus it is the microwave group velocity that needs to be matched to the optical group velocity. Of course, for a non-dispersive structure, v_p=v_g. For this case, the velocity mismatch is approximately 5%.

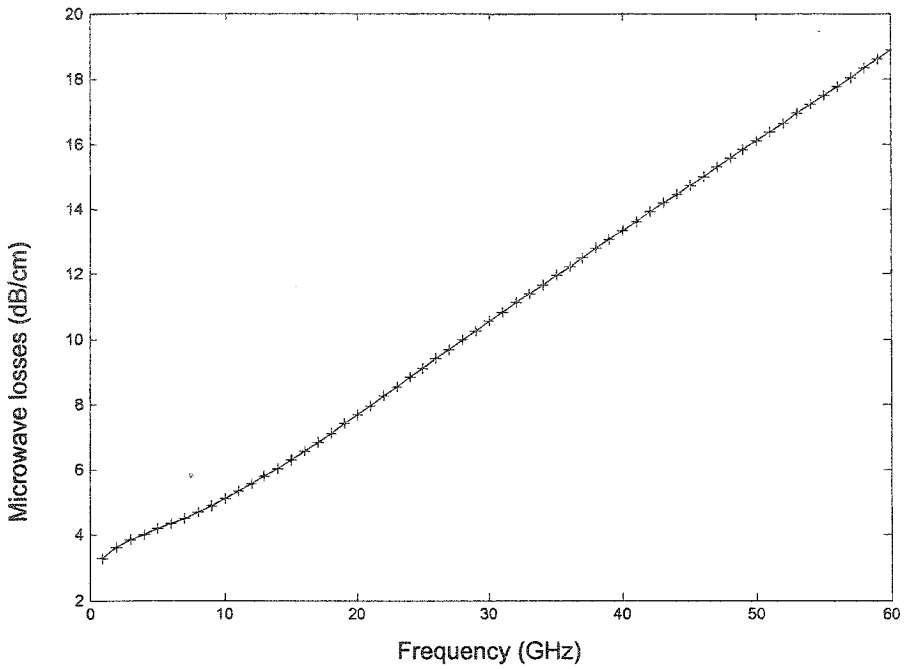

Figure 4.26 Microwave losses vs frequency.

As shown in Figure 4.26, the microwave losses increase with frequency and reach 6.32 dB/cm and 13.4 dB/cm at 15 GHz and 40 GHz, respectively. For 60 GHz, the microwave losses are only 18.9 dB/cm.

In our design, the length of the device is normalized to 1cm, thus the frequency response of the PMS traveling wave electro-optic modulator can be calculated from equation (3.22). Fig. 4.27 shows the frequency response of the PMS modulator with matched input and output impedances. For the PMS, the electrical 3 dB bandwidth of 15 GHz and the optical 3 dB bandwidth of 40 GHz are achieved. As discussed in Chapter 3, 6.34 dB loss determines the electrical 3 dB bandwidth when velocity and impedance matching is obtained, therefore high microwave losses in PMS result in a narrow electrical 3 dB

bandwidth while quite small velocity mismatch even at high frequency contributes to an acceptable optical 3 dB bandwidth.

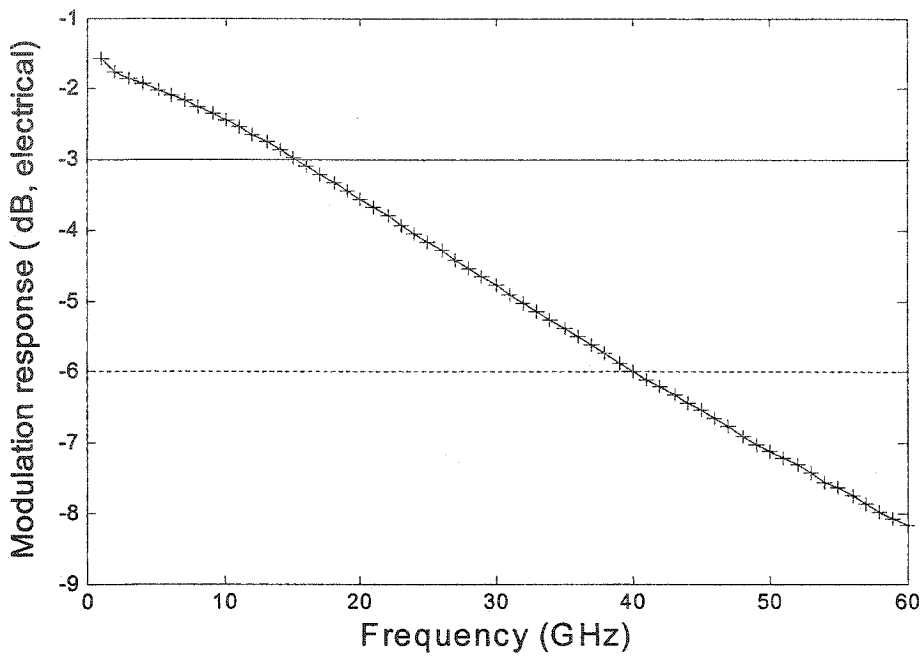

Figure 4.27 Modulation frequency response of the PMS traveling wave electro-optic modulator on GaAs with 50 Ω characteristic impedance. The black straight line, and the black dotted line represent the electrical 3 dB and the optical 3 dB (electrical 6 dB) respectively.

The expression for V_π with $E_{dc,rf}$ along the direction <001> can be obtained from equation (2.18):

$$V_\pi = \frac{\lambda d}{n_0^3 r_{41} l \xi} \tag{4.18}$$

where λ is the optical wavelength, l is the length of the device, here normalized to 1cm, r_{41} is the electro-optic coefficient for GaAs, and ξ is the overlap integral between an optical mode and a microwave field, and d is the depletion width. n_0 is 3.5124, the optical group index of the waveguide, and r_{41}=1.42×10^{-12}(m/v), and ξ is approximately unity for PMS,

since the layers above the n^+ doped GaAs layer contain most of the optical mode that is indicated by the low propagation loss of the waveguide from Table 4.4, and d=4.5 μm from Table 4.4. The calculated $V\pi$ for PMS is about 11.3 V·cm. Such a high $V\pi$ is caused by the large depletion width d. Thus, to reduce $V\pi$, the depletion width d should be decreased. For the 1cm long device, the figure of merit (the ratio of bandwidth (f_{3dBe}) to the half wave voltage) is about 1.33.

According to Table 4.4, the optical insertion loss is estimated to be 9.05 dB for the modulator. Here, the optical insertion loss is calculated as the propagation loss over the given length of the active region (1 cm) plus twice the coupling loss.

Some important parameters of the designed modulator with the PMS electrodes are listed in Table 4.6.

Table 4.6 Important parameters for the designed modulator

Length (cm)	f_{3dBe} (GHz)	f_{3dBo} (GHz)	Optical Insertion Loss (dB)	V_π (V)	Figure of Merit (GHz/V)
1	15	40	9.05	11.3	1.33

4.4 Summary

For the design and optimization of PMS modulator electrodes to satisfy impedance matching and velocity matching, the following rules should be followed based on the above analysis:

(a) The thickness of n^+ GaAs should be submicron to reduce the microwave loss and ensure slow wave propagation

(b) Corresponding waveguide width, height and signal electrode width are chosen to achieve a specific capacitance, according to the "capacitance map". Larger electrode widths and wavguide heights are preferred due to low microwave losses and low optical propagation loss.

(c) The inductance map and microwave loss maps need to be determined once the waveguide width, height and the signal electrode width are selected.

(d) The proper ground electrode width and the gap between the optical waveguide and the ground electrode are selected based on the inductance map and the microwave loss map, to achieve the demanded inductance and minimum microwave losses.

As discussed in chapter 3, there are several requirements concerning high speed electro-optic traveling wave modulators, such as velocity matching, 50 Ω characteristic impedance matching, low microwave loss, large overlap integral, low optical insertion loss, and low V_π. All of these requirements are often coupled with each other through some common parameter, and may be conflicting depending on the specific structure, therefore the potential of a specific structure as a high speed traveling wave modulator is quite dependent on whether the structure enables the decoupling of the microwave and optical designs. Firstly, simulations demonstrate that a wide top electrode and large waveguide height (depletion width) are needed to reduce the microwave losses in PMS, which is the dominant factor limiting the bandwidth of this structure when velocity mismatch is quite small. Low optical propagation loss also requires large waveguide height. Secondly, a low

V_π demands a small depletion width (waveguide height). Thirdly, The optical waveguide, which needs to support single mode propagation and to guarantee its good coupling with laser and fiber respectively, prevents the use of wide signal electrode. In addition, top electrode width along with the waveguide height and width determines the capacitance and in turn determines the characteristic impedance and phase velocity. These design requirements cause conflicts through some parameters such as the waveguide height and waveguide width and thus makes the design and optimization of a PMS very difficult. In short, optical design and microwave design are so tightly interleaved with each other in PMS that they can not be decoupled, thus the potential of PMS as high-speed traveling wave modulator electrode is somewhat limited, with the electrical 3 dB bandwidth less than 20 GHz. To work as a high-speed modulator, a new architecture is needed. In the next chapter, a different slow wave structure has been suggested, in which the uniform coplanar strip is periodically loaded with small capacitors. Its potential of working as a high-speed traveling wave modulator electrodes will be discussed.

CHAPTER 5

Design and Modeling of GaAs Traveling Wave Electro-optic Modulators Based on Capacitively Loaded Coplanar Strips Using Doped Layers

In this chapter, capacitively loaded coplanar strips have been designed as the electrodes in GaAs traveling wave electro-optic modulators. A n+ doped epitaxial layer has been used to guarantee a good overlap between the optical field and microwave field, and effectively reduce the loaded capacitance. This study goes beyond [41][42] in two respects. First, the design space of the CPS loaded electrodes is fully characterized so that it provides guidance for the future design and optimization of GaAs traveling wave electro-optic modulators with CPS loaded electrodes. Next, the electrical 3 dB bandwidth of the designed modulators is predicted to exceed those reported in [41][42], and the figure of merit of the designed modulators is also higher.

5.1 GaAs Traveling Wave Electro-optic Modulators Based on Capacitively Loaded Coplanar Strips Using Doped Layers

As discussed in last chapter, the PMS, a variant of the MIS, has a limited frequency response in a GaAs traveling wave electro-optic modulator thus in this chapter the potential of periodic structure as the electrodes for high speed GaAs traveling wave modulators will be investigated.

R.G. walker [41][42] reported a high speed GaAs traveling wave electro-optic modulator, in which uniform coplanar strips are periodically loaded with small capacitors with a highly n doped layer used in the epitaxial layers as shown in Figure 1.7. For convenience, Figure 1.7 is reproduced here as Figure 5.1.

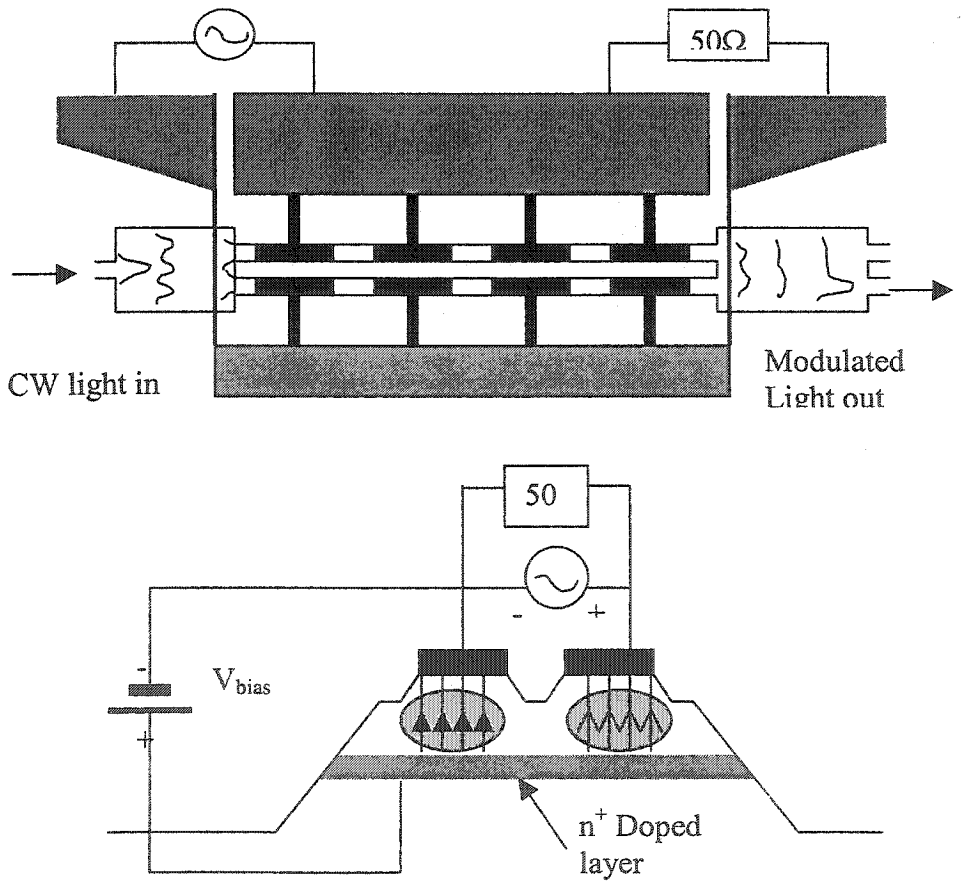

Figure 5.1 Schematic of traveling-wave Mach-Zehnder modulator using capacitively loaded CPS [42. Fig.1].

The optical structure is a Mach-Zehnder interferometer comprising equal optical split and recombination at the input and output, respectively, between which a pair of electro-optic phase modulation waveguides are driven in antiphase (push-pull) to give chirp free intensity modulation. The GaAs /AlGaAs epitaxial layers are grown on SI GaAs substrate. A conductive n+ layer is grown below the waveguide core and contributes to the back-to-back connection between the Shottky-i-n double heterostructure waveguides. The capacitive elements used are the reverse-biased capacitance of the Schottky-i-n junction. The reverse-biased Schottky contact is the key to low drive voltages. Firstly, it ensures that the electric field overlaps the optical mode very well. Secondly, it provides a series push-pull drive. Half the applied voltage drops across each arm of MZI, and thus the total loading capacitance is reduced by factor of 2. In other words, the effective capacitive load offers the availability of increasing the interaction length of electrical and optical fields, which decreases the drive voltage. On the other hand, these separate capacitors do not carry any axial currents in the transmission line, therefore the microwave loss is dominated by that of the coplanar line. This offers the possibility of maintaining low microwave loss while both impedance matching and velocity matching are achieved.

Such a device of active length 10 mm with 40 segments at 70% fill was reported to achieve an electrical 3 dB bandwidth of 50 GHz and V_{π} of 13 V [42].

5.1.1 Periodic Structures

Periodic structures such as periodically loaded coplanar strips with small capacitors have been suggested here as modulator electrodes, as shown in figure 3.6(a). One basic property of the periodic structure is the support of waves with phase velocities much less than the velocity of light, which makes it suitable for use in GaAs traveling wave modulator. For a uniform transmission line, such as coplanar strips, the characteristic impedance Z_u and the phase velocity v_{pu} are given by the fundamental relations:

$$Z_u = \sqrt{\frac{L}{C_u}} \tag{5.1}$$

$$v_{pu} = \frac{1}{\sqrt{LC_u}} = \frac{c_0}{n_u} \tag{5.2}$$

where L and C_u are inductance and capacitance per unit length of the uniform transmission line respectively, c_0 is the speed of light in the free space, and n_u is the microwave index. From equation (3.28), with a relative permittivity for GaAs of 13.18, the value of n_u will be 2.66 for uniform CPS lines. The phase velocity of the transmission line can be reduced by increasing L or C_u, or both. Changing the dimensions of the uniform transmission line changes the capacitance and inductance of the line, however the LC_u product and therefore phase velocity will almost remain constant. Increasing C_u will automatically decrease L. However, when the uniform transmission line is periodically loaded with small capacitors, an effective increase in the shunt capacitance can be achieved without a corresponding decrease in the series inductance L. If the periodic interval is small compared with the wavelength, the loaded line will appear to be electrically smooth, with a characteristic impedance and phase velocity given by:

$$Z_0 = \sqrt{\frac{L}{C}} \tag{5.3}$$

$$v_p = \frac{1}{\sqrt{LC}} = \frac{c_0}{n_m} \tag{5.4}$$

where $C=C_u+C_l$. C_l is the loading capacitance per unit length, and n_m is the microwave effective index. Thus both the impedance and velocity will be reduced by the slow wave factor κ,

$$\kappa = \frac{Z_u}{Z_0} = \frac{v_{pu}}{v_p} = \frac{n_m}{n_{pu}} = \sqrt{(1+C_l/C_u)} \tag{5.5}$$

For velocity matching, n_m is set equal to n_g where n_g is the group index of the optical waveguide, with its value being 3.5284 (based on the design of the optical waveguide). From the above equations, the required value for the loading capacitance C_l is readily obtained:

$$C_l = \frac{n_g^2 - n_u^2}{cZ_0 n_g} \tag{5.6}$$

For Z_0=50 Ω, C_l is around 1.015 pF/cm. It follows from (5.5) that the unloaded Z_u should be 66.3 Ω and the unloaded capacitance should be 1.34 pF/cm. Such a capacitively loaded transmission line can be achieved using either doped or undoped epitaxial layers.

The other basic property of periodic structures lies in passband-stopband characteristics, that is the existence of frequency bands throughout which a wave propagates unattenuated (except for incidental conductor loss) along the structure, separated by frequency bands throughout which the wave is cut off and does not propagate. The frequency characteristic of a capacitively loaded transmission line is given by [53]:

$$\cos(\beta_l p) = \cos(\beta_u p) - Z_u \frac{\omega C_l p}{2} \sin(\beta_u p) \tag{5.7}$$

where β_l is the phase constant of the loaded transmission line, β_u and Z_u are the phase constant and characteristic impedance of the uniform (unloaded)transmission line, p is the periodicity of interval. Thus the cut off frequency of such a periodically loaded transmission line can be approximated by

$$f_{cut-off} \cong \frac{v_p}{2p} \tag{5.8}$$

A small periodicity needs to be chosen to stay well away from the cut off frequency of the structure so that dispersion is minimized. For p=100 μm and v_p =8.5 cm/nsec (to match a GaAs/AlGaAs optical structure at 1.55 μm wavelength), the cut off frequency is almost 425 GHz. This indicates that for frequencies below 100 GHz dispersion due to the periodicity of the structure is negligible.

5.1.2 Validation of Modeling

Due to a lack of detailed information, it is impossible to validate the model by simulating the original structure of [41][42] as shown in Figure 5.1. In addition, the properties of periodic structures are well known, and the guidelines for designing a periodic electrode for a GaAs modulator have already been given in the last section. Therefore, we will characterize the design space of capacitively loaded CPS electrodes following these design guidelines, and the validity of the modeling is checked in parallel to the characterization process.

5.2 Optical Structures

5.2.1 The Design of Single Mode Optical Waveguide

In order to offer a high overlap integral of electric field to optical mode, a n^+ doped layer is used in the design of the single mode optical wavguide. The target is to design a single mode waveguide with low propagation loss. The waveguide is of the strip-loaded variety since etch depths which give adequate confinement without multimode guiding are found to be a little less than the upper cladding thickness. For low propagation loss, bottom cladding of sufficient thickness is needed

Figure 5.2 illustrates a GaAs/AlGaAs waveguide cross section of the single mode waveguide designed here. The width of the ridge is 4 μm. The top electrode is 1 μm thick Au and this forms a Schottky contact with the epitaxial layers. The waveguide consists of GaAs-AlGaAs layers with GaAs core layer, approximately 0.6 μm thick, and lower and upper claddings of $Al_{0.3}Ga_{0.7}As$ of thickness of 0.45 μm and 2.3 μm, respectively. Above the upper cladding, 0.05 μm thick GaAs cap layer is placed to prevent oxidization of AlGaAs. Modulation fields are applied via the reverse biased Schottky-i-n junction. Below the lower cladding is a n^+ doped layer designed to limit the extent of the depletion zone to the vicinity of the guided light, thus this highly doped layer contributes to the high overlap integral of the electric field to the optical mode. The detailed dimensions are shown in Table 5.1

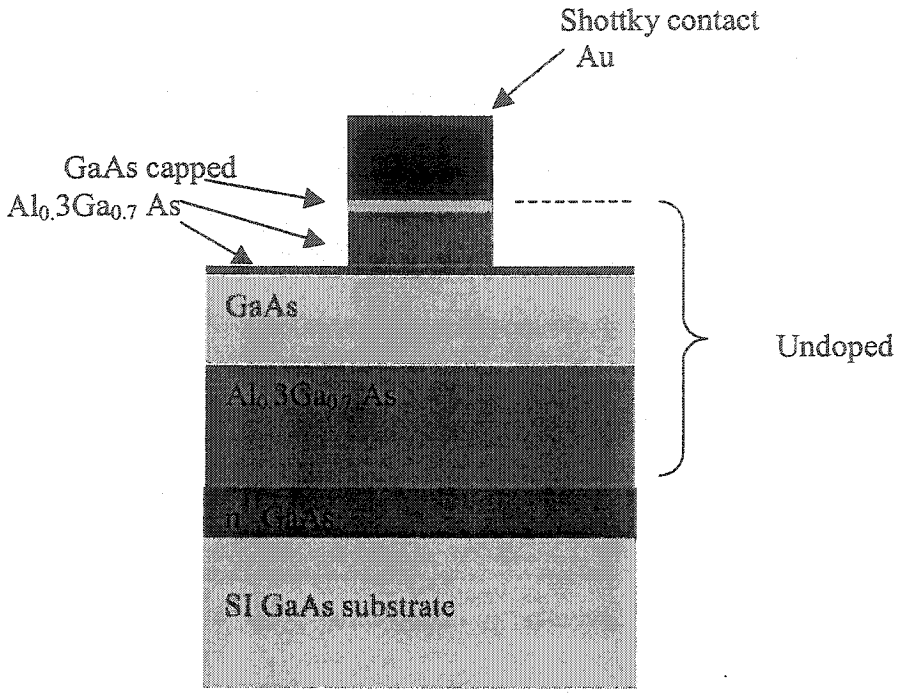

Figure 5.2 Schematic cross section of the GaAs/AlGaAs electro-optic waveguide.

Table 5. 1 Parameters of the ridge optical waveguide

Material Layers	Layer thickness (um)	Doping type	Doping level	Refractive index
GaAs	0.05	-	-	3.3704
$Al_{0.3}Ga_{0.7}As$	0.35	-	-	3.2317
$Al_{0.3}Ga_{0.7}As$	0.1	-	-	3.2317
GaAs	0.6	-	-	3.3704
$Al_{0.3}Ga_{0.7}As$	2.3	-	-	3.2317
GaAs	0.5	n^+	2×10^{18} cm^{-3}	3.3704
GaAs	200	Semi Insulating	-	3.3704

The simulation results for the TE mode of the optical waveguide shown above are presented in Table 5.2. Based on the design and numerical modeling, this waveguide supports single mode guiding with low optical propagation loss. The symbols used here are defined in chapter 4.

Table 5. 2 Parameters of the TE mode supported by the optical waveguide

n_{eff}	n_g	*PL* (dB/cm)	*Confinement factor (Γ)*	*mode size* (μm)	*Coupling loss* (dB/facet)
3.2993	3.5284	0.1	0.82	a_x=3.67; a_y=1.03	8.0

Figure 5.3 is used to sense the mode size of the designed waveguide in the lateral direction and the vertical direction.

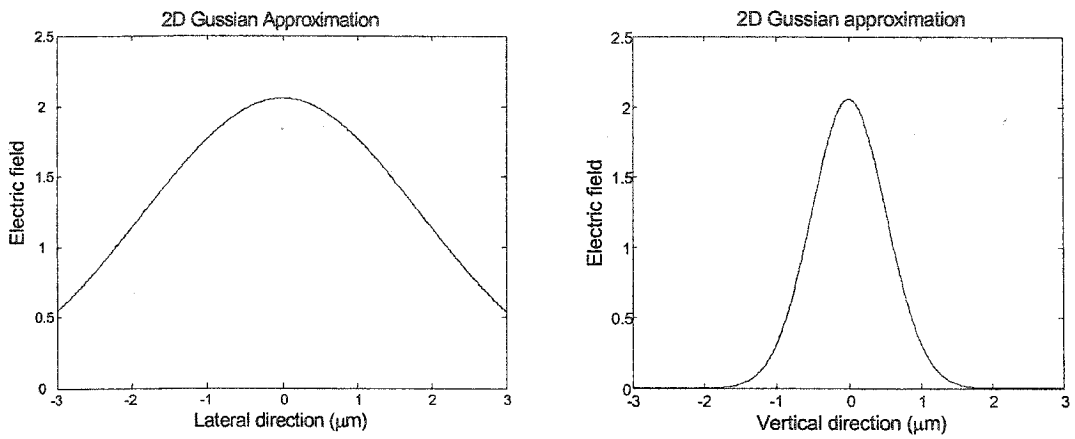

(a) (b)

Figure 5.3 Mode size of the designed waveguide (a) in the lateral direction (b) in the vertical direction.

5.2.2 Mach-Zehnder Interferometer

As discussed earlier, one of the most commonly used waveguide configuration in electro-optic intensity modulation is a Mach-Zehnder optical interferometer(MZI). It usually consists of three sections, a power splitter, an active section where the interaction between the optical and electrical signals occurs, and a power combiner. The power splitter and combiner are designed here to be Y-branch. The Y-branch for the power splitter and power

combiner can also be replaced by multimode interference sections (MMI). The Y-branch needs to be designed to minimize the optical loss at the junctions and reduce the overall device length. A large bending radius leads to smaller optical loss and longer device length. The bending radius is an important issue in devices whose length is short or the optical propagation loss per unit length is large, such as electroabsorption modulators. In the case of traveling wave electro-optic modulators, the device is usually long (≥ 1cm) for the electrode works as a transmission line, therefore, the Y-branch length is only a small part of the total device length that does not impose an strict design criterion. Here, the bending radii were chosen to achieve an optical loss less than 0.1dB per bend for the given slow wave electrode, and the optical structure.

5.3 Design of GaAs Traveling Wave Electro-optic Modulators Based on Capacitively Loaded Coplanar Strips Using Doped Layers

5.3.1 Characterization of the Design Space of Capacitively Loaded Coplanar Strips Using Doped Layers

Similarly, before modulators based on capacitively loaded Coplanar Strips (CPS) using doped layers are designed, the design space of this structure needs to be characterized first.

The following structure is used as the basic structure to characterize the unloaded CPS, with the cross section shown in Figure 5.4. The width of the signal electrode is W_s, the width of the ground electrode is W_g, and the gap between the signal electrode and the ground electrode is G. The width of the central region (the loading zone) is CW. The gap between the central region and the signal side region, and that between the central region and the ground side region are S_s and S_g, respectively. For the case $W_s=W_g=W$, the unloaded line is symmetrical line; for the case $W_s \neq W_g$, the unloaded line is asymmetrical line. The layer structure is based on the design of the waveguide, with layer thickness listed in Table 5.3. The electrode is 1um thick Au.

Table 5. 3 Layer structure of the unloaded symmetrical CPS line

Material Layers	Layer thickness (um)	Doping type	Doping level
Au	1	-	-
GaAs	0.05	-	-
$Al_{0.3}Ga_{0.7}As$	0.45	-	-
GaAs	0.6	-	-
$Al_{0.3}Ga_{0.7}As$	2.3	-	-
GaAs	0.5	n^+	2×10^{18} cm^{-3}
GaAs	200	Semi Insulating	-

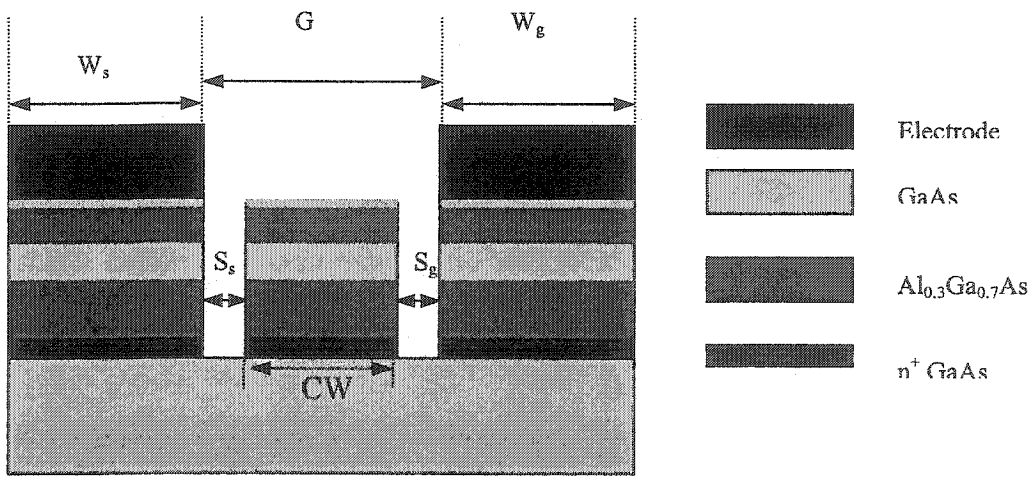

Figure 5.4 Basic structure for an unloaded CPS line (cross section).

Above all, the effects of central region on the microwave performance of the unloaded CPS lines are investigated. As shown in Figure 5.5 (a), the characteristic impedance of the unloaded CPS, Zu decreases with increasing CW while the unloaded microwave index n_u increases with the increase of CW. This is reasonable for the air region shrinks as the width of central region CW increases. As shown in Figure 5.5 (b), the microwave losses increase as CW increases.

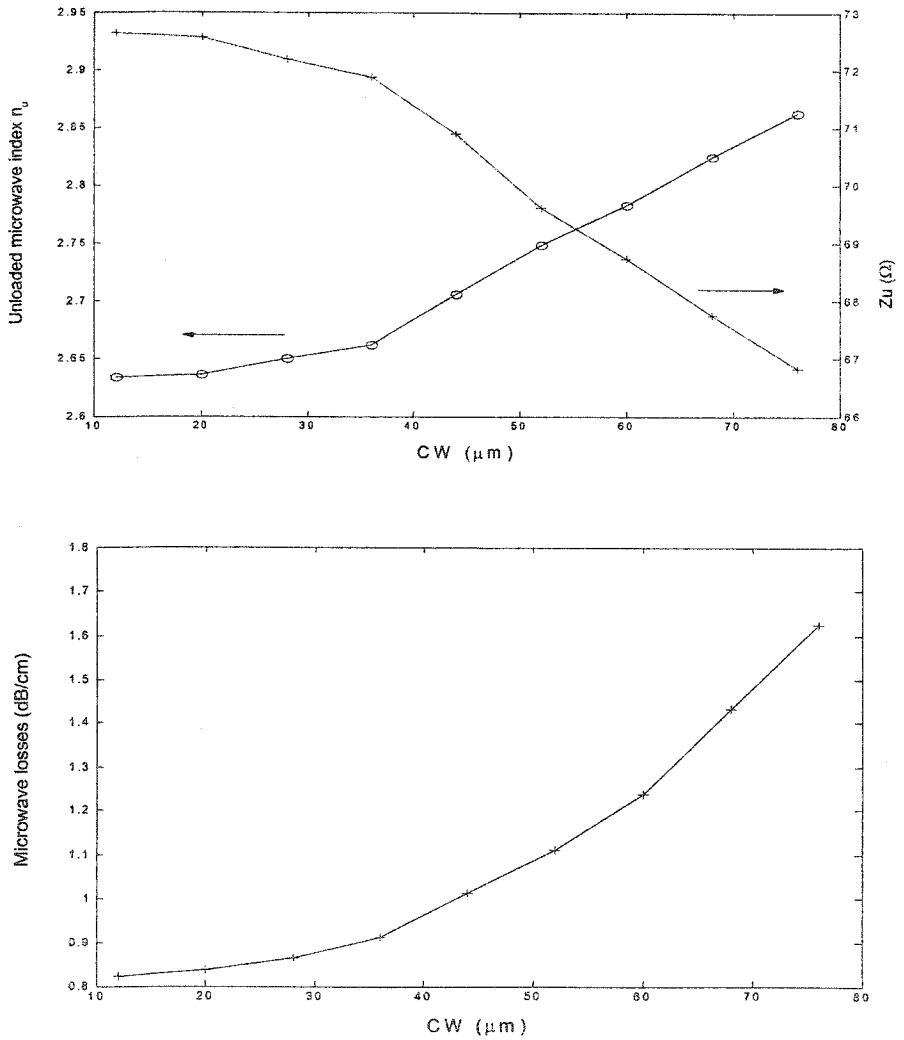

Figure 5.5 The effect of CW on the microwave performance of the unloaded CPS lines (a) characteristic impedance and microwave index versus CW (b) microwave losses versus CW. Here, W_s=W_g=156μm, G=84μm, S_s=S_g, CW=G- S_s-S_g. The simulation frequency is 30GHz.

From the simulation above, it is easily concluded that a narrow central region is beneficial from microwave loss point view. However, the central region is the loading zone where two waveguides are located so that it should be wide enough to prevent the coupling between two waveguides. Taking these factors into consideration, the ideal CW must be at least around 30 μm. In the following simulation and design, CW is chosen to be 28 μm.

Next, the effect of W_s, W_g and G on the microwave performance of the unloaded CPS lines will be studied. The aim is to design the CPS lines with the same characteristic impedance, 66.3 Ω, and then test the effect of Ws, W_g, and G combinations on the microwave performance of the line. The symmetrical CPS lines are studied first. In this case, W_s=W_g=W. In addition, S_s=S_g, and CW=28 μm.

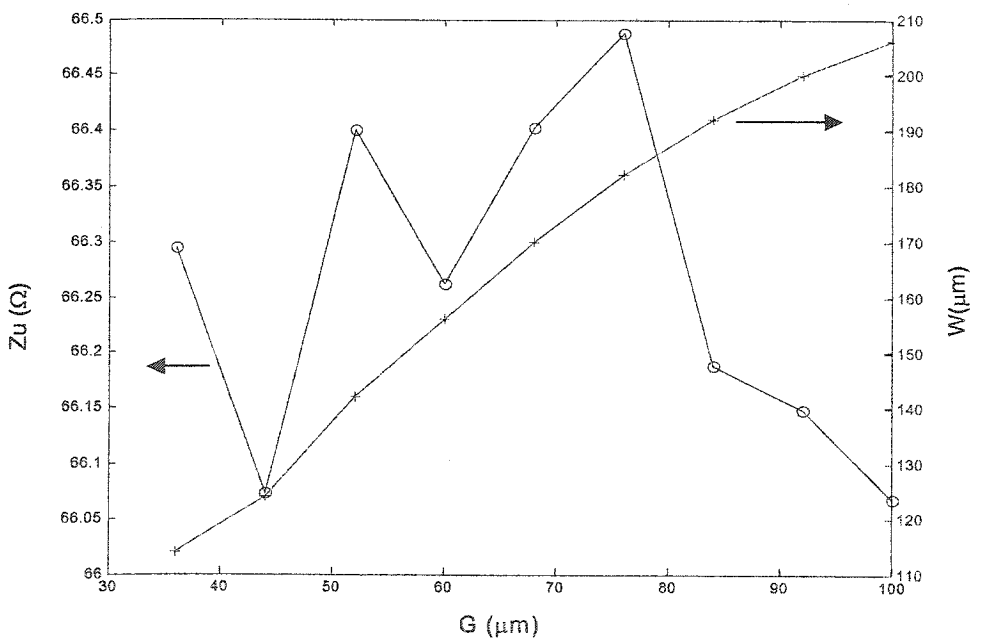

(a)

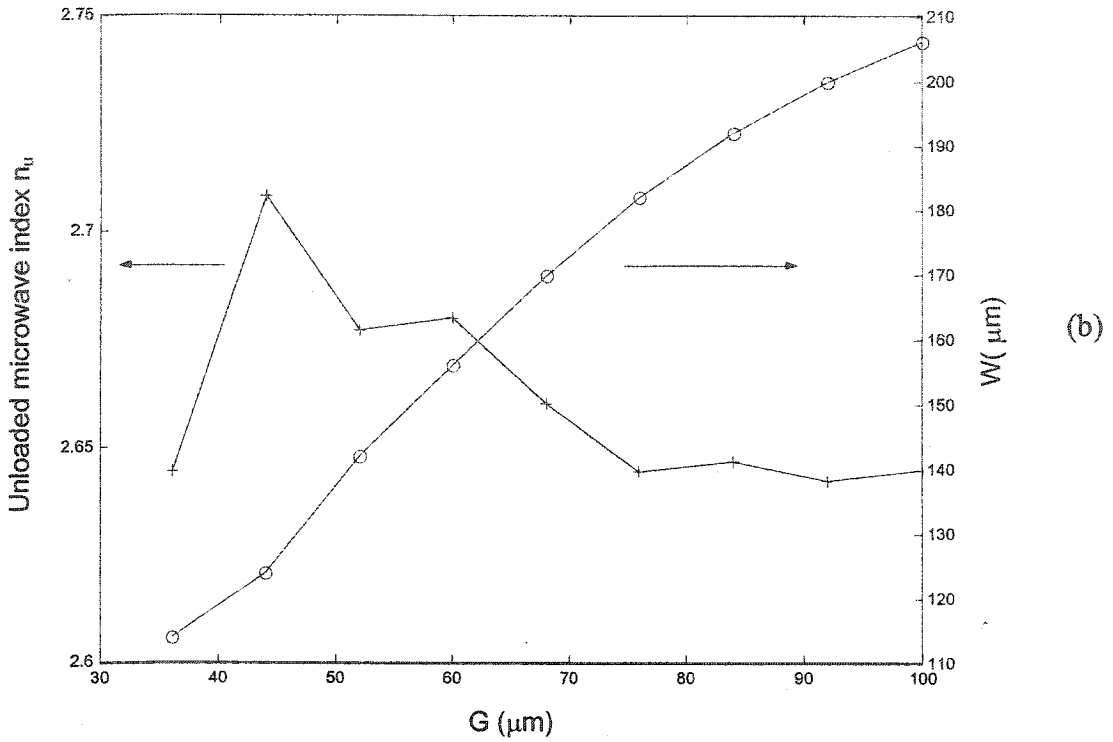

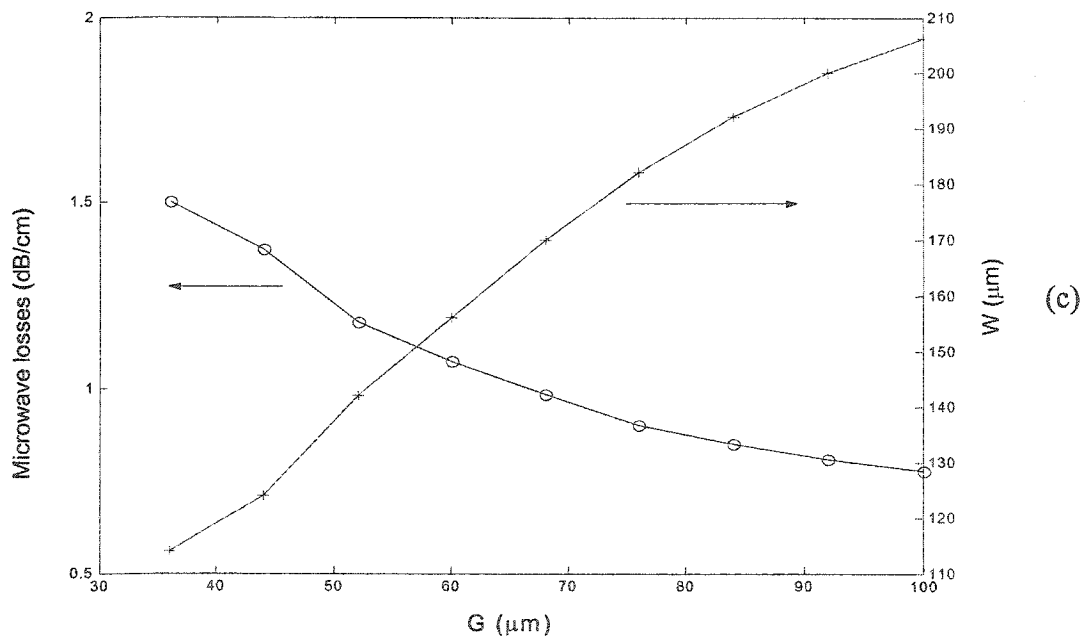

Figure 5.6 The effect of W and G combination on the microwave performance of unloaded CPS (a) characteristic impedance vs W and G combination (b) microwave index vs W and G combination (c) microwave losses vs W and G combination. The simulation frequency is 30 GHz.

Different combinations of W and G may yield the same value of characteristic impedance for symmetrical unloaded CPS lines. As shown in Figure 5.6 (a), all these combinations of W and G provide approximately the same value of characteristic impedance for the symmetrical unloaded CPS lines, about 66.3±0.3 Ω. The unloaded microwave index fluctuates in the range from 2.64 to 2.7 with the changes of W and G pairs. Microwave losses decrease as G and W simultaneously increase according to Figure 5.6 (c). Large G and W are advantageous to reduce the microwave losses.

For asymmetrical CPS lines, W_g is chosen to be larger than W_s. S_g-S_s=4 μm, and CW=28 μm. The combinations of W_s, W_g and G that produce approximately the same value of characteristic impedance for the asymmetrical uniform CPS lines are illustrated in Figure 5.7.

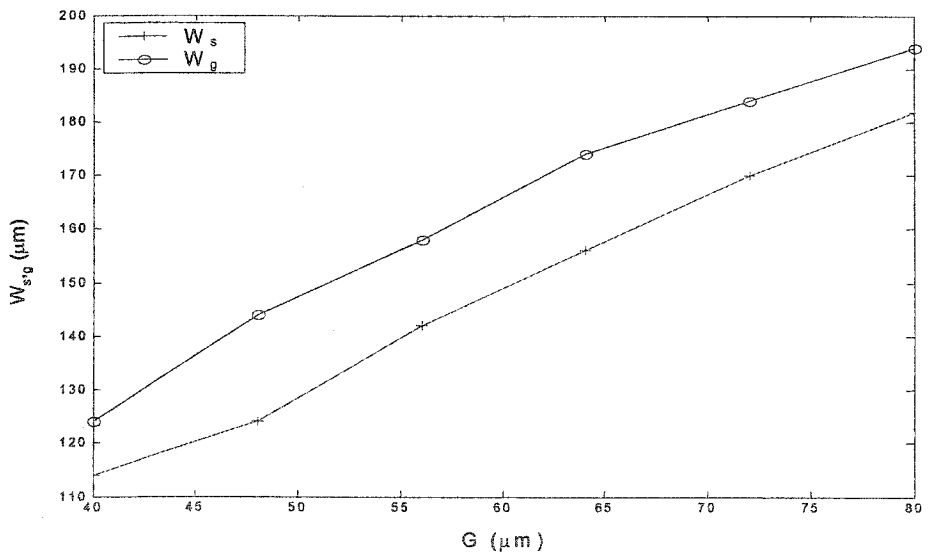

Figure 5.7 W_s and W_g versus G, and all these combinations yield approximately the same value of the characteristic impedance of asymmetrical unloaded CPS lines, 66.3 Ω. The simulation frequency is 30 GHz.

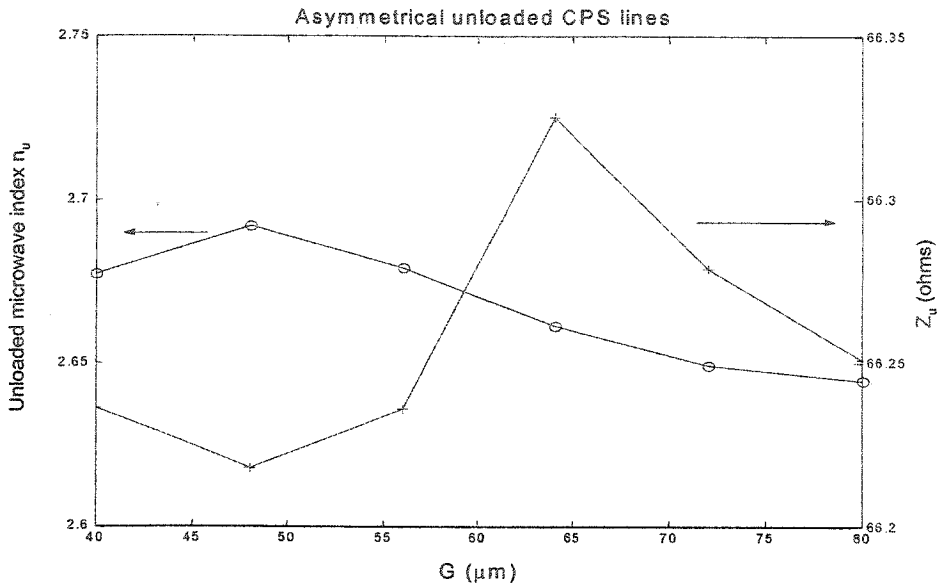

(a)

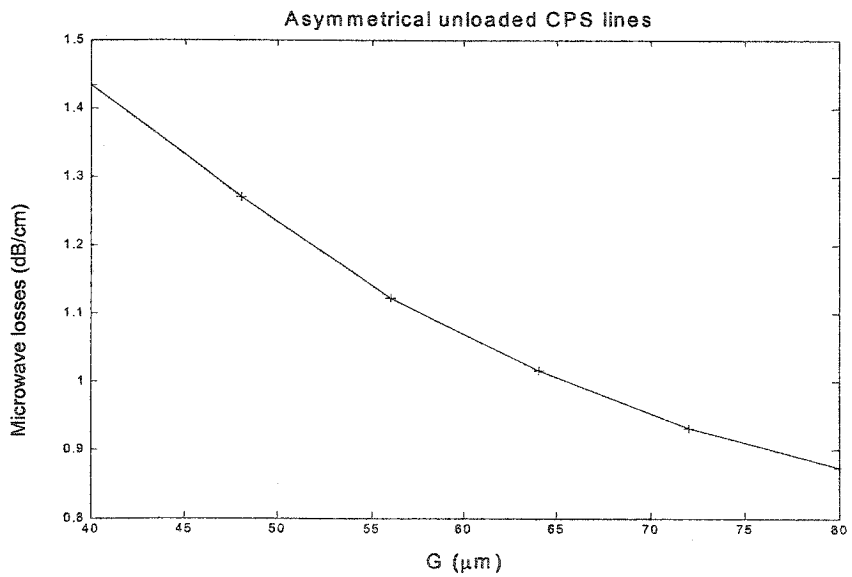

(b)

Figure 5.8 The effect of W_s, W_g and G combination on the microwave performance of asymmetrical unloaded CPS lines (a) characteristic impedance and microwave index vs the combination (b) microwave losses vs the combination.

As shown in Figure 5.8 (a), the characteristic impedance for all these lines is around 66.3±0.2 Ω, and the microwave index varies between 2.69 and 2.64. Microwave loss decreases with the simultaneous increase of W_s, W_g and G as Figure 5.8 (b) demonstrates.

According to the simulations above, one can conclude that a narrow central region, wide electrodes and a large gap between two electrodes are preferred due to low microwave losses for the design of unloaded CPS lines with the same characteristic impedance. Of course, the selected width of the central region needs to be wide enough to avoid the proximity of the two waveguides.

It is noted that the layer structure of the unloaded CPS lines are not completely the same as the waveguide structure. The small ridge parts of the waveguides are replaced by the large rectangular parts in the unloaded CPS lines. This approximation is valid for the thickness of the small ridge part is so thin compared to the thickness of other layers and substrate. It is to generalize and simplify the problem without the necessity of taking the width of the waveguides and the distance between the waveguides into consideration (compare Figure 5.4 and Figure 5.9 (a)).

Before loaded CPS lines are finally designed, some properties of these structures need to be investigated first, such as the effects of a loading element on the microwave performance of loaded CPS lines. The basic structure used to study these effects is shown in Figure 5.9. W_s and W_g are the signal electrode width and the ground electrode width, respectively; G is the gap between the signal electrode and the ground electrode. Loading period is P, and it is chosen to be 50 μm in the whole design to avoid dispersion of the line according to Equation (5.10). T_L and L_e are the length and width of the loading pad, respectively. The loading arm width for both sides (signal side and ground side) is aw while the length for the loading arm of the signal side, and for that of the ground side are

L_s and L_g respectively. The gap between the two loading pads is S and this is also the distance between the two waveguides, and $S=G-L_s-L_g-2*L_e$. The waveguide width is the same as the width of the loading pad. The layer thickness is exactly the same as that of the waveguide designed in the last section, as shown in Table 5.1.

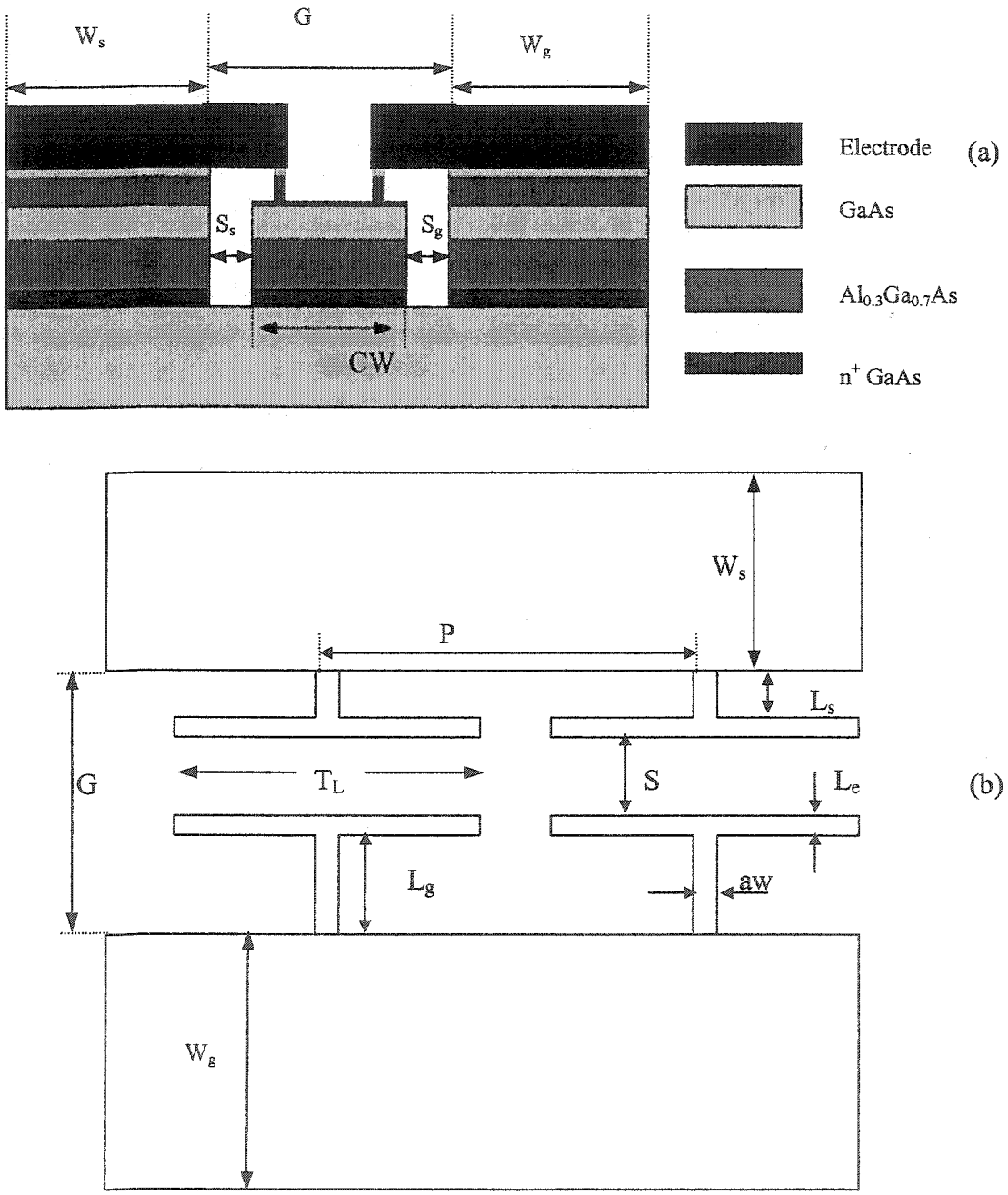

Figure 5.9 Basic structure for loaded CPS lines (a) cross section view (b) top view.

The loading pad is the crucial part in designing the loaded CPS electrodes for modulators, for the electric field underneath the loading pad, below which the optical waveguides lie, contributes to the electro-optic modulation. The effects of loading pads on the microwave performance of the loaded CPS lines are examined. As shown in Figure 5.10 (a), the loading capacitance increases with increasing T_L and L_e. The diamond at T_L =0 corresponds to the case where the loading pads disappear and the unloaded CPS lines are only loaded with loading arms. Thus the loading capacitance for T_L=0 comes from loading arms only, and is quite small, and it should be small because it does not contribute to the electro-optic modulation. As mentioned before, the unloaded capacitance C_u should be 1.34 pF/cm while the loading capacitance C_l should be around 1.015 pF/cm to achieve 50 Ω characteristic impedance and velocity matching. According to Figure 5.10 (a), for L_e=2 μm, the loading capacitance is not enough to achieve 50 Ω characteristic impedance and velocity matching for the whole range of T_L. The cases T_L =45 μm, L_e=4 μm and T_L=35 μm, L_e=6μm may provide 50 Ω characteristic impedance and velocity matching. This is confirmed later by the characteristic impedance and microwave index curves. The impact of loading pads on the inductance of the loaded CPS lines is shown in Figure 5.10 (b). Although the inductance of the loaded CPS lines slightly decreases with increasing T_L and L_e, it is very close to that of the unloaded CPS line. Generally, one can conclude that both loading pads and loading arms make a slight impact on the inductance of the loaded CPS lines so that the inductance of the loaded CPS lines are almost the same as that of the unloaded CPS lines. In fact, the above simulation results verify the basic properties of the periodic structure with capacitive loading, that is, capacitive loading effectively increases the capacitance of the line while it does not essentially change the inductance of the line.

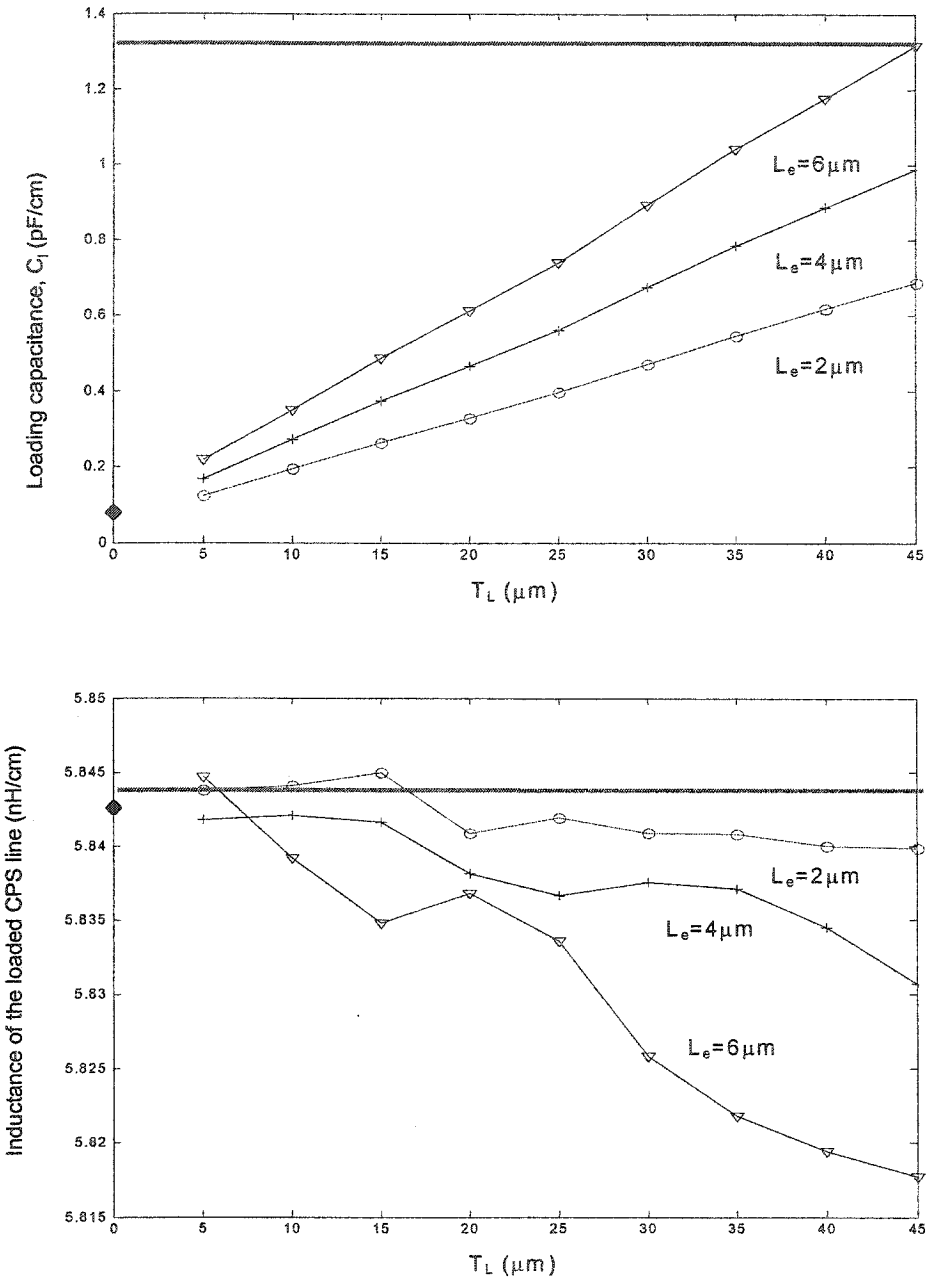

Figure 5.10 The effect of loading pads on the capacitance and inductance of the loaded CPS lines (a) loading capacitance vs T_L for different L_e. The straight line represents the capacitance of the unloaded CPS line (b) inductance of the loaded CPS line vs T_L for different L_e. The straight line represents the inductance of the unloaded CPS line. W_s=W_g=114 μm, G=36 μm, L_s=L_g=8 μm, aw=5 μm, CW=28 μm,P=50 μm, and S=G-L_s-L_g-2*L_e. The simulation frequency is 30 GHz.

The Microwave losses increase with increasing T_L and L_e, as illustrated in Figure 5.11.

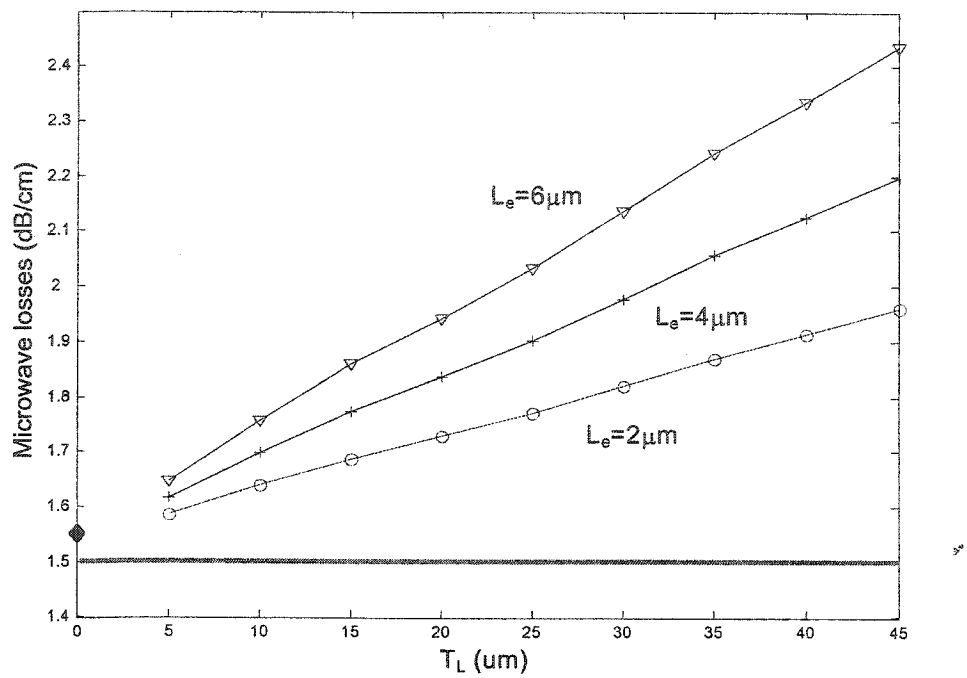

Figure 5.11 Microwave losses of the loaded CPS lines versus T_L for different L_e. The straight line represents the microwave losses of the unloaded CPS line. W_s=W_g=114 μm, G=36 μm, L_s=L_g=8 μm, aw=5 μm, CW=28 μm, P=50 μm and S=G-L_s-L_g-2*L_e. The simulation frequency is 30 GHz.

Because the capacitance increases with increasing T_L and L_e and the inductance is almost constant, the characteristic impedance of the loaded CPS lines, Z_0 decreases with increasing T_L and L_e as shown in Figure 5.12 (a), according to Equation (5.3). For the same reason, the microwave index of the loaded CPS line, n_m increases with increasing T_L and L_e according to Equation (5.4), as demonstrated in Figure 5.12 (b). Indeed, T_L =45 μm in the case of L_e=4 μm and T_L=35μm in the case of L_e=6μm provide 50 Ω characteristic impedance and velocity matching.

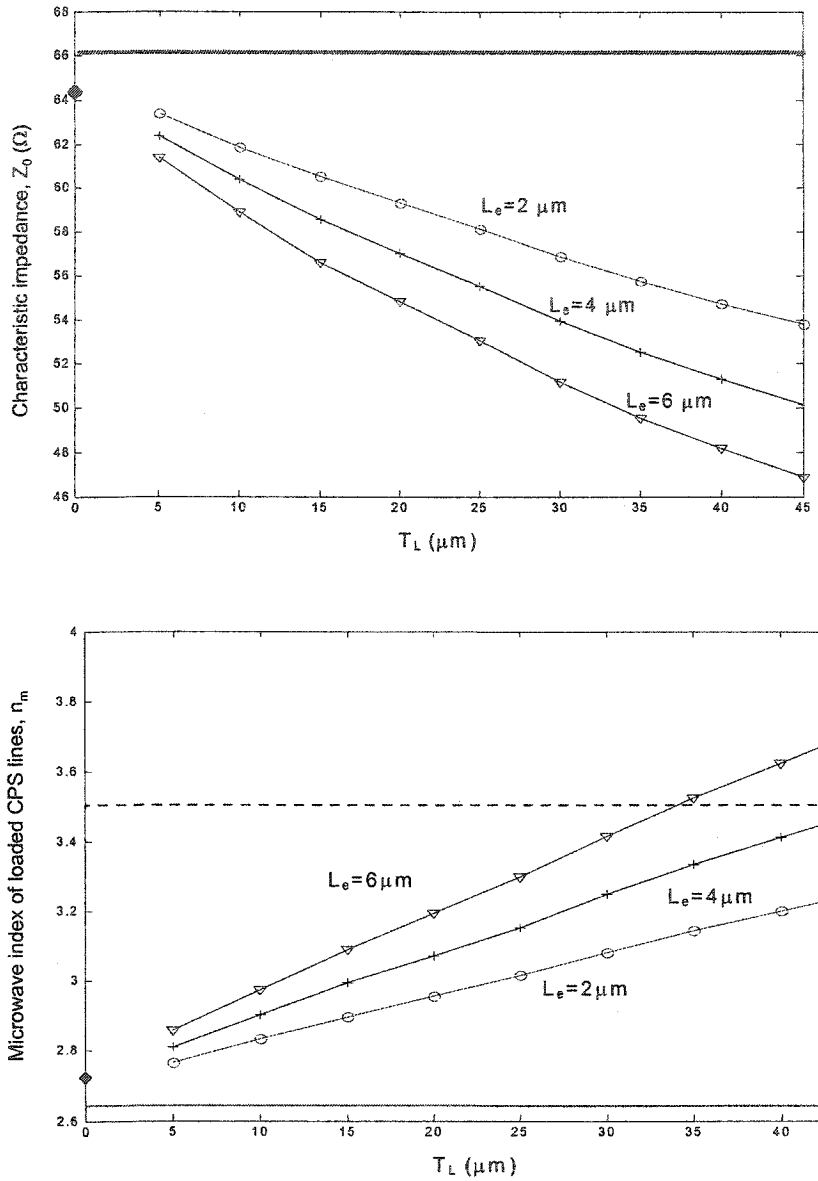

Figure 5.12 The effect of loading pads on the characteristic impedance and microwave index of the loaded CPS lines (a) characteristic impedance Z_0 vs T_L for different L_e. The straight line represents Z_u, the characteristic impedance of the unloaded CPS line (b) microwave index of loaded CPS lines, n_m vs T_L for different L_e. The straight solid line represents the microwave index of the unloaded CPS line, n_u, and the straight dashed line represents the optical index of the waveguide, n_g .W_s=W_g=114 μm, G=36 μm, L_s=L_g=8 μm, aw=5μm, CW=28 μm, P=50 μm and S=G-L_s-L_g-2*L_e. The simulation frequency is 30 GHz.

The impact of loading arms on the microwave performance of the loaded CPS lines is also studied. As shown in Figure 5.13 (a), loading capacitance increases with the increase of aw and L_g. In other words, larger aw and L_g may lead to a larger loading capacitance from loading arms. According to Figure 5.13 (b), the inductance decreases with increasing aw while increasing L_g only cause a slight decrease in inductance. In other words, the inductance is more sensitive to the change of aw. When aw is small enough, the inductance of the loaded CPS line is approximately the same as that of the unloaded CPS line. According to Figure 5.13 (c), the microwave losses also increase with increasing aw and L_g.

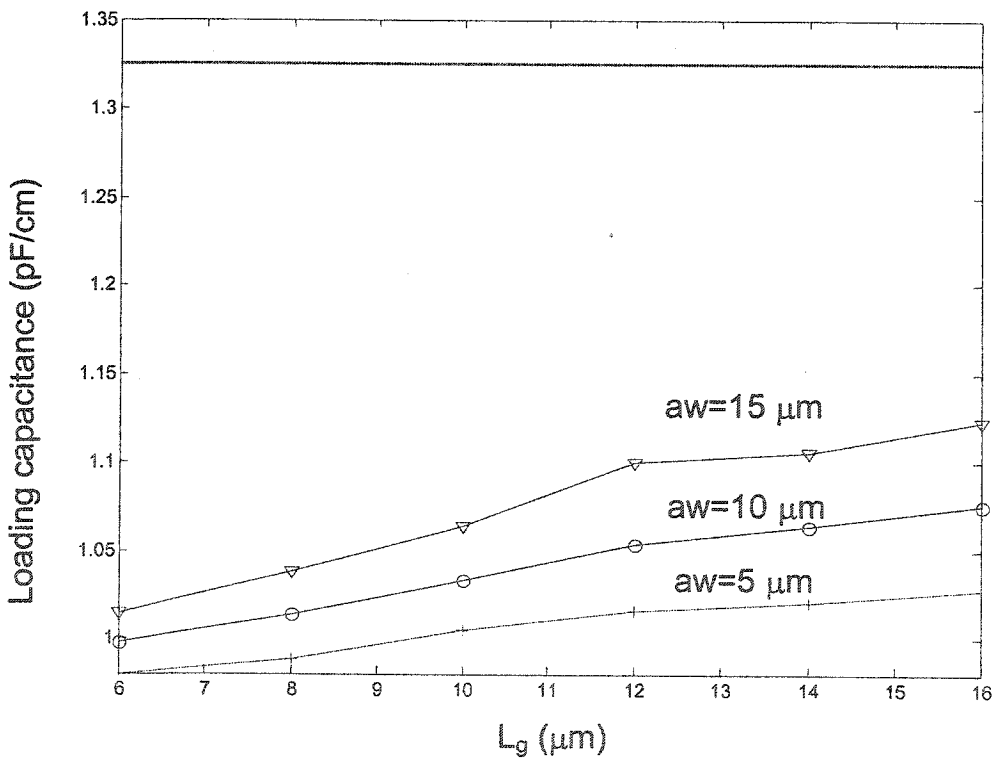

(a)

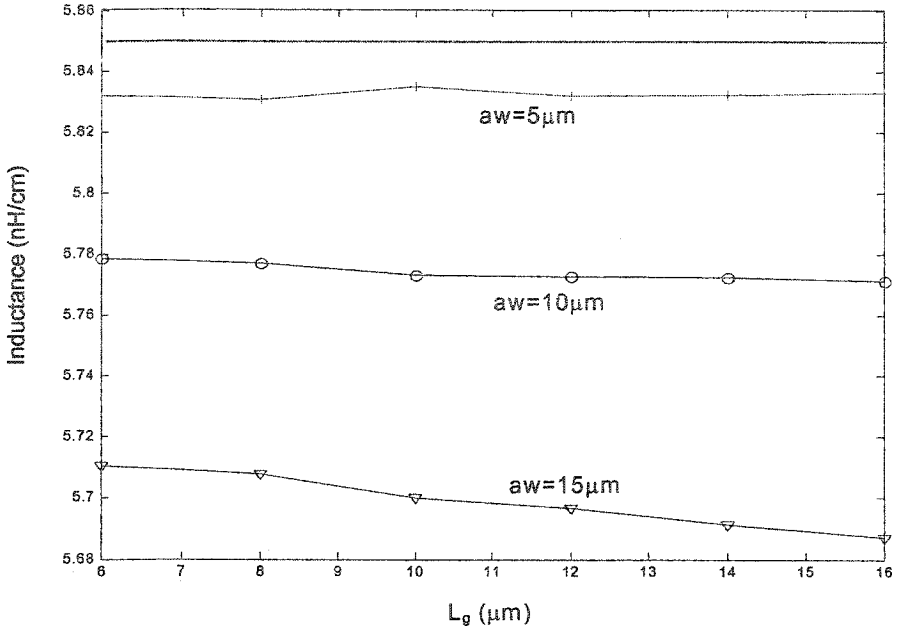

(b)

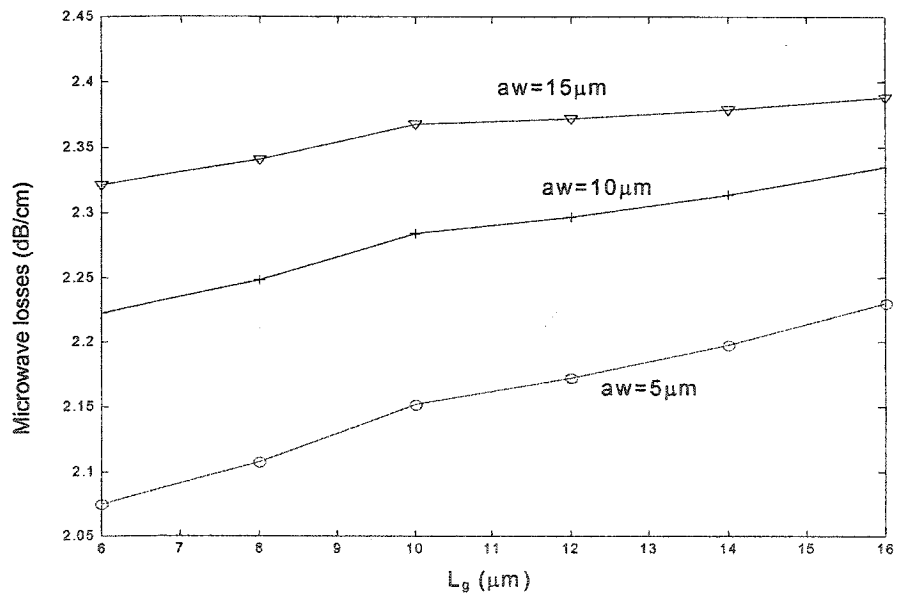

(c)

Figure 5.13 The effect of loading arm on loaded CPS lines (a) loading capacitance vs L_g for different aw. The straight line represents the capacitance of the unloaded CPS line. (b) Inductance of the loaded CPS lines vs L_g for different aw. The green straight line represents the inductance of the unloaded CPS line. (c) Microwave losses vs L_g for different aw. W_s=W_g=114 μm, G=36 μm, L_s=8 μm, CW=28 μm, S_s=S_g=(G-CW)*0.5=4 μm, T_L= 45 μm and L_e=4 μm, P=50 μm and S=G-L_s-L_g-2*L_e. The simulation frequency is 30 GHz.

In summary, the advantages that capacitively loaded CPS lines offer, impedance matching and velocity matching have been verified. As for the design of loaded CPS lines, the dimensions of the loading arms should be small to ensure that the loading capacitance from the loading arms is low for it does not contribute to the electro-optic modulation. Besides, the loading arms should be narrow enough to ensure that the inductance of a loaded CPS line is approximately the same as that of unloaded line. Long loading pads with moderate width are preferred to achieve impedance match and velocity match, for the length of the loading pads, T_L is the interaction length of electro-optic modulation. Too narrow loading pads may fail to achieve 50 Ω characteristic impedance while too wide loading pads may lead to short T_L so that modulation efficiency is lowered.

In addition, another advantage of the loaded CPS lines, low microwave losses are also verified. As shown in Figure 5.14, the microwave losses of a loaded CPS line are close to those of the unloaded CPS line below 60 GHz. As the frequency increases, the microwave losses from the loading elements increase so that microwave losses of the loaded CPS line bias further from those of its counterpart, the unloaded CPS line. However, even when the frequency is as high as 120 GHz, the microwave losses from the main signal and ground electrode still account for 50% of the total microwave losses and the microwave loss is still very low, only 16.6 dB/cm at 120 GHz. The Current distribution also supports this conclusion. As shown in Figure 5.15 (a), at a relatively low frequency such as 30 GHz, the main current is flowing along the inner edge of the main signal and ground electrode and current flow into the loading arms and pads are quite small, while at a relatively high

frequency such as 90 GHz, current flow into the loading arms and pads increases, but the main currents still flow along the inner edge of the main signal and ground electrode.

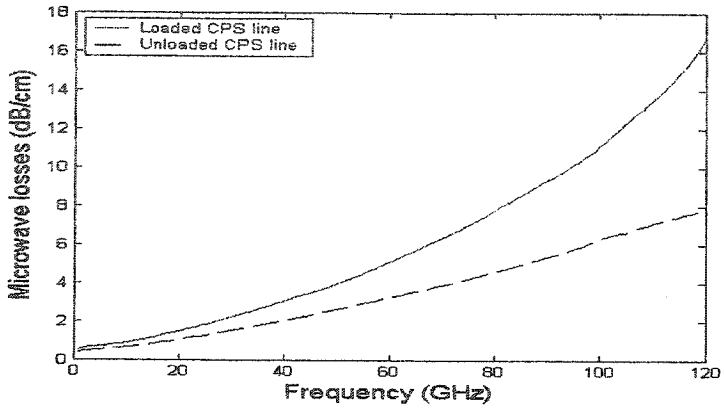

Figure 5.14 Microwave losses vs frequency. W_s=W_g=114 μm, G=36 μm, L_s=L_g= 8 μm, aw=5 μm, CW=28 μm, P=50 μm, T_L=45 μm, L_e=4 μm and S_s=S_g=4 μm and S=12 μm.

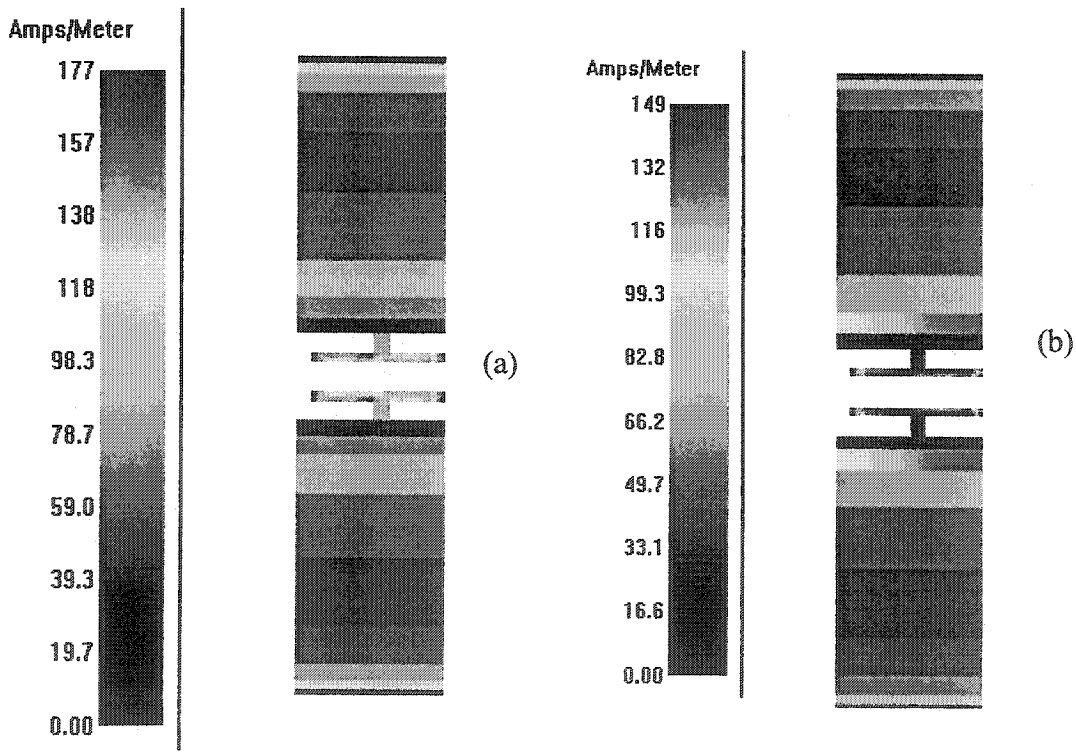

Figure 5.15 Current distribution along the loaded CPS line (one period) (a) at 30 GHz (b) at 90 GHz. W_s=W_g=114 μm, G=36 μm, L_s=L_g= 8 μm, aw=5 μm, CW=28 μm, P=50 μm, T_L= 45 μm, L_e=4 μm, S_s=S_g=4 μm and S=12 μm. V=1V.

As the microwave losses of the loaded CPS lines are dominated by those of the main currents, reducing current crowding by increasing the distance between the main currents G, and by making the central region (loading zone) reasonably small, (small CW) can significantly reduce the microwave losses of the loaded CPS lines, based on the analysis of unloaded lines. According to Figure 5.14 and Figure 5.15, the loading elements are just small capacitors so they do not carry axial current, thus the microwave losses from them are essentially small, though they increase as the frequency increases. In conclusion, periodic loading the uniform CPS with capacitive elements enables the design of low microwave loss structure.

Figure 5.16 shows the charge distribution on a typical loaded CPS line. This clearly illustrates the charge density variation on one period of a loaded CPS line. As Figure 5.16 shows, at both the low frequency (30 GHz) and high frequency (90 GHz), the maximum charge density always occurs in the loading pads. Due to the existence of the n^+ layer, a high electric field is generated between the loading pads and the n^+ layer. Because the optical waveguides are just between the loading pads and the n^+ layer, this high electric field contributes to the electro-optic modulation. In this scenario, the electric field overlaps the optical field very well as shown in Figure 5.1. In addition, the two loading pads and the n^+ layer forms two capacitors connected in series to each other as shown in Figure 5.1, thus the loading capacitance is halved. Consequently, the effective loading capacitance increases the interaction length of the electric field and optical field, thus reducing the half wave voltage.

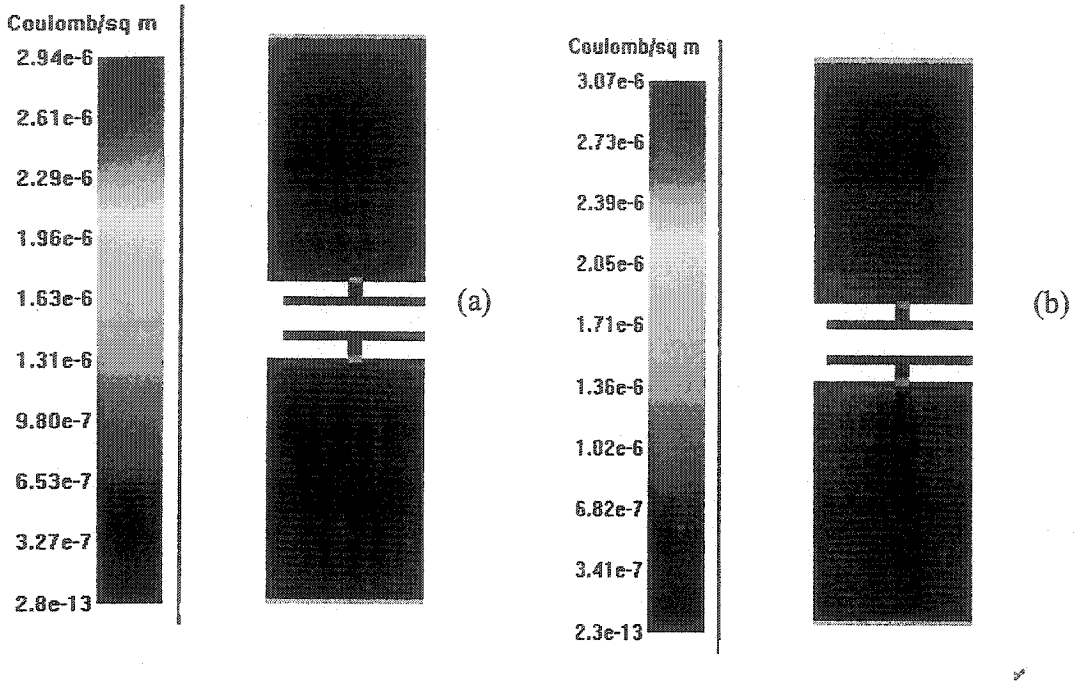

Figure 5.16 Charge distribution along the loaded CPS line (one period) (a) at 30 GHz (b) at 90 GHz. W_s=W_g=114μm, G=36μm, L_s=L_g= 8μm, aw=5μm, CW=28μm and P=50μm, T_L= 45 μm, L_e=4 μm, S_s=S_g=4 μm and S=12 μm. V=1V.

5.3.2 Design of GaAs Traveling Wave Electro-optic Modulators Based on Capacitively Loaded CPS Using Doped Layers

Based on the characterization of the design space of loaded CPS lines, a loaded CPS line with 50 ohms characteristic impedance and velocity matching can be designed with selected dimensions of the relevant parameters. First, an unloaded CPS line with 66.3 Ω is selected, of course, a CPS line with large G, W_s, W_g are preferred for low microwave losses. Next, loading pads and arms with appropriate dimensions are selected. Loading arms of narrow width are necessary to ensure the inductance of the line is not affected by loading elements. The loading pad should be long to increase the interaction length of the optical field and the electric field. The total loading capacitance should be around 1.015

pF/cm. Two loaded CPS lines are designed based on the characterization of the design space. Figure 5.9 shows the cross section and top view of loaded CPS electrodes designed. Table 5.4 provides the detailed dimension of the loaded CPS lines with 50 Ω characteristic impedance and velocity matching.

Table 5. 4 Dimension of loaded CPS lines designed

Line	W_s (μm)	W_g (μm)	G (μm)	CW (μm)	T_L (μm)	L_e (μm)	L_s (μm)	L_g (μm)	aw (μm)	P (μm)
sym	114	114	36	28	45	4	8	8	5	50
asym	114	124	40	28	45	4	8	12	5	50

Please note that $s=G-L_s-L_g-2*L_e$

Similarly, the designed GaAs traveling wave modulators utilizes a Mach-Zehnder Interferometer with y branch at the input and output for power splitting and combining, as shown in Figure 5.17. The cross section view of this modulator is shown in Figure 5.9 (a).

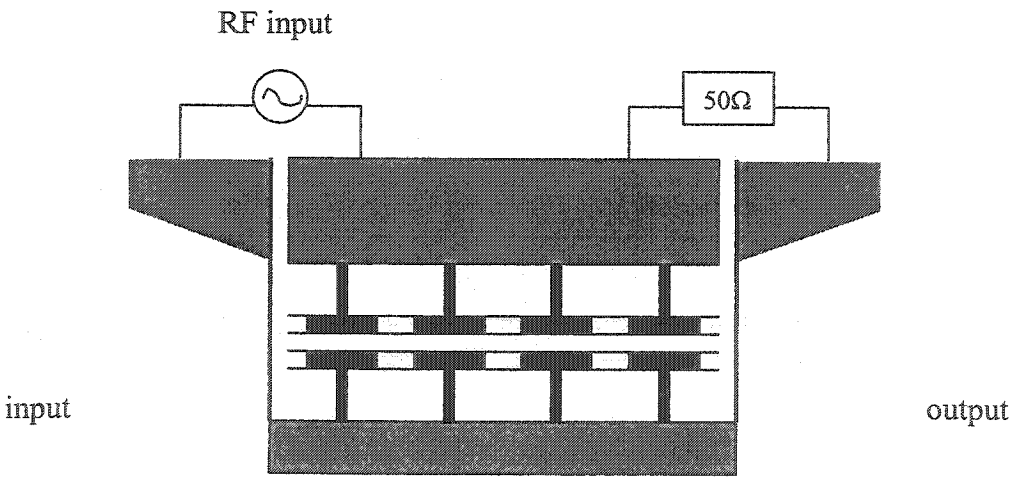

Figure 5.17 Top view of a GaAs traveling wave modulator with capacitively loaded CPS electrodes.

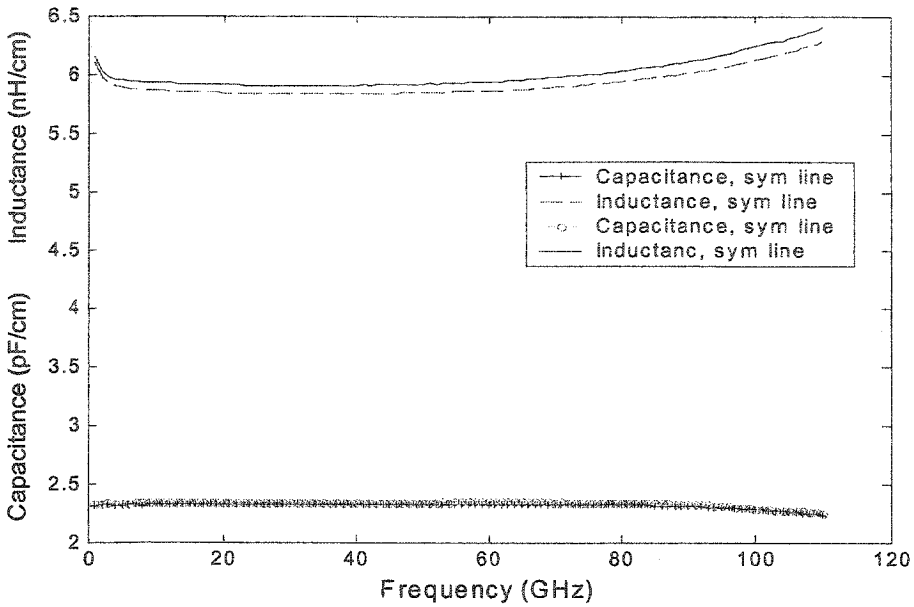

Figure 5.18 Capacitance and Inductance per unit length vs frequency.

As demonstrated in Figure 5.18, the capacitance per unit length is quite constant for the whole frequency band while the inductance per unit length is constant at low frequency and increases slightly as the frequency increases.

The characteristic impedance of both lines is close to 50 Ω for the whole frequency band as shown in Figure 5.19. The characteristic impedance increases slightly at high frequency due to the slight increase in the inductance per unit length as frequency goes up. Figure 5.20 shows the microwave index and phase velocity versus frequency. Both lines are not dispersive. In this case, the microwave phase velocity equals to the microwave group velocity. The short period P contributes to the non-dispersion of these lines. The velocity mismatch for both lines are within 3%.

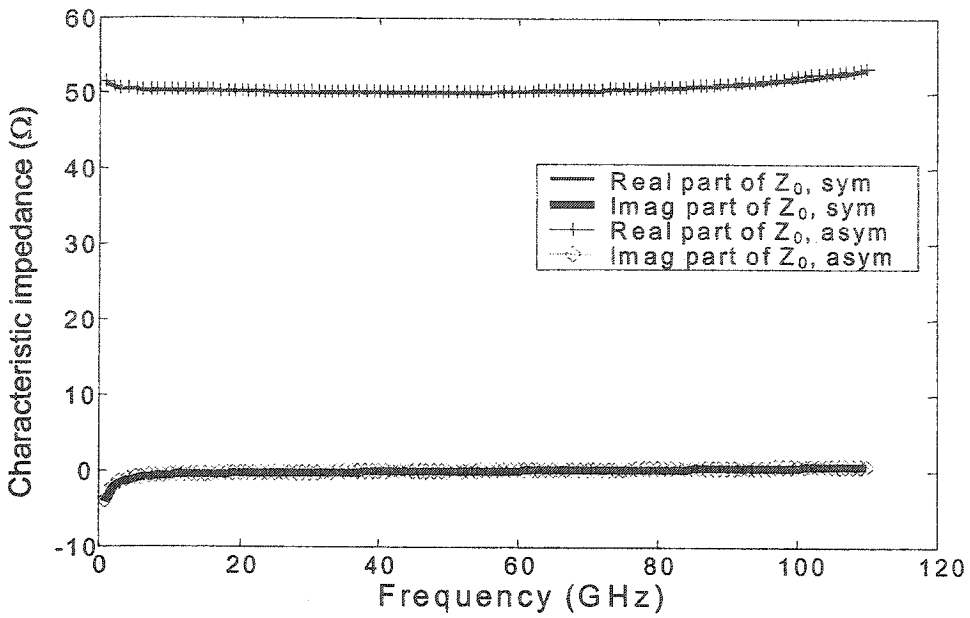

Figure 5.19 Characteristic impedance of loaded CPS lines vs frequency.

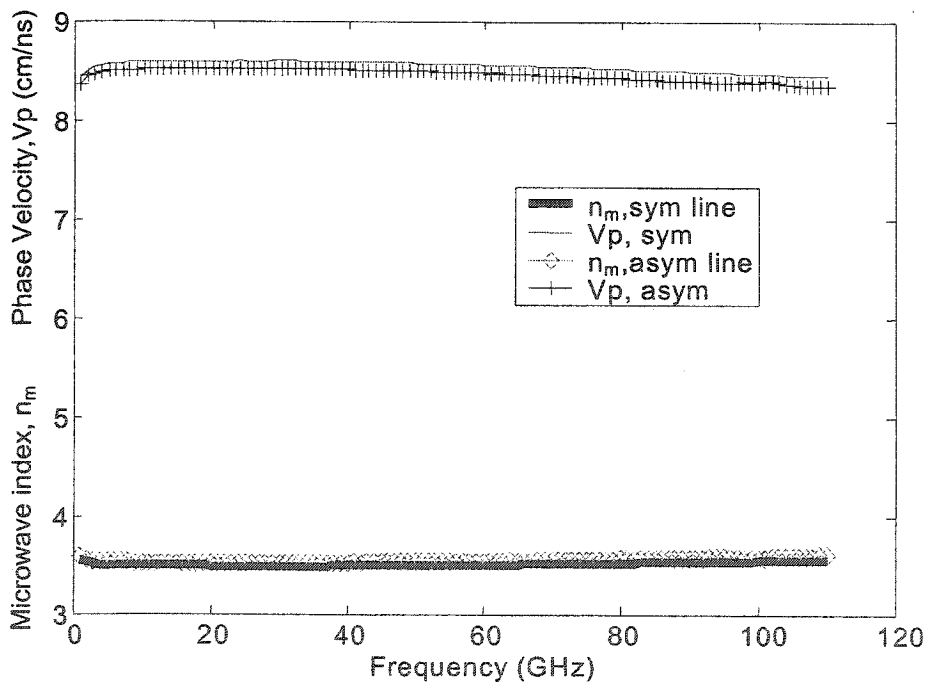

Figure 5.20 Microwave index and phase velocity vs frequency. The optical group index of the waveguide is 3.5284 thus the optical group velocity is about 8.5cm/ns.

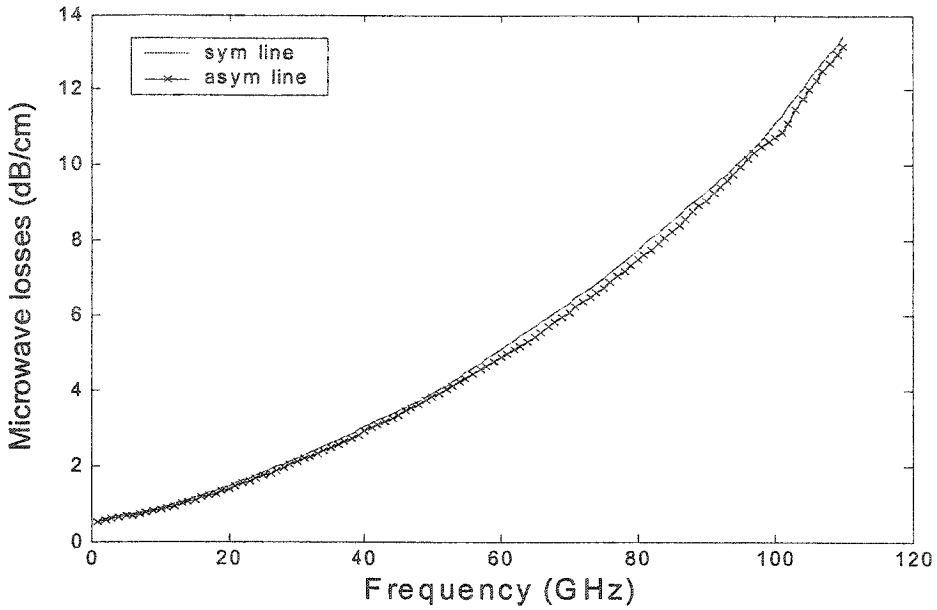

Figure 5.21 Microwave losses vs frequency for loaded CPS lines.

Though microwave losses increase with increasing frequency, they are quite low for both lines in comparison to the PMS lines designed in chapter 4, as shown in Figure 5.21. The microwave losses of the asymmetrical line are slightly lower than those of the symmetrical line.

The frequency response of the designed modulators can be predicted based on Equation (3.18). The length of the device is still normalized to 1cm. The frequency response of the GaAs traveling wave electro-optic modulators with capacitievely loaded CPS electrodes is shown in Figure 5.22. For the symmetrical line, an electrical 3 dB bandwidth of 70 GHz and an optical 3 dB bandwidth of 110 GHz can be predicted, while the asymmetrical line is expected to have an electrical 3 dB bandwidth of 71 GHz and an optical 3 dB bandwidth of 105 GHz. Although the asymmetrical line has slightly lower microwave losses, the

velocity mismatch for the asymmetrical line is larger than that for the symmetric line at high frequency, consequently the asymmetrical line has slightly narrower optical 3 dB bandwidth.

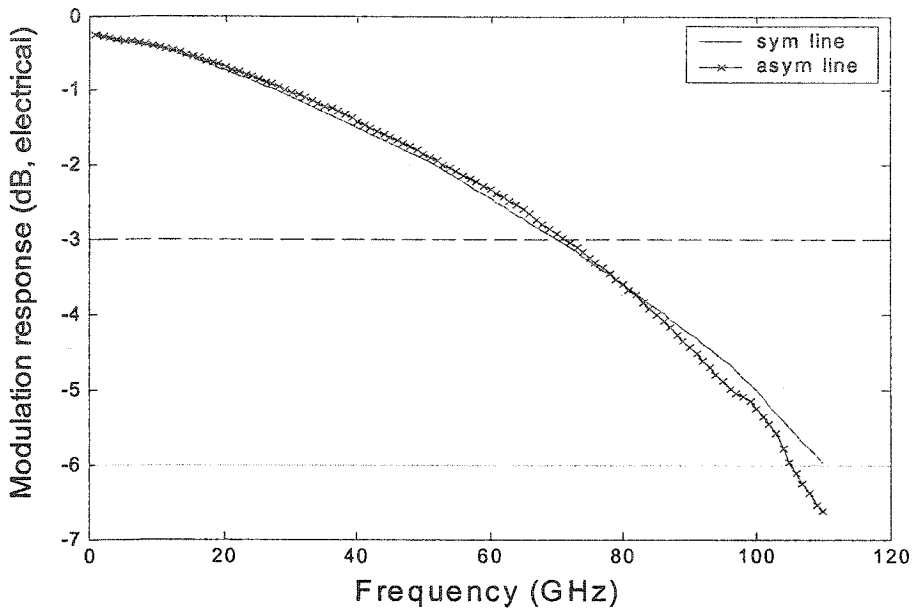

Figure 5.22 Modulation frequency response of GaAs traveling wave electro-optic modulators with capacitively loaded CPS electrodes. The length of the device is 1 cm. The straight dashed line and the straight solid line represent the electrical 3 dB and the optical 3 dB, respectively.

In addition, Figure 5.23 shows the modulation frequency response of GaAs traveling wave electro-optic modulators with different device length. As predicted based on Equation 3.18, the frequency bandwidth decreases as the device length increases due to the increase of microwave losses. As the device length increases, the advantage of the asymmetrical lines becomes apparent due to its lower microwave losses. For example, although both the symmetrical line and the asymmetrical line have almost the same electrical bandwidth around 70 GHz for 1 cm long device, the asymmetrical line has an electrical 3 dB

bandwidth of 44 GHz while the symmetrical line has an electrical 3 dB bandwidth of only 40 GHz for 2 cm long device.

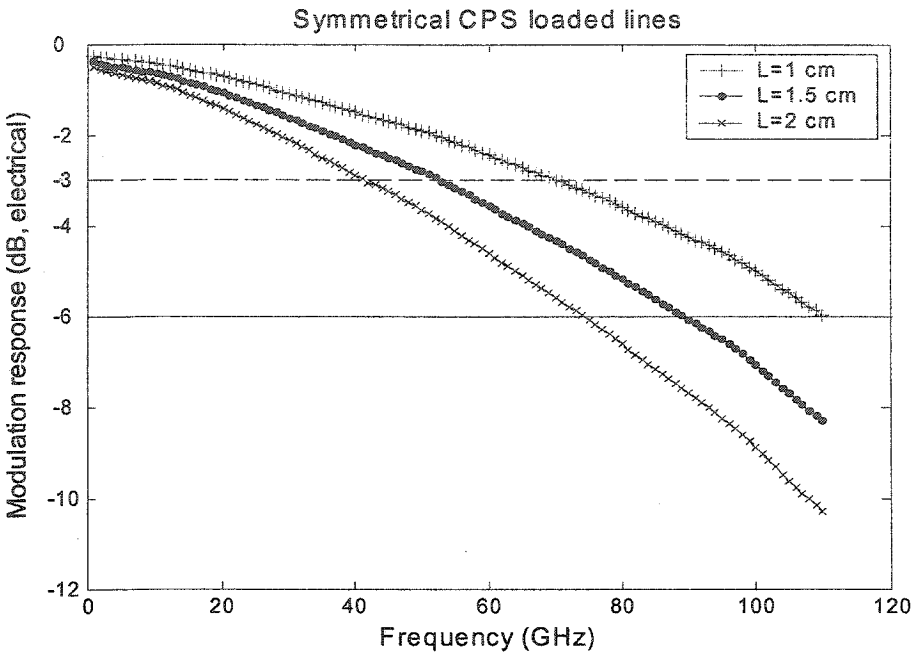

(a)

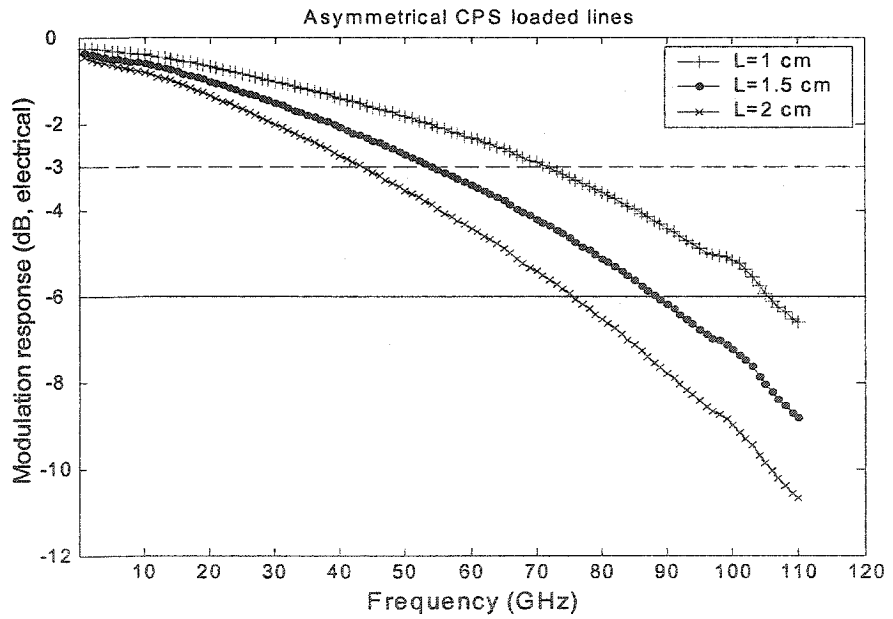

(b)

Figure 5.23 Modulation frequency response for different device length (a) symmetrical CPS loaded lines (b) asymmetrical CPS loaded lines. The straight dashes line represents the electrical 3 dB while the straight solid lines represents the optical 3 dB.

The electric field contributing to the electro-optic modulation is still along the [001] direction, so only the TE mode can be modulated. The expression for V_π with $E_{dc,rf}$ along the direction [001] becomes according to (2.18)

$$V_\pi = \frac{\lambda d}{n_0^3 r_{41} l_e \xi} \tag{5.9}$$

where λ is the optical wavelength, 1.55 μm , l_e is the effective length of the device, the interaction length of the optical field and microwave field. If the device length L is normalized to 1cm, then l_e=L*T_1/P=0.9 cm. The electro-optic coefficient for GaAs, r_{41} is about 1.42×10^{-12}(m/v), ξ is the overlap integral between the optical mode and the microwave field, and d is the depletion width; n_0 is 3.5284, the optical group index of the waveguide, and ξ is approximately unity for this kind of modulator, since the layers above the n^+ doped GaAs layer contain most of the optical mode as is indicated by the low propagation loss of the waveguide according to table 5.2, and d is the total thickness of the waveguide (except the thickness of n^+ layer and the substrate), d= 3.4 μm from table 5.1. The calculated $V\pi$ is about 9.4 V·cm.

Table 5. 5 Figure of merit of traveling wave modulators with CPS loaded electrodes.

Length (cm)	1 (sym)	1.5 (sym)	2 (sym)	1 (asym)	1.5 (asym)	2 (asym)
f_{3dBe} (GHz)	70	53	40	71	55	44
F_{3dBo} (GHz)	110	90	74	105	89	75
V_π (V)	9.4	6.3	4.7	9.4	6.3	4.7
Figure of merit (f_{3dBe}/V_π)	7.45	8.41	8.51	7.55	8.73	9.36

Table 5.5 listed the figure of merit for this kind of modulators with different lengths. Among these lines, the 2 cm long modulator with asymmetrical CPS loaded electrodes has the highest merit of figure, about 9.36 GHz/V.

5.4 Summary

In this chapter, both the design of the optical waveguide and the optimized design of the capacitively loaded CPS structure were presented. The properties of the optical waveguide, such as the effective refractive index, propagation loss, confinement factor and mode size, are mainly determined by the waveguide width, the epitaxial layer structure and the thickness of each layer. Sufficiently thick undoped layers prevent the leakage of the optical mode into the highly doped region, thus low propagation loss is guaranteed. With the capacitively loaded CPS slow wave structure, impedance and velocity matching are easily achieved while microwave losses can be kept low. Because the loading capacitors do not carry any of the axial currents in the transmission line, the microwave losses of the loaded line are close to those of the unloaded line. In short, capacitively loaded CPS is essentially a low loss microwave structure.

According to the analysis in this chapter, the following instructions provide help for the future design and optimization of GaAs traveling wave modulators with capacitively loaded CPS electrodes using doped layers:

(a) The designed unloaded CPS electrodes need to have a characteristic impedance around 66.3 Ω. Once this requirement is satisfied, large-scale CPS electrodes are preferred due to low microwave losses. In other words, large G , large W_s and W_g.

(b) The central region, the loading zone should be as small as possible. Of course, the width of this region needs to be large enough to avoid the coupling between the two optical waveguides.

(c) The dimensions of the loading arms should be small to ensure that the loading capacitance from the loading arms is small compared to that from the loading pads. In addition, the loading arm should be narrow such as 5μm or less in order that the inductance of the loaded CPS lines should be almost the same as that of the unloaded CPS line.

(d) The length of loading pad T_L should be as long as possible to increase the interaction length of the electric field and the optical field, thus loading pads with proper width L_e are preferred to those with small L_e or large L_e. Loading pads with small L_e, such as 2 μm may fail to achieve 50 Ω characteristic impedance and velocity matching, while loading pads with large L_e such as 6 μm may lead to a short loading length T_L (the interaction length of the optical field and the electric field), L_e is suggested to be between 3 μm and 5 μm.

(e) Short period P is suggested such as 100μm or 50μm to avoid dispersion.

In addition, a sufficient large depletion depth d enables good overlap between the applied electric field and the optical mode. The series push-pull drive effectively reduces the loading capacitance so that the interaction length of electric and optical fields can be

increased which in turn decreases the drive voltage. In summary, all these contributory factors, such as low microwave losses, easy realization of velocity and impedance matching, good overlap between the optical field and the electric field, microwave design and optical design decoupling to a large extent, can easily push the electrical 3 dB bandwidth of capacitively loaded CPS structure modulator up to 70 GHz and even higher. In our design, unloaded CPS electrodes with moderate dimensions are selected. If larger scale CPS electrodes are chosen, then microwave losses of the loaded CPS electrodes will decrease, and the electrical 3 dB bandwidth can extend up to 100 GHz.

CHAPTER 6

Conclusion

6.1 Traveling Wave Electro-Optic Modulators on GaAs Using Doped layers

In this thesis, key design issues of high speed traveling wave electro-optic modulators are discussed and traveling wave electro-optic modulators based on GaAs with a highly doped layer in the structure are designed, modeled and optimized. These modulators are in the form of a waveguide integrated with Planar Microstrip electrodes (PMS), and of a Mach-Zehnder interferometer integrated with capacitively loaded CPS electrodes. High-speed optical modulators are characterized by wide bandwidth and low half wave voltage. In order to obtain high speed traveling wave electro-optic modulators, several demands need to be satisfied. The velocity of the optical signal needs to be matched to that of the microwave signal, the characteristic impedance of the modulator needs to be 50 Ω to be closely matched to both the driver and load impedance and low microwave loss is imperative. In addition, the optical insertion loss needs to be minimized too.

Based on these objectives, two kinds of slow wave structures are designed, PMS and capacitively loaded CPS. These two slow wave structures have something in common. Firstly, a thin highly doped layer is utilized. Secondly, both can offer good overlap

between the optical mode and the applied electric field (the overlap integral is close to 1), if designed properly. Thirdly, both can only modulate the TE mode due to the direction of the applied electric field, thus modulators based on these two structures are polarization dependent modulators.

For PMS, the optical design and the microwave design are tightly coupled with each other. For example, one single parameter, the depletion width may affect several parameters, such as microwave loss, optical insertion loss, characteristic impedance, phase velocity and half wave voltage. Low microwave losses and low optical insertion losses demand large depletion width while low half wave voltage requires a small depletion width. Thus the bandwidth of the modulators based on PMS is greatly limited. The 3 dB electrical bandwidth of 15 GHz and the 3 dB optical bandwidth 40 GHz are predicted with a half wave voltage of 11.3 V·cm for 1 cm long device.

For capacitively loaded CPS, the optical and microwave designs are decoupled. Optical waveguides with low propagation loss can be designed without sacrificing the performance of the microwave structure. Impedance and velocity matching can easily be realized. As long as the impedance is kept approximately constant, the dimensions of the line can be designed large enough to reduce the microwave losses. Furthermore, capacitively loaded CPS is essentially a low microwave loss transmission line. All of these attributes help to increase the bandwidth of GaAs electro-optic modulators based on capacitively loaded CPS. Simulations predict that the electrical 3 dB bandwidth and

the optical 3 dB bandwidth, for the symmetrical line, can reach 70 GHz and 110GHz, respectively for 1cm long device while the half wave voltage is 9.4 V·cm.

6.2 Discussion of Some Issues

In this research, the design targets high-speed GaAs traveling wave electro-optic modulators with 50 Ω characteristic impedance. What the consequence will be if we design GaAs modulator with non-50 Ω characteristic impedance in the case of impedance match at both the generator end and the load? Will the figure of merit be improved for the modulator? This question can be answered for the two designs, respectively.

For the GaAs traveling wave modulators on PMS, characteristic impedance less than 50 Ω means larger capacitance and smaller inductance compared to the 50 Ω case according to equations (3.36) and (3.37). Based on the capacitance map as shown in Figure 4.16, larger capacitance requires smaller waveguide height, H, compared to the 50 Ω case if the same signal electrode width is chosen. This leads to the reduction of V_π, but also degrades the frequency response due to larger microwave losses. Following the same analysis, characteristic impedance larger than 50 Ω will lead to the increase of V_π and the wider bandwidth. It is difficult to conclude which case has the highest figure of merit due to the fact that frequency response is nonlinear function of microwave losses which itself is a function of H while V_π is proportional to H.

For the GaAs traveling wave modulators on loaded CPS electrode, characteristic

impedance less than 50 Ω requires larger loaded capacitance compared to the 50 Ω case according to equation (5.6). Larger loaded capacitance will require a smaller depletion width and longer loading pads so that V_π can be effectively reduced while the frequency response may not be affected as long as velocity and impedance match and low microwave loss are satisfied. Conversely, characteristic impedance larger than 50 Ω requires smaller loaded capacitance compared to the 50 Ω case, and this may lead to a higher V_π. In short, characteristic impedance less than 50 Ω may improve the figure of merit compared to the 50 Ω case.

Another concerned issue here is the electrical power dissipation of the designed GaAs traveling wave electro-optic modulators. In the case of perfect impedance match at the generator and the load, The electrical power dissipation P_e for the load of a traveling wave modulator can be written as $P_e = V_m^2/2Z$ with V_m the modulating voltage, and Z the characteristic impedance of the modulator electrode. The electrical power dissipation for the modulator electrode itself is small due to the low microwave loss of the electrodes. GaAs traveling wave modulators usually work with the bias and a small signal voltage applied, so power dissipation is not a problem at all in this situation. However, when deep extinction needed, drive voltage is close to V_π and power dissipation stands. High V_π means large power dissipation. For example, in the case of the designed GaAs modulator on loaded CPS electrode, V_π is about 9.4V for 1cm long device, thus $P_e \approx 0.9$ W. Thanks to the high thermal conductivity of GaAs (k_{th}=0.48 W/cm°C [58]), the power dissipation in the modulator can be channeled

away efficiently, without heating up the device considerably above the ambient temperature. Though dn/dT (the derivative of the refractive index change with respect to temperature change) is usually large for a semiconductor, as long as the temperature change in the two arms is the same for a MZI modulator, there will be no phase shift due to the temperature change so that the performance of MZI modulators will not be affected by the power dissipation. In short, power dissipation will not degrade the performance of the modulator to first order.

6.3 Thesis Contributions

In this thesis, traveling wave electro-optic modulators on GaAs with using doped layers have been designed and modeled [59]. The design space of two slow wave structures, PMS and capactively loaded CPS, are fully characterized, and thus provide guidance for future design and optimization of these two slow wave structures for the GaAs traveling wave electro-optic modulators. In addition, the frequency chirp parameter α is derived for both two kinds of modulators, polarization modulators and Mach-Zehnder modulators.

6.4 Future Work

Simulation and modeling have shown that GaAs/AlGaAs traveling wave modulators based on capacitively loaded CPS can offer wide modulation bandwidth. Naturally, the

next step is the fabrication of the devices proposed. Only when the fabricated devices are tested can the theoretical modeling be fully validated. Furthermore, improvement of the devices proposed need to be made. This includes the design of new electrode and optical structures. The simulation demonstrates that the half wave voltage is still high (higher than 5V) despite of the high bandwidth offered, thus new electrode and optical structures are needed to reduce the half wave voltage and microwave insertion loss. One promising approach is to use substrate-removed waveguides and process both sides of the epitaxial layer [60]. This should yield very high- speed devices with low drive voltages when combining with the undoped epitaxial layer approach.

REFERENCES

[1] T.H. Maiman, "Stimulated optical radiation in ruby masers," Nature, vol. 187, pp.493-494, 1960.

[2] F. P. Kapron, D. B. Keck, and R.D. Maurer, "Radiation losses in glass optical waveguides", *Applied Phys. Lett.*, vol 17, pp. 423-425, 1970 .

[3] J. Gowar, Optical Communication Systems, Prentice Hall, 1993.

[4] K. Yonenaga, M. Yoneyama, Y.Miyamoto, K. Hagimoto, and K. Noguchi, "160-Gbits/s WDM transmission experiment using four 40-Gbits/s optical duobinary channels," *Opt. Fiber Conf.*, vol 2, 1998, TUI2.

[5] A. Haasegawa, "Soliton-Based Optical Communications: An Overview" *IEEE J. of Selected Topics in Quantum Electron.*, Vol.6, No.6, pp.1161-1172 , Dec. 2000

[6] B.Wedding, " New method for optical transmission beyond dispersion limit," *Electron. Lett.*, vol.28, No. 14, pp. 1298-1300, July 1992.

[7] S. Weissner, E.C. Larkins, K. Czotscher, W. Benz, J. Daleiden, I. Esquivias, J. Rosenweig, "Damping Limited modulation bandwidths up to 40 Ghz in undoped short cavity In0.35Ga0.65As-GaAs mutiple quantum well laser, " *IEEE Photon. Technol. Lett.*, Vol. 8, pp.608-610, May 1996.

[8] C. Lawetz, J. C. Carledge, C. Rolland, and J.Yu, "Modulation characteristics of semiconductor Mach -Zehnder optical modulators," *J. Lightwave Tech.*, vol. 15, No. 4, pp. 697-702, 1997.

[9] T. H. Wood, "Mutiple quantum well (MQW) waveguide modulators," *J. Lightwave Tech.*, vol. 6, pp. 734-757, June 1988.

[10] Fang-Shang Chen, "Modulators for Optical Communications", *Proc.IEEE*, vol.58, No.10, pp 1440-1457, Oct. 1970.

[11] K. Wakita, K. Yoshino. I. Kotaka, S. Kondo, and Y. Noguchi, "Blue chirp electroabsorption modulators with very thick quantum wells," *IEEE Photon. Technol. Lett.* vol. 8, pp.1169-1171, sept. 1996.

[12] K.K.Loi, I. Sakamoto, X.B. Mei, C.W. Tu and W.S.C. Chang, "High efficiency 1.3-um InAsP-GaInP MQW electroabsorption waveguide modulators for microwave fiber optic links", *IEEE Photon. Technol. Lett.*, vol. 8, pp. 626-628, May 1996.

[13] T.Ido, S.Tannaka, M.Suzuki, M. Koizumi, H.Sano, and H.Inoue, "Ultra high-speed mutiple quantum well electroabsorption optical modulators with integrated waveguides," *J. Lighwave Tech.*, vol14, pp. 2026-2034, Sept. 1996.

[14] N.Mineo, K.Yamada, K.Nakamura, S. Saki, and T.Ushikobo, "60 GHz bandwidth electroabsorption modulator module," in *Opt. Fiber Conf.*, San Jose, CA, 1998.

[15] H. Soda, M. Furutsu, K. Sato, M. Matsuda, and H. Ishikawa, "5 Gb/s Modulation Characteristcis of Optical Intensity Modulator Monolithically Integrated with DFB Laser, " *Electron. Lett.*, Vol. 25, No. 5, Mar.1989, pp. 334-335.

[16] K.Yamada, K.Nakamura, and H. Horikawa, "Design of double pass electroabsorption modulators with low voltage, high-speed properties for 40Gb/s modulation," *J. Lightwave Tech.*, vol.15, pp.2287-2293, Dec.1997.

[17] K. Kawano, M. Kohtoku, M. Ueki, T.Ito, S.Kondoh, Y. Noguchi, and Y. Hasumi, "Polarization insensitive traveling wave electrode electroabsorption (TW-EA) modulator with bandwidth over 50Ghz and driving voltage less than 2V," *Electron. Lett.*, vol.33, no.18, pp. 1580-1581, Aug. 28, 1997.

[18] S. Irmscher, R. Lewen, and U. Eriksson, "InP-InGaAsP high-speed traveling wave electroabsorption modulators with integrated termination resistors," *IEEE Photon. Tech. Lett.*, vol. 14, No.7, July 2002.

[19] H. Takeuchi, Y. Hasumi, K. Kondo, and Y. Noguchi, "4×4 Directional coupler switch matrix with an InGaAlAs/ InAlAs multiple quantum well structure," *Electron. Lett.*, vol. 29, No.6, pp.441-443, 1992

[20] T. Aizawa, Y. Nagasawa, K.G. Ravikumar, and T. Watanabe, "Polarization-independent switching operation in directional coupler using tensile-strained multi-quantum well," *IEEE Photon. Tech. Lett.*, vol.7, No.1, pp.47-49, 1995.

[21] J. E. Zucker, K. L. Jones, T. H. Chiu, B. Tell, and K. Brown-Goebeler, "Strained quantum wells for polarization-independent electrooptic waveguide switches," *J. Lightwave Tech.*, vol. 10, No. 12, pp. 1926-1930, 1992.

[22] N. Agrawal, C. M. Weinert, H.J. Ehrke, G.G. Mekonnen, D. Franke, C. Bornholdt, and R. Langenhorst, "Fast Mach-Zehnder optical space switches using InGaAsP/InP multiquantumwell structures," *IEEE photon. Tech. Lett.*, vol.7, No.6, pp.644-645, 1995.

[23] Z. Wanru, D. Jining, Z. Zhenzhong , Y. Peisheng, S. Zhiwen, S.Furong, and G. Junhua, "Total internal reflection optical switch with injection region isolated by ion implantation," *Fiber and Integrated Optics*, vol,15, pp.27-36, 1995.

[24] R. C. Alferness, "Waveguide electrooptic modulators," *IEEE Trans. Microwave Theory Tech.*, vol. MTT-30, pp.1121-1137, Aug.1982.

[25] G. K.Gopalakrishnan, C. H. Bulmer, W.K. Burns, R. W. McElhanon, and A.S. Greenblatt, "40GHz, low half-wave voltage Ti: LiNbO3 intensity modulator," *Electron. Lett.*, vol. 28, pp.826-827, Apr. 1992.

[26] K. Noguchi, O. Miyomi, H. Miyazawa, "Millimeter-wave Ti: LiNbO3 optical modulators," *J. Lightwave Tech.*, Vol. 16, pp. 615-619, Apr. 1998.

[27] S.-J. Chang, C.-L. Tsai, Y.B. Lin,-F-Liu, and W.-S. Wang, "Improved electro-optic modulator with ridge structure in X-cut LiNbO3," *J. Lightwave Tech.*, vol.17, pp. 843-847, 1999.

[28] R. Madahushi, "Wide-band Ti: LiNbO3 optical modulator with low driving voltage," in *Proc. Tech. Dig. OFC'96*, 1996, paper ThB3.

[29] W. K. Burns, M. M. Howerton, R. P. Moeller, A. S. Greenblatt, and R. W. McElhanon, "Broad-band reflection traveling-wave LiNbO3 modulator," *IEEE Photon. Technol Lett.*, vol. 10, pp.805-806, June 1998.

[30] Jacob B. Khurgin and Jin U. Kang, "Ultrabroad-bandwidth electro-optic modulator based on a cascaded Bragg grating", *Optics Lett.*, vol. 25, No. 1, pp. 72, January 2000.

[31] S. Y. Wang and S. H. Lin, "High speed III-V electrooptic waveguide modulators at Lamda=1.3um," *J. Lightwave Tech.*, vol. 6 , pp. 758-771, June 1988.

[32] S. H. Lin., S. Y. Wang, and Y. M. Houng, "GaAs p-i-n electrooptic traveling-wave modulator at Lamda=1.3um," *Electron Lett.* , vol. 22, pp. 934-935, 1986.

[33] S. H. Lin., S. Y. Wang, and Y. M. Houng, "GaAs travelling-wave polarization electrooptic waveguide modulator with bandwidth in excess of 20Ghz at 1.3um," *Appl. Phys. Lett.*, vol. 51, pp. 83-85, 1987.

[34] I. Kim, M. R. T. Tan, and S. Y. Wang, "Analysis of a new microwave low-loss and velocity-matched III-V transmission line for travelling electrooptic modulators," *J. Lightwave Tech.*, vol. 8, pp. 728-737, May 1990.

[35] Y. Fukuoka, Y. Shih, and T. Itoh, "Analysis of slow-wave coplanar waveguide for monolithic integrated circuits," *IEEE Trans. Microwave Theory Tech.*, vol MTT-31, pp. 567-573, July 1983.

[36] D. Jager, "Slow-wave propagation along variable schottky-contact microstrip line," *IEEE Trans. Microwave Theory Tech.*, vol. MTT-24, pp.566-573, Sept 1976.

[37] Y. Fukuoka and T. Itoh, "Slow-wave coplanar waveguide on periodically doped semiconductor substrate," *IEEE Trans. Microwave Theory Tech.*, vol. MTT-31, pp. 1013-1017, Dec.1983.

[38] J. Nees, S. Williamson, and G. Mourou, "100Ghz travelling -wave electrooptic phase modulator," *Appl. Phys. lett.*, vol.54, pp.1962-1964, 1989.

[39] R. Spickermann, S. R. Sakamoto, M. G. Peters, and N. Dagli, "GaAs/ AlGaAs traveling wave electrooptic modulator with electrical bandwidth greater than 40Ghz," *Electron. Lett.* vol.32, no. 12, pp 1095-1096, June 6, 1996.

[40] H.R. Khazaei, "High-speed GaAs/ AlGaAs travelling wave electro-optic modulators," Ph.D Thesis, Ecole Polytechnique Montreal, Canada, 1999.

[41] R. G.Walker, "High-speed III-V Semiconductor Intensity modulators," *IEEE J. Quantum Electron.* , vol. 27, pp.654-667, Mar. 1991.

[42] R. G.Walker, "Electrooptic modulation at mm-wave frequencies in GaAs/AlGaAs guided wave devices," in *Proc. IEEE/ LEO'95 8th Annu. Meeting* , San Francisco, CA, Oct.30-Nov.2, 1995, pp. 118-119.

[43] A.Yariv, Optical Electronics, 4th ed. New York:Holt, Rinehart and Winston, 1991.

[44] I. P. Kaminow and W.D. Johnston, Jr., "Quantitative determination of sources of the electro-optic effect in $LiNbO_3$ and $LiTaO_3$", *Phys. Rev.*, vol. 160, pp.519-522, August 1967.

[45] F. Jona and G. Shirane, *Ferroelectric Crystals*. New York: Macmillan, 1962.

[46] S. Namba, "Electrooptic effect of zincblende", *J. Opt. SOC. Amer.*, vol.51, pp.76-79, 1961

[47] F. Koyama, "Frequency Chirping in External Modulators", *J. Lightwave Tech.*, vol. 6,No. 1, pp.87-93, January 1988.

[48] D.M. Pozar, *Microwave Engineering* . New York: John Wiley& Sons, Inc. , 1998, pp.162.

[49] K.C. Gupta, R. Garg, I. Bahl, and P. Bhartia, *Microstrip lines and slotlines*. Norwood, MA: Artech House, 1996.

[50] Sunderland, D., and Dapkus, P.D. "Optimizing N-p-n and P-n-P heterojunction bipolar transistors for speed," *IEEE Trans. Electr. Dev.* 34, pp. 367-377, 1987.

[51] H. Hasegawa, M.Furukawa and H.Yanai, "Properties of microstrip line on Si-SiO_2 systerm," *IEEE Trans. Microwave Theory Tech.*, vol. MTT-19, pp.869-881, Nov.1971.

[52] Sonnet User's Manual, Release 6.0, Sonnet Software, Inc. 1020 Seventh North St., Suite210, Liverpool, NY 13088 USA.

[53] R.E. Collin, *Foundations for Microwave Engineering*, McGraw-Hill, Inc. 1992.

[54] H. Matsumura and T. Suganuma, "Normalization of single-mode fibers having an arbitrary index profile," *Appl. Opt.*, vol.19, pp.3151-3158,1980.

[55] R.G.Hunsperger , *Integrated optics theory and technology*. Springer, 1997.

[56] J.V.Roey, J.V.D.Donk and P.E. Lagasse, "Beam propagation method: analysis and assessment," *J. Opt. Soc.* America, vol. 71, pp.803-810, 1981.

[57] *BeamProp*^{TM} *Version4.0,* Rsoft, Inc.200 Executive Blvd. Ossining, NY 10562 USA

[58] Sadao Adachi "GaAs, AlAs, and $Al_xGa_{1-x}As$: Material parameters for use in research and device applications," *J. Appl. Phys.*, vol 58, No.3, R1-R29, August 1985

[59] Y.Cui, P. Berini, "GaAs/AlGaAs Traveling Wave Electro-optic Modulator for Operation at a wavelength of 1.55um," *ISMOT 2001*, pp.670-673.

[60] S.R.Sakamoto, C.Ozturk, Y.T.Byun, J.Ko and N.Dagli, "low loss substrate-removed (SURE) optical waveguides in GaAs/AlGaAs epitaxial layers embedded in organic polymers," *IEEE Photon. Technol. Lett.*, vol.10, pp.985-987, July 1998.